INSTITUTO SUPERIOR DE ENGENHARIA DO PORTO
MESTRADO EM ENGENHARIA MECÂNICA

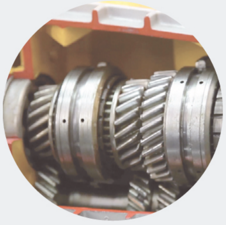

Housing components for autonomous underwater vehicles ? design and structural validation via finite element analysis

PEDRO NUNO DE ALMEIDA ARROJADO DA SILVA PEREIRA
novembro de 2021

POLITÉCNICO
DO PORTO

Instituto Superior de
Engenharia do Porto

HOUSING COMPONENTS FOR AUTONOMOUS UNDERWATER VEHICLES – DESIGN AND STRUCTURAL VALIDATION VIA FINITE ELEMENT ANALYSIS

Pedro Nuno de Almeida Arrojado da Silva Pereira

1160618

2021

Instituto Superior de Engenharia do Porto

Departamento de Engenharia Mecânica

POLITÉCNICO
DO PORTO

Housing components for autonomous underwater vehicles – design and structural validation via finite element analysis

Pedro Nuno de Almeida Arrojado da Silva Pereira

1160618

Dissertation presented to ISEP – Instituto Superior de Engenharia do Porto – to fulfill the necessary requirements to obtain the Master's degree in Mechanical Engineering, carried out under the guidance of Doctor Raul Duarte Salgueiral Gomes Campilho and Doctor Andry Maykol Gomes Pinto.

2021

Instituto Superior de Engenharia do Porto

Department of Mechanical Engineering

JURY

President

Doctor Ramiro Carneiro Martins

Assistant Professor, ISEP

Supervisors

Doctor Raul Duarte Salgueiral Gomes Campilho

Assistant Professor, ISEP

Doctor Andry Maykol Gomes Pinto

Senior Researcher, INESC TEC

Examiner

Doctor Isidro de Jesús Sánchez-Arce

Senior Researcher, INEGI

ACKNOWLEDGEMENTS

My deepest appreciation to everyone involved in the development of this thesis.

To my professor and supervisor, Doctor Raul Campilho for the thoughtful guidance, feedback, and availability demonstrated throughout the process of writing and whose expertise was fundamental and invaluable to the successful completion of this thesis.

To my colleagues at INESC, for their companionship and help during these last months, particularly my scientific supervisor, Doctor Andry Pinto, for the opportunity and confidence placed in me, as well as the advice and guidance provided.

And finally, to my family and friends, whose support and belief encourages me to push forward, and whose presence and companionship is the greatest pleasure in life.

KEYWORDS

Autonomous underwater vehicles; Product development; Structural analysis; Wireless Charging; Imaging perception system; Ashby material selection method.

ABSTRACT

Every day, more and more effort is put into the production of green energy as a countermeasure to climatic changes and sustainability. One of the biggest bets of the energy industry is in offshore wind energy, using wind towers. This technology can benefit greatly from interventive AUVs to assist in the maintenance and control of underwater structures. The wireless charger system extends the time the AUV can remain underwater by allowing it to charge its batteries through a docking station. On the other hand, the imaging perception system enables a 3D reconstruction of the AUV target, thus contributing to the mission.

The present work details the development process of housing components for two different systems: a wireless charging system and an imaging perception system, to be implemented in an AUV, from the concept stage to the final physical verification stage. These products were designed following a design for excellence and modular design philosophy, implementing visual scorecards to measure the success of certain design aspects. For an adequate choice of materials, the Ashby material selection method is implemented. The prototypes structural performance was validated via linear static finite element analysis before being outsourced for production. These prototypes were further physically verified in a hyperbaric chamber.

Results show that the application of FEM, together with well-defined design goals, have a very positive impact in the optimization of the housings, which would have been more time consuming and costly otherwise. Additionally, the Ashby material selection method allowed to equate the material choice, achieving the best performance for the lower cost.

PALAVRAS-CHAVE

Veículos autónomos subaquáticos; Desenvolvimento de produto; Análise estrutural; Carregamento *Wireless*; Sistemas de perceção de visual; Método Ashby de seleção de material

RESUMO

A cada dia que passa, há um crescimento do esforço dedicado à produção de energias verdes como medida de oposição às alterações climáticas. Uma das maiores apostas da indústria energética é em energia eólica em alto mar. Esta tecnologia beneficia fortemente de veículos autónomos subaquáticos de intervenção que assistem na manutenção e controlo de estruturas subaquáticas. O sistema de carregamento *wireless* permite carregar as baterias do veículo subaquático através duma estação de atracamento, prolongando o tempo que permanece debaixo de água. Por outro lado, o sistema de perceção visual permite a reconstrução tridimensional do objeto alvo do veículo, contribuindo para a missão de intervenção.

O presente trabalho detalha o processo de desenvolvimento de dois componentes de *housing* para dois sistemas diferentes: um sistema de carregamento *wireless* e um sistema de perceção visual, que serão implementados num veículo autónomo subaquático, desde a fase de conceito até verificação física dos *housings*. Estes produtos são projetados seguindo filosofias de *design* de excelência e *design* modular, implementando tabelas de desempenho visuais que medem o sucesso de certos aspetos do *design*. Para uma escolha adequada de materiais, implementou-se o método de seleção de Ashby. A performance estrutural dos *housings* foi validada por análises lineares estáticas de elementos finitos antes de serem terceirizados para produção. Adicionalmente estes protótipos foram fisicamente verificados numa câmara hiperbárica.

Os resultados deste projeto demonstram que a aplicação do método de elementos finitos, junto com metas bem definidas de *design,* teve uma contribuição bastante positiva para a otimização dos *housings*, que de outra forma teria consumido muito tempo e recursos. O método de seleção de materiais de Ashby permitiu equacionar a escolha de material, que permite a melhor performance por um custo mais reduzido.

LIST OF SYMBOLS AND ABREVIATIONS

List of abbreviations

3D	Three-dimensional
PLA	Polylactic Acid
ABS	Acrylonitrile Butadiene Styrene
PET	Polyester
POM	Polyoxymethylene
PEEK	Polyetheretherketone
PA	Polyamide
AUV	Autonomous Underwater Vehicle
BREP	Boundary Representation
CAD	Computer Aided Design
CAM	Computer Aided Manufacturing
CNC	Computerized Numerical Control
DFX	Design for excellence
DVL	Doppler Velocity Log
FEA	Finite Element Analysis
FEM	Finite Element Method
GPS	Global Positioning Systems
I-AUV	Intervention Autonomous Underwater Vehicle
INS	Inertial navigation systems

LBL	Long Baseline
MARIN	Maritime Research Institute Netherlands
MEMS	Micro-Electro-Mechanical-Systems
POV	Point Of View
PS	Pressure Sensor
ROV	Remotely Operated underwater Vehicle
SBL	Short Base Line
STL	Standard Tessellation Language
TOPSIS	Technique for Order Preference by Similarity to Ideal Solution
USBL	Ultra-Short Baseline
IPSH	Imaging Perception System Housing
WCH	Wireless Charger Housing
LED	Light Emitting Diode
PCB	Printed Circuit Board
MOSFET	Metal Oxide Semiconductor Field Effect Transistor
FOS	Factor of Safety

Unit List

m	Meter
m^2	Square meter
cm^3	Cubic centimeter
mm	Millimeter
MPa	Megapascal

GPa	Gigapascal
kg	Kilogram
g	Gram
K	Kelvin
V	Volt
A	Ampere
W	Watt
kJ	Kilojoule

Symbol List

P	Pressure
ρ	Density
g	Gravity acceleration
h	Water depth
M_i	Material index
W_i	Material weighted index
%	Percentage
w_i	Normalized property weight
w_i^*	Property weight
$\sum$	Summation
σ_f	Failure stress

FIGURES INDEX

TABLES INDEX

ÍNDEX

INTRODUCTION

1 INTRODUCTION

1.1 Framework

The development of green technologies has been a concern since the Tokyo protocol in 1992. Public awareness of these issues is also a contributing factor for the need of change and adaptation in the current industry scenario. The development of green energies is an answer to the environment issues the world is facing today, and one of the biggest bets of this sector is wind energy. There are two main types of wind power stations: inland, and offshore. Although inland wind turbines allow for easier maintenance as well as construction, wind turbines cause a lot of noise, and being close to civilization can originate some concerns regarding visual disamenities and landscape. Offshore wind turbines are far from civilization, with the additional bonus of being able to collect more power due to stronger winds at sea [1], leading to a significant growth in Europe, as shown in Figure 1.

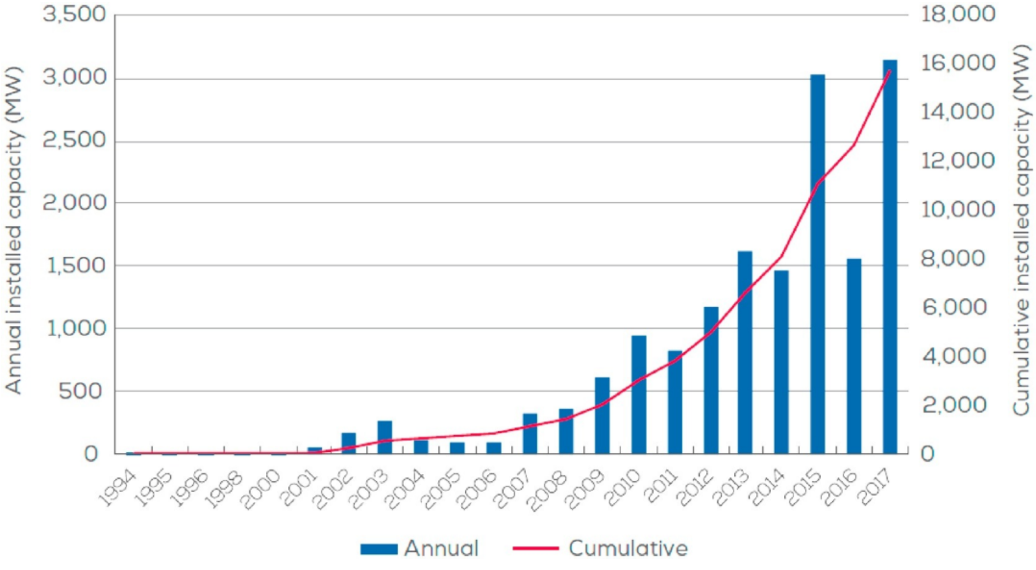

Figure 1. Offshore Wind power in Europe 1994 – 2017 [2].

The goals for installed wind capacity defined by the European Council in 2014 assures an expected growth until 2030 [2]. The main problem with offshore power farms is that the underwater environment is not easily accessible. Thus, maintaining and constructing these structures has proven to be very difficult and expensive [1]. These issues are paving the way to a new market: interventive autonomous underwater vehicles (I-AUV). These vehicle's main concept is to use imaging systems and robotic arms to inspect and perform maintenance of various structures [3]. However, this technology is still in a very early stage. This report presents the development of an underwater imaging system housing (IPSH) and wireless charger housing (WCH). The imaging perception system aims to reproduce a three-dimensional (3D) reconstruction of underwater objects to enable an autonomous interaction between the manipulator and the object. The wireless charger system aims to improve the longevity of the vehicle mission, without having to return to the surface, by enabling battery charging at a docking station.

1.2 Objectives

The objective of this dissertation is to document the development process of an underwater imaging perception system housing and a wireless charger housing, which can be easily integrated in any I-AUV and be able to resist hydrostatic pressures at 300 meters depth.

For this dissertation, the following tasks were performed:

1. Definition of the main objectives and initial considerations;
2. Definition of the product requirements, and goals to achieve;
3. Study and critical analysis of design techniques used in existing equipment, that can be translated to the proposed housings;
4. Analysis and study of desired design methodologies;
5. Concept design and basic elements of the assembly;
6. Definition of desired material properties and material selection for the components;
7. Iterative design and virtual prototyping to optimize structural performance and component weight;
8. Selection of the best budget for outsourcing production;
9. Physical validation of the housings.

1.3 Report structure

In addition to this chapter, the report comprehends the following sections:

- Chapter 1: Introduction, aims to contextualize the problem that allowed this project to come to existence, as well as establish the objectives and structure of this dissertation.
- Chapter 2: Literature review, where every relevant topic for the development of the product is introduced and discussed. The state-of-the-art for those topics is reviewed and analyzed. The topics being discussed are *underwater vehicles*, understanding their purpose and how the industry has evolved thus far; main

techniques and methodologies applied in *product development*; and *mechanical design*, namely structural analysis methods.

- Chapter 3: This chapter portrays the development process. Beginning with the definition of the premise and requirements of the products, the initial design phases, material selection, final product design, structural validation, cost analysis and finally physical validation.
- Chapter 4: Conclusions and critical analysis of the development process of the housings.
- Chapter 5: Bibliography and other sources of information. Here are presented all the articles, books, and sites referenced throughout chapters 1, 2, and 3.

LITERATURE REVIEW

2.1 Underwater vehicles

2.2 Product Development

2.3 Mechanical design

2 LITERATURE REVIEW

2.1 Underwater vehicles

2.1.1 Unmanned underwater vehicles

Water environments such as oceans, rivers and lakes remain largely unexplored. Considering the operational costs and risk of having humans boarding underwater vehicles due to the harsh conditions of these environments, the development of underwater robotic vehicles is rising in popularity. Working underwater comes with a set of unique challenges. For example, metals that are usually reliable on air can easily corrode underwater. Also, the depth rate cannot be ignored. Since pressure changes associated with altitude are about one thousand times greater than in air, hydrostatic pressures can easily reach enormous values. Plus, structures need to be watertight to preserve their electrical components. Radio signals used for communication on land are nearly useless as they cannot penetrate water [4].

Unmanned underwater robotic systems can be divided in two main categories.

- The autonomous underwater vehicle (AUV) – Navigates autonomously via its navigation algorithm and surrounding information. After deployed they complete their predefined task and come back to the surface. This allows the vehicle high maneuverability and access to remote locations;
- The remotely operated underwater vehicle (ROV) – These types of vehicles are controlled remotely from the surface, usually via an umbilical cable that provides power and communication but limits their maneuverability and remote location accessibility [5].

The development and production of these unmanned underwater vehicles are currently facing several challenges concerning water wireless communications, battery autonomy, advanced manufacturing techniques, smart materials, compact on-board computers with high computational power for better decision making, and onboard energy generation and its efficient use [5].

2.1.2 Main applications and elements of an AUV

An AUV can be considered to have three main elements: body structure, propulsion system, and navigation system which is further discussed in section 2.1.3. Depending on its mission/application, AUVs structure and components may vary greatly.

The body structure of an AUV is where all the electronic and mechanical components are housed, and as such, it needs to be watertight and be able to withstand the water pressure. Its shape design is also very important considering that its dynamic movement is influenced by the fluid-structure interaction with the water it is submerged in [5]. Often AUVs are conceived for surveying applications where large areas must be covered and a good autonomy is required [6]. As such many AUVs take inspiration from submarine and torpedo designs that allow for better hydrodynamic efficiency and long endurance [3,4] as well as long range and depth capabilities [8]. Both the Maritime Research Institute Netherlands (MARIN) modular AUV (Figure 2 A) [9] or Sparus II [6] from the University of Girona follow this design.

Another major source of inspiration comes from aquatic animals. These bio mimetic AUVs can blend in with the aquatic environment to study and better understand its habitants. The shape of the vehicle built in the SABUVIS project was inspired by living fish (Figure 2 B) [10]. Also, AUVs like the Mantabot (Figure 2 C) try to mimic Manta rays due to their efficient swimming and high maneuverability [11]. These AUVs often do not employ the traditional screw propellers. In the case of Marcin et al [10] two servomotors synchronized oscillatory movements generate the undulation of the tail that propels the vehicle forward, along with pectoral fin's servomotors for directional control, generating less noise. This is ideal for applications such as aquatic life observation, oceanic supervision, undersea environmental monitoring, intelligence and surveillance, and reconnaissance. Another type of structure usually found in AUVs is the open-frame structure. When operating at low speed, since the drag force is smaller, AUVs often have open-frame structures, like the FeelHippo AUV (Figure 2 D) [5], [12].

The last few decades have seen an emergence of a new type of AUV. Still at an early stage, I-AUVs require the end-effector of the manipulator mounted on the vehicle to perform intervention tasks such as ship-and subsea pipeline maintenance underwater welding and oil and gas searching [3]. The MARIS project employed an I-AUV that successfully detected a pipe-like object, grasped it, and transported it using a customized three finger gripper [13]. I-AUVs require a more accurate and comprehensive model of the environment than other perception systems. Object models must include shape, position, and information on how to grasp it [14].

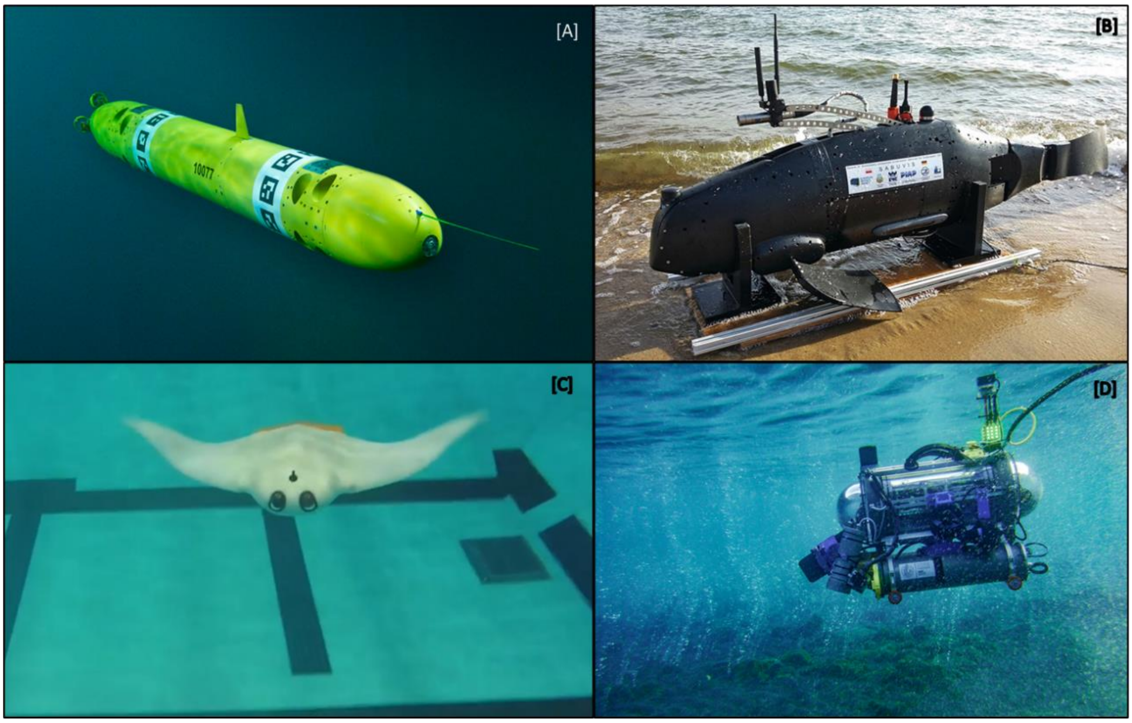

Figure 2. Torpedo shaped AUV: MARIN modular AUV (A) [15], bio mimetic AUVs: SABUVIS project AUV (B) [16] , Mantabot (C) [17] and open-frame structured AUV: FeelHippo AUV (D) [18].

2.1.3 Underwater navigation

Underwater navigation is one of the main challenges for AUVs. Navigation consists of determining the position and movement of a body relative to a known reference point, and planning and maintaining a course from one point to another [19]. Given that AUVs operate underwater, Global Positioning Systems (GPS) and high-frequency radio signals are not available, making localization and navigation very challenging for AUVs. Due to the complexity of marine environments the position accuracy deteriorates over time due to motion variations of the AUV and absence of an external reference. Generally, underwater navigation can be divided in three main techniques: inertial, acoustic, and geophysical. It is very common to see these techniques combined, capturing the individual strengths of each technique, and providing a more robust navigational solution [20]. In the next sections, these three techniques will be discussed.

2.1.3.1 Inertial navigation systems

Inertial navigation systems (INS) use a dead-reckoning navigation method. This method measures the travelled distance and direction. So, with a known initial position, it is possible to determine the current location relying on inertial sensors, and velocity and attitude measurements, as illustrated by Figure 3. This system requires no external infrastructure.

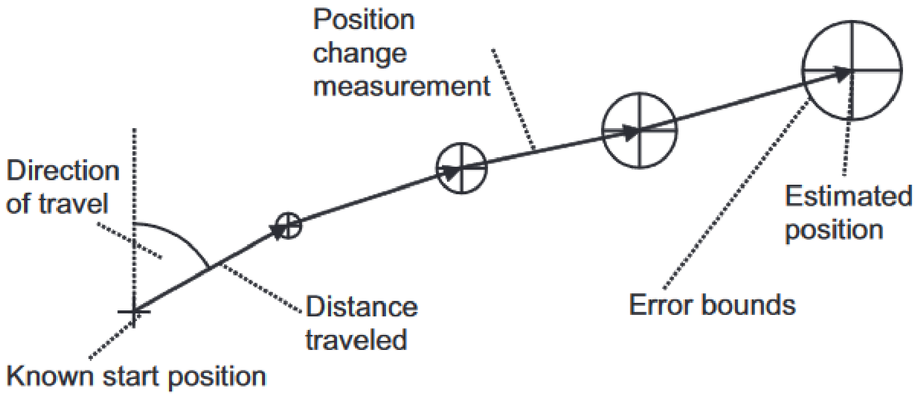

Figure 3. Principle of dead reckoning [19].

Usually, the inertial sensors consist of three accelerometers and three gyroscopes. The accelerometers measure the acceleration caused by all forces except gravity, allowing to measure the motion in the three directions of travel. On the other hand, the gyroscopes measure the attitude of the moving body, giving information on which direction the body is facing. Applying a gravity model to the specific forces, the acceleration is obtained. Integrating the acceleration gives the velocity solution, and integrating the velocity gives the position of the body [19]. Over time the measurement noise leads to increasingly less accurate positioning. The measurement noise can be attributed to the harsh and unpredictable conditions of the marine environment. There have been successful attempts to improve the accuracy of the navigational system by obtaining the vehicle speed using a doppler velocity log (DVL), as well as measuring the depth of the AUV with a pressure sensor (PS). The integrated system INS/DVL/PS, using a variational Bayesian method to approximate the measurement noise, has shown significant improvement in accurately representing the positioning of the AUV Sailfish 324 [21].

2.1.3.2 Acoustic navigation systems

Acoustic navigation systems are based on the use of transducers. These devices transform electrical energy into mechanical energy, generating a sound pulse. Usually, in underwater applications the transducer generates an omnidirectional sound wave that can be picked up by other transducers. The more popular acoustic navigation systems are (Figure 4):

- **Ultra-short Baseline** (USBL) – The AUV, equipped with a transducer, is located relative to a reference point, usually a surface fixed vehicle, that has an array of transducers. The position is resolved by the interaction between the two components [22]. This system is usually dependent on other sensors to accurately measure the position of the AUV. The accuracy of the system decreases as the distance between the reference vehicle and AUV increases [23].

- **Long Baseline** (LBL) – The LBL system deploys at least three transducers at three distinct and known locations in a wide area on the seabed. Then triangulates the position of a fourth transducer equipped in the AUV [24]. This allows for a wider area of coverage than USBL or SBL systems [25]. This method is very complex in terms of calibration, positioning, and recovering of the components [22]. GPS intelligent buoys equipped with a transducer can be used instead of placing the transducers on the seabed [5].
- **Short Baseline** (SBS) – Similarly to the USBL, this system utilizes a reference vehicle, but instead of having all transducers in an array, they are disposed in a triangular or rectangular shape underneath the reference ship. This system greatly benefits from transducer spacing, and as such operating from small vessels can compromise positioning accuracy. [25].

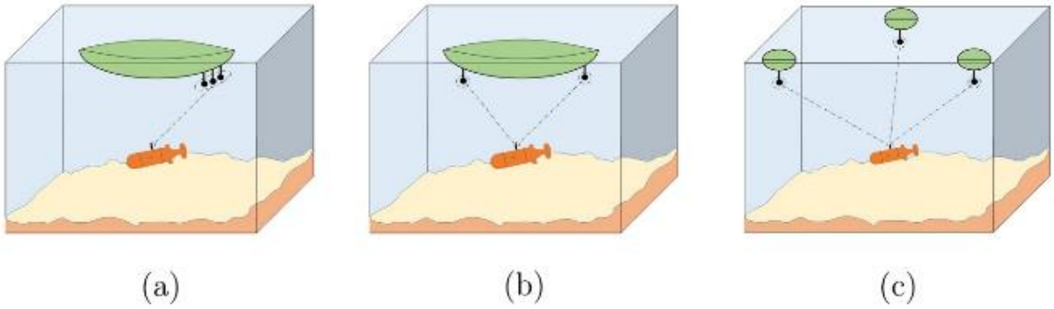

Figure 4. Acoustic navigation a) USBL; b) SBL; c) LBL (with GPS intelligent buoys). Retrieved from: Advancements in the field of autonomous underwater vehicle [5].

2.1.3.3 Geophysical navigation

Geophysical navigation utilizes the external environment features such as landmarks for localization. It matches sensor data to a prior map or terrain database, considering there is sufficient spatial variation for accurate localization. This technique does not rely on exterior devices, granting vehicles large operational ranges [20]. One of the two main categories of geophysical navigation are *sonars*.

Sonars make use of lower frequency sounds that can travel extreme distances in seawater, determining the range and reverberation of objects. Sonar technology is based around a transducer that receives sound from a source and, through a series of computations, determines the range and bearing solution. Sonar technology can be passive, relying only on "listening" (only receives acoustic signals), or active, which relies on "echo" (sends acoustic signals and reads its reflections) [25]. Sonars can be very helpful in conditions of turbidity and lack of illumination [26].

This technology has seen a wide range of applications. Lankowicz et al. [27] uses sonar technology to improve accuracy and reduce bias in determining the abundance and distribution of menhaden. Chen et al. [28] has determined that sound-based techniques can detect damage in underwater bridge structures. Pillay et al. [29] created a tool, ArcGIS, that uses machine learning to analyze geophysical data including multibeam bathymetry, backscatter, and side-scan sonar to map seafloor substrates. Figure 5 is an illustrative example of a multibeam sonar and side-scan sonar being used for seafloor mapping.

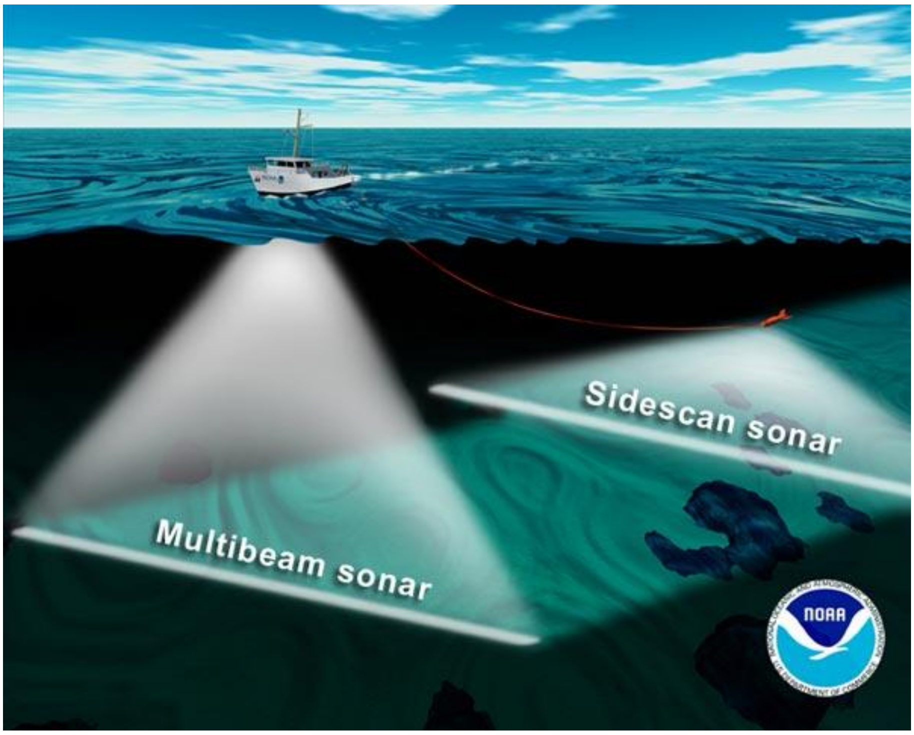

Figure 5. Illustration of a ship using a hull-mounted multibeam sonar while towing a side-scan sonar on a cable. Retrieved from: [30].

The other category is *optical navigation*. Due to environmental factors discussed in section 2.1.4, underwater imaging systems are only relevant in very close-range applications, like docking operations [20]. Nevertheless, these systems are seeing an increased demand in AUVs related to fisheries, environmental monitoring, inspection of offshore wind farms and oil&gas industry missions [31]. Three-dimension (3D) reconstruction systems are categorized as passive or active techniques.

Passive imaging techniques rely on light sources and photogrammetry. Essentially, passive techniques rely on multiple acquisitions under different points of view (POV) or different lighting conditions to retrieve 3D information [31]. Photometric stereo techniques are the easiest way of obtaining scene depth based on the triangulation of points of two different POVs [32]. To compensate for the passive systems dependence on the existence of features in the environment and susceptible lighting conditions, active systems are used to gather additional information to complement these passive optical systems.

Active imaging techniques use projected patterns of light using lasers for better light propagation in scattering mediums and to make beams highly collimated, allowing for better range acquisition. Distance between the target and device is measured by triangulation or time of flight (similar to sonars) [32]. Light stripe ranging is an active technique that consists of a set of laser stripes that are projected onto the scene. The structured light pattern is distorted by the nonplanar geometric shape of the surface. The information from the distorted light pattern is used to extract the 3D shape by triangulation, [33]. Pinto and Matos [31] used a hybrid optical system that employs both light stripe ranging and photometric stereo techniques to achieve 3D representations with high accuracy and precision. Structure from motion is another active technique that captures geometrical changes such as translation, rotation and orientation by pose estimation in motion, and delivers a 3D reconstruction of the object [34]. Recently deep-learning techniques have been applied in 3D recognition with impressive results. However, the scarcity of datasets constituting underwater environments means that applying deep learning approaches is challenging. To overcome this, Jeon et al. [35] used a dataset of 3D CAD (computer aided design) models to train the network.

2.1.4 Underwater perception challenges

The marine environment produces several challenging problems to the current underwater perception technology. The way light interacts with the underwater environment is different from air, making the imaging process harder. The three main phenomena that constitute a challenge to underwater imaging perception are absorption, scattering and refraction.

The absorption effect reduces the energy of signal light, transforming it into heat as it travels through the medium. The absorption rate depends on the wavelength. The maximum penetration/least absorption rate is usually in the blue/green spectrum, as illustrated in Figure 6. In ocean environments red wavelengths are absorbed within about 18 meters below the surface, yellow wavelengths about 100 meters, while blue/green wavelengths persist to about 244 meters [25]. This presents two main issues. One is that the color represented in the image does not accurately represent reality, due to different absorption rates. And two, artificial lighting is needed in most cases and image perception is greatly limited by the distance from the object [36]. One way of overcoming the absorption effects is by using stronger lights. However stronger lighting can deteriorate the image quality, because of the increase in backscattering [25].

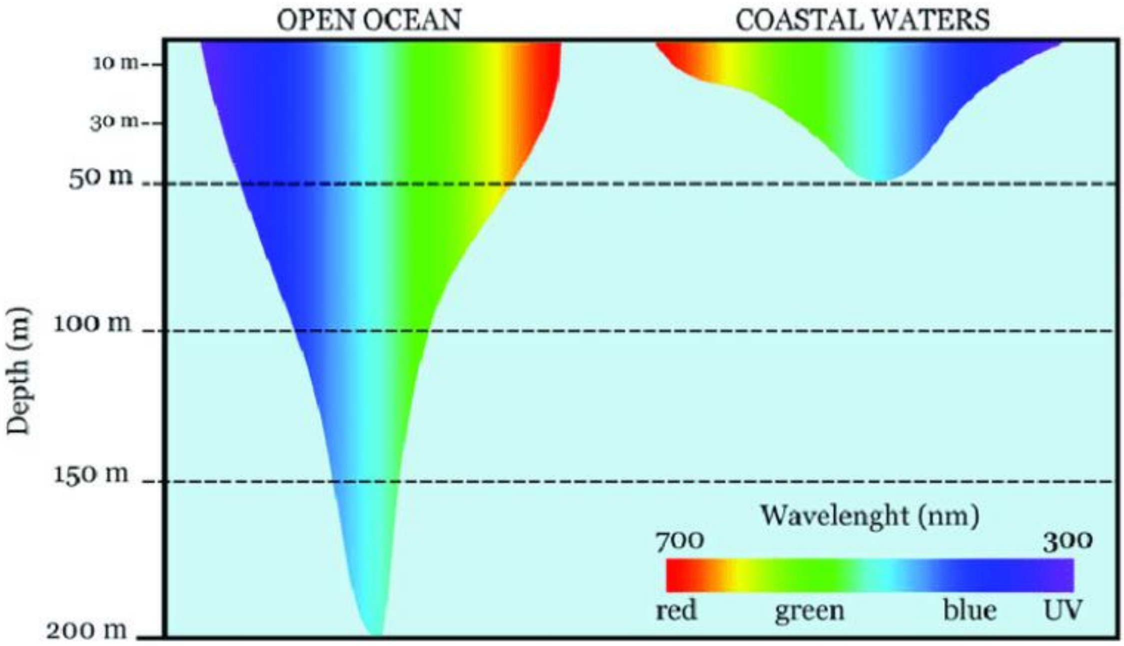

Figure 6. Light penetration in oceanic and coastal waters [37].

When a photon hits a suspended particle in water, its path is deflected. This phenomenon is known as scattering. Depending on the angle that the light ray is deviated, it can be known as forward scattering or backscattering. When the angle is small, it is called foreword scattering, and results in image blurring and loss of contrast. If the light ray is reflected to the camera before reaching the object, then it is backscattering (Figure 7). This results in bright points in the image, known as marine snow. It also causes what is known as path radiance, which leads to a high loss of image contrast [36]. In high turbid water, light intensity may have to be reduced in order to gain any visibility (like fog lights in a car). Another solution is to separate the light source from the camera. That way the column of water in front of the camera is not illuminated, reducing backscattering [25].

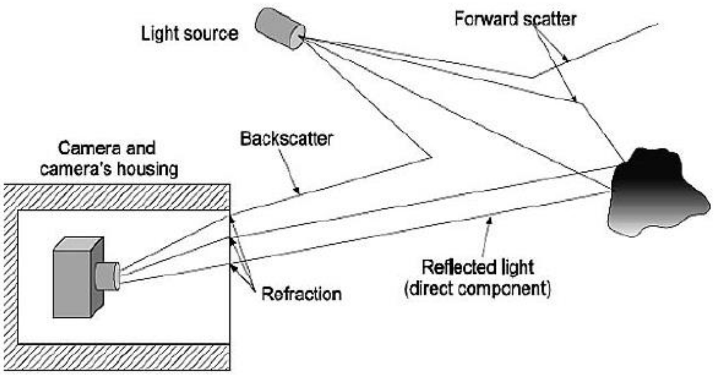

Figure 7. Example of backscatter, forward scatter, and refraction [36].

Light refraction occurs when a light beam moves through one medium to another. Refraction causes the light to bend, when it goes from water to glass, and again from glass to air in the case of underwater cameras. Therefore, it is required that the system is calibrated to counter the refractive effects from both mediums. Otherwise, the system may suffer from focus, field of view and/or distortion errors [36]. These errors are caused by the misalignment of the camera and its housing/interface projection centers. Using a hemispherical interface (dome) can help decrease the refractive effects. As illustrated in Figure 8, a hemispherical interface can align the projection centers mentioned before, thus improving the accuracy of the captured image [38].

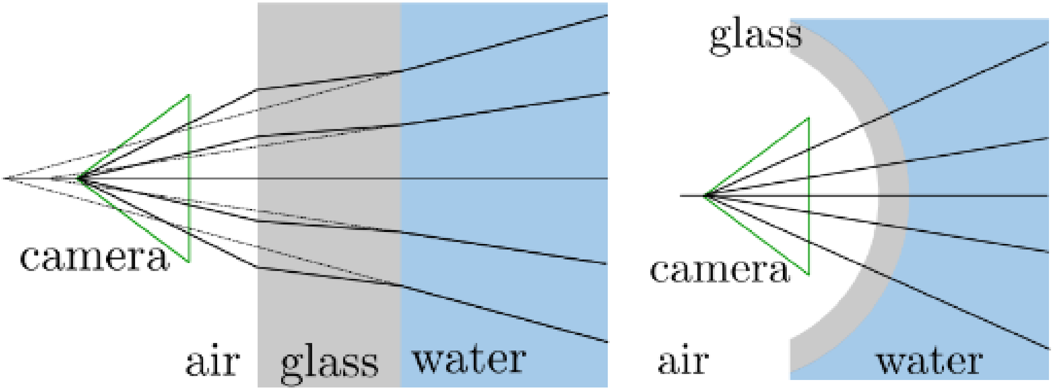

Figure 8. Refraction of light rays at flat (right) and dome ports (left) [38].

2.1.5 Project solutions

Underwater vehicles need to be able to withstand significant hydrostatic pressures while remaining watertight. The most common materials used in underwater robotics are titanium alloys, aluminum alloys (5083, 6082 T6, 6061 T6, 7075 T6, A356), stainless steel alloys (316, 630, 660), some plastics [39], and composites materials like fiber reinforced plastics (FRP) [40] or even hybrid materials like AW/CRFP (Aluminum/Carbon FRP) [41]. These materials present good to excellent corrosion resistance and relatively high strength to weight ratios. Smart materials are also seeing an increased interest in soft robotics due to its super elasticity and shape memory effect. This makes them ideal to simulate some of the more complex motions found in biomimetic AUVs [42].

A great effort is put into optimizing hull shapes to minimize drag forces and thus, optimizing energy consumption, allowing for greater periods of operation. Ignacio et al. [43], used computational fluid dynamics (CFD) and empirical methods to achieve optimal parameters concerning the protection of internal hardware, buoyancy and drag reduction . Other works that use CFD for hull shape optimization can be found in references [7,38,39], proving that CFD can be a powerful tool in designing AUVs.

Acrylic plastic is one of the more commonly used materials in underwater viewports. Zhu et al. [46] studied the strength and stability of spherical pressure hulls, considering a plane disk, a conical frustrum and a spherical shape using finite element analysis (FEA) through ABAQUS, a computer aided engineering (CAE) software. Gelli et al. [47] also used FEA to determine static stresses in their AW 6082 T6 housing and frame (two sheets of carbon fiber connected by supports in Polyoxymethylene (POM)) components. Other applications of FEA studies in AUV design can be found in references [34,35,42,43,44].

Due to the variability of missions and applications, the AUV industry has seen an increased interest in modular design. This approach enables easier manufacturing and maintenance, as well as higher flexibility and customization [51]. The MARIN AUV [9], MARTA [52], and Bluefinn-21 [53] are some examples of AUVs that follow this design methodology.

2.1.6 AUV industry

Due to the nature of the missions performed by AUVs they are usually costly, and so they are not of very easy access to the general public. However, there are some companies that have a big presence in this industry. In Table 1 some of the leading companies of underwater robotics industry are presented.

Table 1. Leading companies in the AUV industry

Teledyne Marine [54].	Teledyne Marine is a group of subsea technology companies. They provide products related to imaging, instruments, interconnect, seismic, and vehicle technology. Their AUV solution is the Gavia, a modular AUV available for 500 and 1000 m. Modularity allows it more flexibility in its applications, and ease of upgrade, as well as maintenance.
SAAB Seaeye, subsidiary of SAAB [55].	SAAB Seaeye supports a vast range of sectors across commercial, defense and scientific markets. They have a large range of AUV/ROV solutions as well as components, like thrusters, light emitting diode (LED) lamps, electric manipulators, amongst others.
ECA Group [56]	ECA Group provides long-endurance AUVs up to 3000 m. They have solutions for pipeline inspection, platform surveillance, search and rescue, among other applications.

BlueRobotics [57]	BlueRobotics is dedicated to developing components for underwater robotics, like cameras, sensors, thrusters, enclosures, and many others. They also have a ROV solution in the form of the BlueROV2.
MacArtney Group [58]	Like BlueRobotics, the MacArtney Group is more dedicated to developing underwater technology components, like subsea cables, connectors, fiber optic telemetry, underwater cameras, amongst others. They also have several towed ROV solutions.

2.2 Product Development

2.2.1 General concept

Product development is the transformation process that leads into the introduction of new products as a response to a marketing opportunity, by combining a logical set of activities [59]. *Marketing* is one of the three most central functions to a product development project. The marketing function facilitates the identification of product opportunities, market segments and costumer needs. It mediates the interaction between the developer and costumers. Another central function is *Design*. It defines the physical form of the product to meet product requirements. This function includes both engineering (product-working functionality), and industrial (human-using functionality) design. Lastly there is *Manufacturing*, primarily responsible for the production of the designed product. It encompasses designing, operating, and coordinating the production system [60].

2.2.2 Material selection

Material selection is vital for the success and competition of a product. The goal of optimum product design is to attain the maximum performance for the minimum cost while meeting the design needs. Due to the increasing choice of materials and manufacturing processes, material selection is more complex and challenging than before [61]. Generally, material selection is motivated by performance improvements and cost reduction. However, there are other criteria that influence the decision, depending on the end goal of the product (e.g., in the aerospace industry, weight reduction is one of the main targets). Multi criteria Decision-Making (MCDM) tools are usually applied to reach an optimum decision when faced with multiple decisions [62]. A varied number of MCDM methods have been developed to address the issue of material selection and increase the efficiency in the design process [61]. For the scope of this work, only the Ashby method is reviewed. For a more detailed review of MCDM methods refer to Table 1 in reference [62].

Following the Ashby method (Figure 9), the first step (translation) in material selection is converting the design requirements into constraints and objectives. Second (screening), the materials that do not meet the requirements are eliminated from the selection process. The third step (ranking) ranks the surviving materials that meet the design requirements and finds those that maximize performance. The last step (documentation) consists of exploring the final candidates in depth, how they are currently used, material reputation, and availability, leading to a final choice [63].

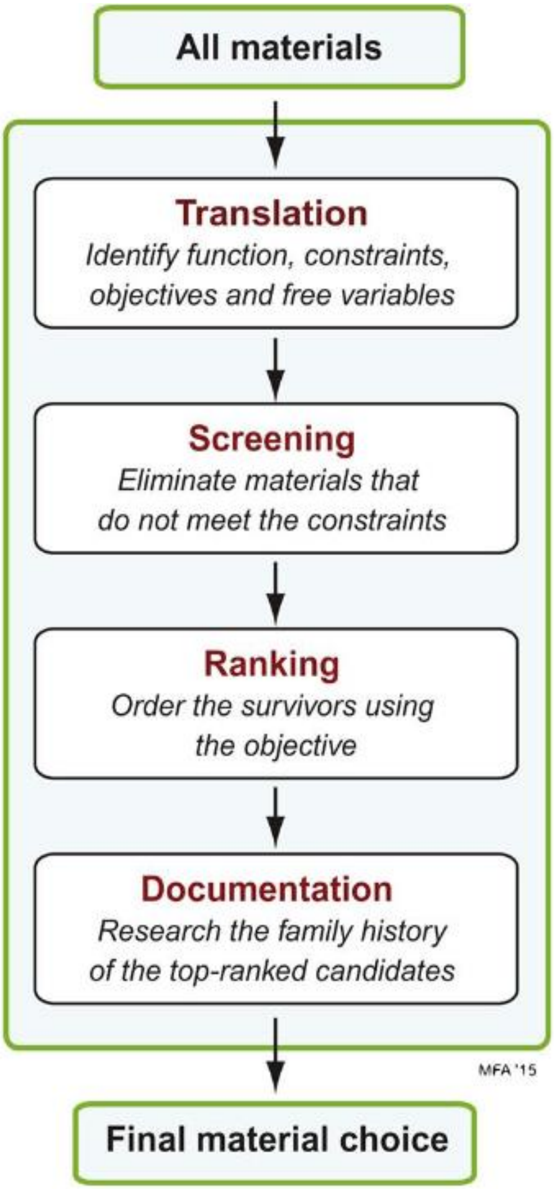

Figure 9. The four main steps in Ashby methodology for material selection [63].

During the ranking process, competitive properties are assigned a weight (w_i) relative to their importance to the design. Next, to calculate the value of the weighted index (W_i), the material indices (M_i) are scaled in two ways:

- If maximization is the desired goal, then:

$$W_i = w_i \times \frac{M_{max}}{M_i} . \tag{1}$$

- Otherwise, if minimization is the desired goal, then:

$$W_i = w_i \times \frac{M_i}{M_{min}} . \tag{2}$$

Last, all the W_i are summed. The material with the highest ranking ($\sum_{i=1}^{n} W_i$) is considered the best option [63]. In the work of Rashedi et al. [64], the Ashby selection method was used to determine the best option for a wind-turbine blade. The authors analyzed the mass, carbon footprint, cost, and embodied energy consumption minimization, and assigned a w_i of 50%, 20%, 20%, 10% respectively. These w_i were arbitrated with support from established norms and industry-based knowledge in the design of wind-blades. The authors calculated the W_i, and determined that carbon fiber reinforce injection molded Polyetheretherketone (PEEK) allowed for a 74% weight reduction in weight, decreased the embodied energy by 30% and the atmospheric carbon dioxide emissions by 17%, with only a 70% increase in price. For more details about the material selection approach of this paper refer to table 1 in [64]. In Table 2 some works are referenced where the Ashby selection method was utilized with success.

Table 2. Compilation of works that use the Ashby material selection method.

Authors/reference	Work description
Mehmood et al. (2018) [65].	Material selection for Micro-Electro-Mechanical-Systems (MEMS) review of the last 20 years show that the Ashby selection method is the most frequently used in MEMS devices. Ashby method proves to give accurate results when applied to micro-scale material properties.
Chauhan and Vaish (2013) [66].	Hard coating material selection using various MCDM approaches. Comparison between TOPSIS (Technique for order preference by similarity to ideal solution) and Ashby method shows that both techniques are efficient in selection and screening of hard coating materials.
Oliveira et al. (2012) [67].	Ashby approach for material selection in polymer electrolyte membrane fuel cells. Results evidenced that the Ashby approach is a reliable method to assist in selecting the best performing materials for bipolar plates.

2.2.3 Product development main stages

According to Ulrich [60], generic product development goes through six stages. Phase zero, *planning*, consists of opportunity identification, assessment of technology developments and market objectives.

In phase one, *concept development*, costumer needs are already identified, and alternative product concepts have already been generated and evaluated. One or more concepts is then selected for further testing and development [60]. Franco et al. [68] focused on mountain farmers whose needs had not been met by advances in agricultural mechanization. The authors analyzed the role of mountain agriculture worldwide and in Italy, identifying an economic justification. A state-of-the-art analysis of similar products was initially done as a starting point for the product design.

Phase two is system *level design*. It defines a preliminary design of the product's key components, as well as the geometrical layout of the product, and key components and functional specifications of the product subsystems. Plans for the manufacturing and final assembly also begin in this phase.

This leads to phase three – *detailed design*. This phase includes the complete specification of geometry, materials, and tolerances of the product system and subsystems. Standard parts are also selected to be purchased from suppliers. Imran et al. [40], in the development of an egg shaped hull, conducted a FEA analysis to optimize the number of layers and orientation angles between five lay-up configurations using three different unidirectional composites. Based on the results the authors were able to infer what material and lay-up configuration could better suit their needs.

Phase four consists of *testing and refining*. The construction and evaluation of multiple versions of the product (prototypes) is tested to see if the design is working as intended and the customer requirements are met. This evaluation identifies necessary engineering changes for the final product. Butchers et al. [69] captured the local requirements of the solution (technical, social, economic, political and natural) to support design for localization of a low head propeller turbine in Nepal. The authors adapted design solutions for local manufacturing and conducted a local research and field-tested to ensure product suitability. The result was a product better suited for the local market's needs, supporting local businesses in developing their own design and manufacturing, and encouraging repair rather than replacement.

Finally phase five begins the *production ramp-up*, here the product is manufactured using the intended production system, and the workforce training begins. It is during this phase that the remaining problems that arise from the production process are fixed, gradually transitioning to on-going production.

2.2.4 3D modeling

Over the years, with computer performance improvements and more accessible hardware prices, 3D modeling has become a key technology in many, different areas. Current engineering groups, from design, physics-based analysis, and manufacturing, all work from a common database, the solid model [70]. Boundary Representation (BREP) is one of the more dominant 3D representation schemes in mechanical CAD systems. This technique uses sets of connected geometrical elements to represent vertices, edges and faces that define the boundary of a solid (Figure 10). The geometric information defines the exact shape and spatial position of these elements, and topological information defines how these elements are linked [71].

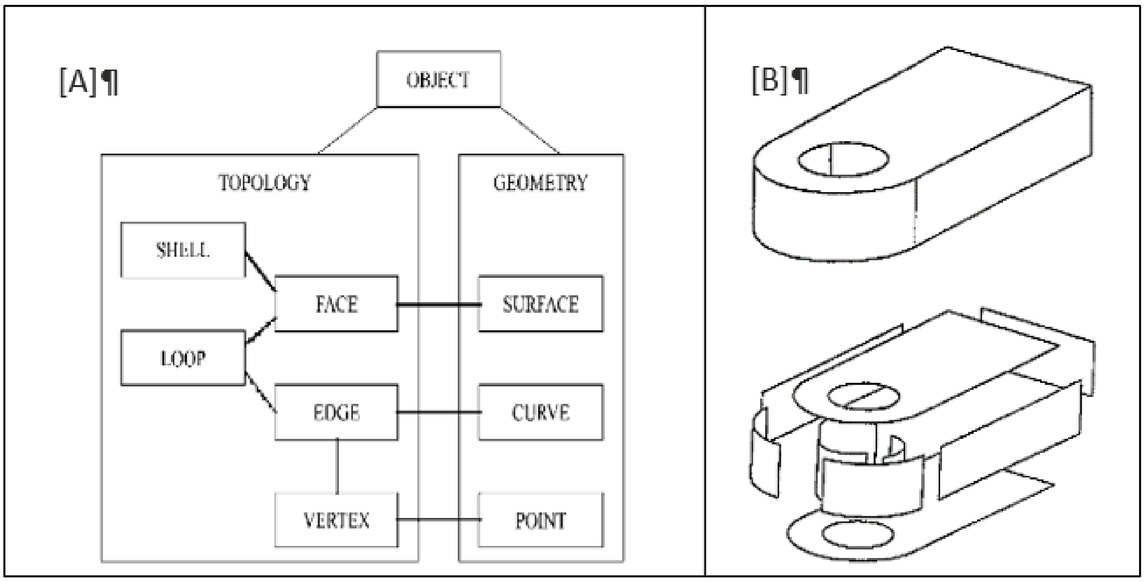

Figure 10. Basic elements of a data structure [A], and Representation of a solid model with BREP [B] [72].

2.2.5 CAD/CAM software

CAD/computer aided manufacturing (CAM) has widened the scope of traditional design and manufacturing. These systems have applications in both the design of a product and programing the manufacturing process, with Computerized Numerical Control (CNC) machines. It is used to design and manufacture prototypes, finished products, and production runs of products [73]. From a design perspective, geometric properties and interactions between parts can be accurately calculated with no need to build physical models. 3D models can be quickly and easily transformed to 2D views, allowing for faster and more accurate technical drawing. Modifications are easy to make, allowing greater design freedom, and changes made to the 3D model will automatically transfer to the 2D drawing. 3D visualization can also be a more effective tool for communication. The manufacturing activity is processed by the computer, often with integrated diagnostics and monitoring facilities, leading to increased productivity, shorter lead times, and better management control. Also, less maintenance is required when compared to traditional methods. Since CAM systems provide a better manufacturing method and controls than traditional ones, they can achieve better quality in the manufactured parts [74]. Some of the more popular software that offers both CAD and CAM solutions are found in Table 3.

Table 3. CAD/CAM software solutions.

SOLIDWORKS® by Dassault Systèmes [75]	SOLIDWORKS® is a CAD software, however a CAM and CAE solution is also available in the form of an add-on.
Fusion 360® by Autodesk [73]	Fusion 360® is a cloud-based software with integrated CAD/CAM/CAE platform.
Creo® by PTC [76]	Similarly to SOLIDWORKS®, Creo is also a CAD software that offers CAM and CAE extensions.
CATIA® by Dassault Systèmes [77]	CATIA® is a multi-platform software that offers CAD/CAM/CAE solutions.

2.2.6 Rapid prototyping

Rapid prototyping or additive manufacturing, also known as 3D printing, is a rapidly growing technology. It utilizes 3D CAD data to quickly fabricate a model or fabricate a replacement part [78]. Using a CAD file, usually standard tessellation language (STL) as an input, 3D printers can manufacture complex 3D models in a layer-by-layer process. 3D printing allows for reconfigurable manufacturing without changing the process [79]. This process can save time and money while allowing for good aesthetics to customized products [80].Although many different plastics/polymers are available for 3D printing, there are other materials, like metals, that are attracting some attention in the industry (Figure 11). For a more detailed analysis on which materials are being used in addictive manufacturing refer to reference [81]. Rapid prototyping has seen applications in many different industries such as: aerospace, medical, automotive, construction, and art [82]. Able to reduce lead times of product development, rapid prototyping is quickly becoming an alternative method of fabricating components. However, this technology cannot yet match the dimensional accuracy, surface roughness and part strength of traditional manufacturing processes [83].

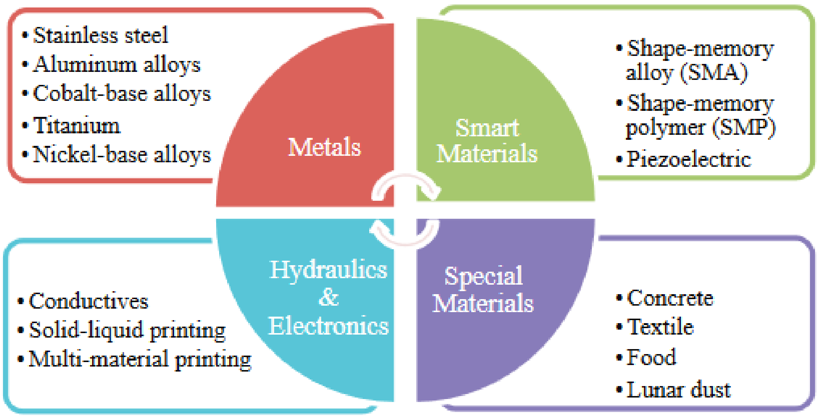

Figure 11. Overview of current research materials for Additive Manufacturing [81].

2.2.7 Reverse engineering

Reverse engineering (RE) is the process of analyzing a subject system to identify the system components and its relationships, to create a representation of the system in another form or at a higher level of performance. From a mechanical design standpoint, it consists of analyzing, testing, experimenting, and documenting a product to assess its functionality, form, manufacturability and assemblability, and to understand how a product works. The obtained knowledge from this process allows the development of a surrogate model with similar or improved performance [84]. Manual repairs are time and labor intensive and produce inconsistent quality. Li et al. [85] proposes a RE methodology to aid in the remanufacturing of worn parts. The methodology presented integrates 3D model reconstruction via surface data collected from optical devices, fine registration, extraction of additive/subtractive repair, tool path generation and machining process. The proposed approach is proved effective and efficient by successfully remanufacturing a used forging die and a worn gear bracket. Zivkovic et al. [86] scanned a Kaplan turbine blade from a scaled model manufactured in the 70's using an optical scanner. From the produced STL model, the blade surface was redesigned eliminating all damages and deformations. Although in their paper, the proposed process showed some limitations regarding the non-smoothness of the boundaries of the shapes, and sampling from rough surfaces. T the implementation of data mining for shape generation and RE topology optimization this method could potentially overcome these limitations by smoothing out the extracted surfaces. Engel et al. [87] used a laser scanner, analytical calculations, and FEA to obtain the 3D CAD model, material type, manufacturing process, and surface characteristics to recover the original design specifications of a shaft of a rotary draw bending machine. It was observed that the recovered shaft had a similar mechanical behavior, however it was suffering from wear and pitting, requiring new machining to attain the desired surface roughness, and carburizing processes to harden the steel.

2.2.8 State-of-the-art in product development methodologies

The following techniques were applied in the papers presented in Table 4:

- **Lean design** has been witnessing an increasing implementation with the increase of customer requirements and competitive environment. Lean design is based on lean thinking, with a primary focus on creating value for the end-costumer and minimizing waste throughout all stages of product lifecycle by optimized product design. Activities that do not contribute towards this goal are considered waste. The aim of lean design is to minimize all non-value-adding but necessary activities, thus increasing the effectiveness of these activities [88].
- **Design for X (DFX)** or design for excellence follows some essential principles of lean design. However, DFX focuses on improving aspects of a specific stage of product lifecycle. The X may stand for manufacturing, assembly, quality, reliability, cost, usability, maintainability, sustainability, amongst many others. DFX techniques aim to support designers by supplying guidelines for product development and improve or maximize aspects with respect to X [89].
- **Prototyping** can be an essential tool in the early stages of product development to design, communicate, build, and test new concepts and ideas. Prototypes can be an efficient and fast way of obtaining answers and knowledge as well as exploring alternatives before converging on a concept to develop further [90].
- **Artificial neural networks (ANN)** are seeing an implementation rise in product development. ANN are widely used for engineering predicting problems due to its powerful non-linear mapping, self-learning, and self-adaptability. These algorithms can determine relationships between data and results of a large amount of data [91].

Table 4. Compilation of product design focused papers

Baptista et al. (2018) [92].	This paper presents the design of a press-brake with a lean DFX approach, integrating eco-design principles, design for structural optimization, and modular design. The authors measured effectiveness of selected variables (e.g., weight) with ratio measures from the distance to the design variable target, with 100% meaning the target was attained. Efficiency rates are measured by how much the variable exceeds the target, thus generating waste according to lean principles. In the end the authors measured an overall effectiveness of 78% and efficiency ratio of 83%. These indicators successfully allowed the identification of areas where the product needs improvement or correction, and the use of scorecards led to a more intuitive representation, which helped supporting decision making by the developing team.

Korsmik et al. (2020) [93].	This paper explores several aspects of addictive manufacturing via direct laser deposition of marine parts. The sharp temperature gradient near the deposited layer causes non-uniform thermal expansion resulting in distortions. The distortion compensation consisted of inverting the predicted deformations via FEA and modifying the original model to produce the desired shape, showing satisfactory results. Despite the material cost for direct laser deposition being higher than in traditional methods, the better material utilization rates and less labor outlays prove that this technology can be very attractive in the design of marine machine parts.
Saldaña-Robles et al. (2020) [94]	In this work, the conceptual design of an agriculture backhoe was obtained through a reverse engineering analysis of commercial backhoes. A structural analysis was done by a FEA using a CAE software. The simulation was validated by comparing the results to a theoretical analysis. Statistical techniques were used to study the effect of thickness and dimensions of some components on its mass reduction, safety factor, and von Mises stress, leading to a smaller number of tests. In combination with an artificial neural network, the solution time was further reduced.
Aufluem et al. (2019) [90]	This paper presents a prototype driven approach in early-stage product development. The authors present two case studies: resuscitation mannequins and leg repositioning mannequin. Prototypes enabled communication between expert users of the medical field and the engineering team, to determine needed functionalities and important aspects of the design. By extensive prototyping, the development teams were able to adapt and test often, making informed decisions and quickly launch proof of concept prototypes to gain feedback.

2.3 Mechanical design

2.3.1 Structural analysis methods

Structural analysis consists of determining the resulting displacements and deformations of a body subjected to a load. There are three different methods to conduct this type of analysis:

Strength of materials (classical method). Dating back to Galileo who first explored this field, strength of materials lays the foundation of structural analysis. This method provides easy to obtain solutions, usually done by hand. However, it fails to solve problems of more complex geometry [95].

The theory of elasticity consists of a set of 15 equations based on stress-strain relations, equilibrium equations, Hooke's law, and compatibility relations. For most 3D problems, this method poses such a high complexity that analytical solutions are practically impossible [96].

Lastly there are the **numerical methods**. The other two mentioned methods are not viable to solve most problems or require very complex solutions. Numerical methods emerged due to those issues. Numerical methods usually work with body discretization. This process consists of replacing the original model by a series of smaller elements. This allows to obtain an approximate solution, where the error is minimized by increasing the number of elements used to describe the original model [97]. The most popular numerical method for solid mechanics is the finite element method (FEM).

2.3.2 Finite element method

In FEM, a continuum body of mater (solid, liquid or gas) is represented by a series of smaller subdivisions called elements. This process is called discretization or meshing (Figure 12). These elements are interconnected at specific joints called nodes. Nodes usually lie at the element boundaries where adjacent elements are connected. The variation of the field variable inside the continuum is unknown, so it is assumed that the variations inside the element are approximated by interpolation functions. The FEM equations unknowns are the nodes values of the field variable. By solving those equations, usually in the form of matrix equations, the values of the field variable at the nodes are known. Then, the interpolating equations solve the values for the rest of the elements. The FEM approach is not only limited to structural analysis. A reason FEM is so popular is the wide range of problems it can be applied to. Several other engineering problems can be solved by FEM, such as heat conduction, fluid dynamics, seepage flow, and electric and magnetic fields [97].

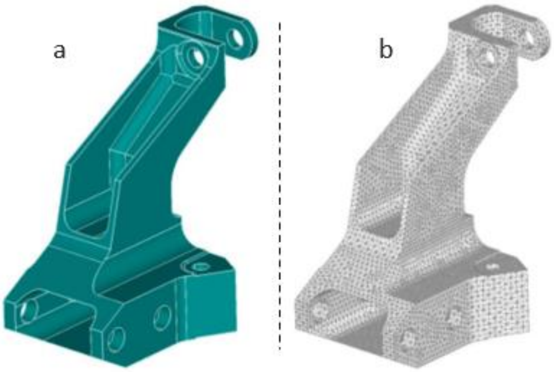

Figure 12. Example of a continuum body (a) and the same body discretized (b) [98]

Mesh manipulation is a fundamental aspect of FEM, since a more refined mesh is expected to deliver a more approximate solution to the exact value. However, as the mesh density increases, so does the computational time. For maximum efficiency it is the interest of the engineer to apply an adequate mesh. In areas where stress concentration is expected, the elements should be smaller than in areas where the stress gradient is not so steep [97]. To ensure that the solution from the numerical simulation is not mesh dependent, a convergence study is conducted. When predicting the ultimate strength of corroded plates with center longitudinal crack, Ahmadi et al. [99] conducted a converge study to determine how many elements could ensure an adequate solution. Figure 13 shows the ratio of ultimate stress to yield stress for a square intact plate with dimensions of 0.6×0.6×0.01 m^3 for different numbers of elements. For a number of elements above 120 the given solution remains steady, showing that the solution is converging to the exact solution, meaning that the study achieves mesh independency for an element count above 120.

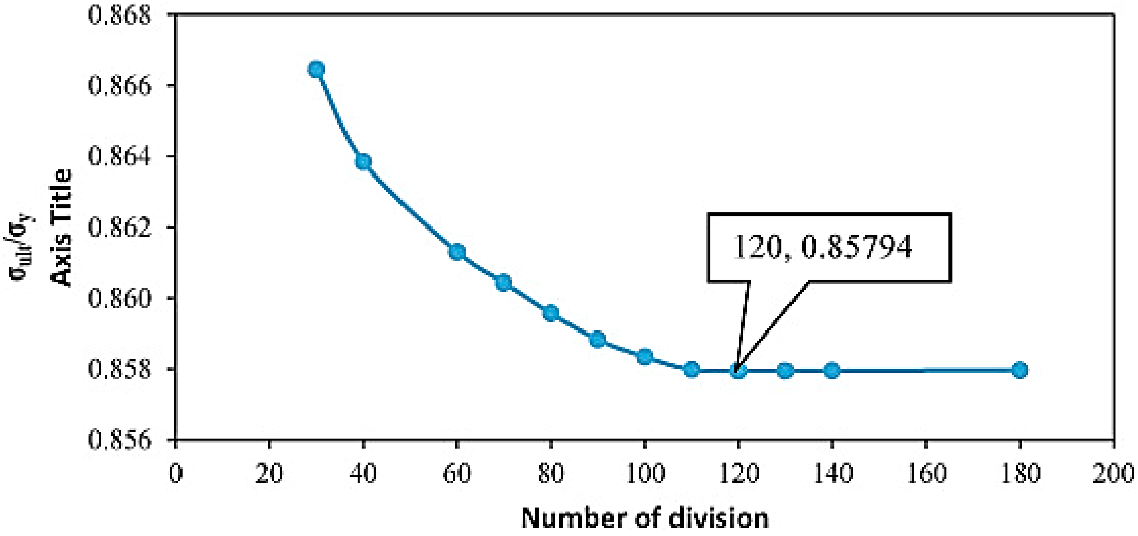

Figure 13. Convergence study on ultimate strengths of an intact plate with different number of elements [99].

2.3.3 Finite element *software*

FEM is the most frequently utilized computational tool to design structures. However, this was not always the case. When it first started, in 1956, manual computations were used as well as the force method, instead of the displacement method used nowadays. Specialized computer programs emerged in the 1960s, and commercial software only became available around the 1970s when computers started to become more available [100]. Today there is a wide array of commercial software able to perform FEM, including those already mentioned in Table 3. Some other available and popular software are presented in Table 5.

Table 5. CAE software solutions.

ANSYS Mechanical® by ANSYS [101].	ANSYS is one of the most popular CAE developers. They focus solely on developing CAE software, and offer many products for different fields, including FEM with ANSYS Mechanical®.
Abaqus/CAE- Simulia® by Dassault Systèmes [102].	Abaqus/CAE-Simulia is Dassault Systèmes more advanced CAE software. It offers solutions to a vast spectrum of engineering problems with FEM.
COMSOL Multiphysics® by COMSOL [103].	The Structural Mechanics module is an add-on of COMSOL Multiphysics® that uses FEM to analyze the mechanical behavior of solid structures.

2.3.4 State-of-the-art of projects that incorporate finite element analysis

FEM is still a very big subject in research literature. This research is usually focused on new FEM based techniques, that cover some of the FEM weaknesses, like the scaled boundary FEM usually applied in fracture mechanics [97,98], or the applied element method (AEM) which has shown great success and better performance modeling the collapse of structures. Figure 14 shows how deformations are considered between FEM and AEM, illustrating why the AEM method succeeds in simulating collapse [106]. Mesh based techniques have significant disadvantages in the areas of modelling free surfaces, deformable boundaries, moving interfaces, crack propagation and large deformations. As such, meshfree methods, based on the interactions between the nodes, instead of its elements boundaries, are seeing an increased interest by researchers as a solution for those issues [107]. Despite its limitations, FEM is still a very reliable tool in most engineering fields, especially to study solid content. Plus, it has been extensively used for many years, and the software is usually more user-friendly, containing a user interface for modelling, simulation, and visualization. Table 6 contains some projects that use FEM.

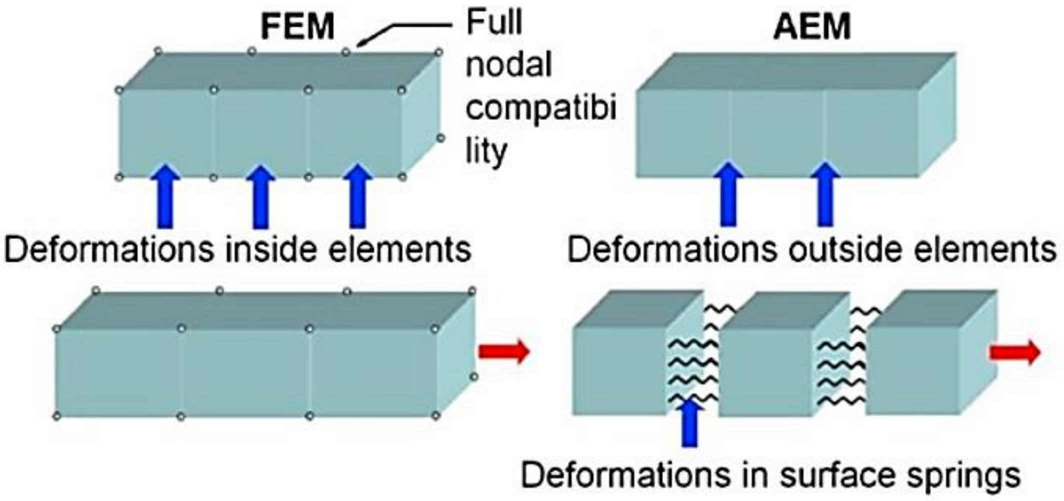

Figure 14. Comparison between how deformations are considered in FEM vs applied element method [106].

Table 6. Compilation of works that use FEA.

Synek et al. (2021) [108].	In this paper the authors used FEM to analyze volar plate fixation of distal radius fractures, with the purpose of determining if using fewer distal screws was biomechanically feasible, and if optimum screw configuration was subject-specific. 42 configurations were compared for 16 subjects. Based on the FEM optimization study, the authors determined that the ideal screw configuration is subject-specific and, on average, 1.9 screws could be saved based on the optimization criterion used. Screw configuration showed to be more relevant than the number of screws, as some configurations with three screws showed a better performance than configurations with five.
Tuswan et al. (2019) [109].	The authors used FEM to evaluate the application of sandwich plates on the structural strength of a ship hull. They analyzed the influence of different core types, core thickness, and stiffener configurations. The authors were able to achieve lower stress and deflection values when compared to an existing model, proving that FEM can be an effective tool to analyze different configurations of sandwich plates.

Deng et al. (2021) [110].	In this paper, the FEM was used to optimize design geometry and power output of a radioisotope thermoelectric generator for terrestrial use. From the analysis, the authors were able to conclude that the octagonal cylindrical shaped electrical heater had better performance than cubic and cylindrical heaters, and that the fin shaped radiator could dissipate heat at its optimum heat-sink capacity. The results were tested experimentally with promising results, proving that FEM is an effective tool to predict and simulate the performance of radioisotope thermoelectric generators.
Vivekanandan et al. (2019) [111].	The main aim of this work was to design and analyze a pressurized vessel working under varying operating conditions and to identify the most contributing parameter that controls the efficient working of the oil tank. The design followed de American Society of Mechanical Engineers standards, using the PV-ELITE software and manually calculated design values. PV-ELITE results were then validated using FEM. The results were agreeable, with a percentile error of 4,99%.
Nandhakumar et al. (2020) [112].	In this paper, two different aluminums (al 6061 T6 and al 7075 T6) were considered to replace the structural steel (Steel A709M grade 345 W) chassis frame of an electric bus. FEM was conducted to determine the performance of the three materials. The results showed that by using al 7075 T6 a weight reduction of 64.33% could be achieved leading to better endurance of the vehicle battery, showing that FEM can aid in the process of material selection.

DEVELOPMENT

3 DEVELOPMENT

3.1 Company presentation

INESC-TEC is a private non-profit research institution dedicated to scientific research and technology development, technological transfer, advanced consulting and training, as well as pre-incubation of new technology-based companies. INESC TEC operates at the interface between academia and business worlds, applying the knowledge and results generated via research in technology transfer products, generating value and social relevance.

As of March 2021, there are thirteen research and development centers of INESC TEC present in the cities of Porto, Braga, and Vila Real dedicated to four thematic domains – Computer Science, Industrial and Systems Engineering, Networked Intelligent Systems, and Power and Energy.

The present work is being developed in FEUP at the center of robotics and automation systems facilities (CRAS). The CRAS center's mission is to develop innovative robotic solutions for complex environments. The investigative focus of the CRAS center is in areas such as autonomous navigation, long term missions, mapping and intervention, and multiple platform operations. The CRAS center has access to two laboratories in FEUP and ISEP, equipped with the necessary equipment to test the developed technology. Between both sites there are two pools, a hyperbaric chamber, and dedicated workshop rooms for manufacturing and storage of underwater and electronic equipment.

The CRAS center is involved in numerous maritime robotics projects. This dissertation's work is comprehended within the ATLANTIS project [113]. This ongoing project is funded by the European Union's horizon 2020 research and innovation program, and aims to reduce the levelized cost of energy, by providing a testing and development platform (Figure 15) of maritime robotics and autonomous systems to perform inspection and maintenance operations at offshore wind farms.

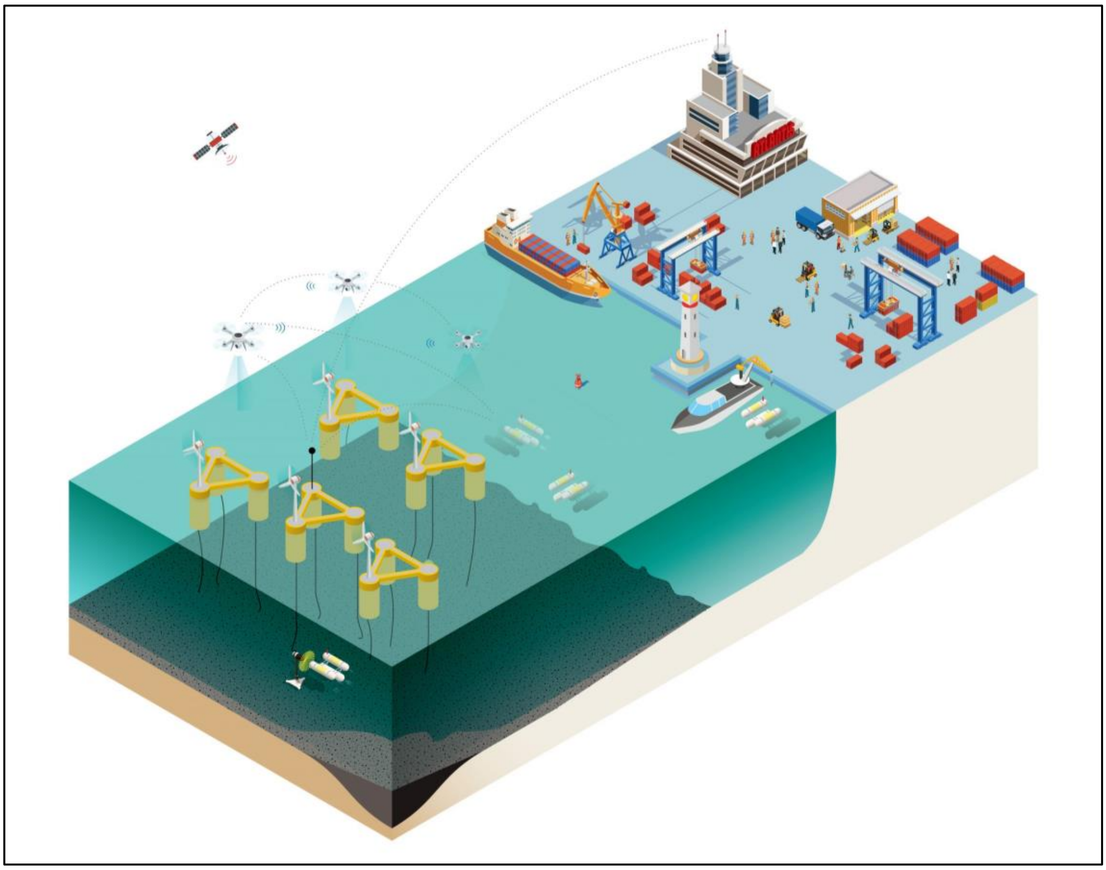

Figure 15. ATLANTIS test center [113].

3.2 Main objectives and initial considerations

The proposed work aims to design, develop, manufacture, and validate two AUV components – an imaging perception system housing (IPSH) named MARESye, and a wireless charger housing (WCH) (Figure 16).

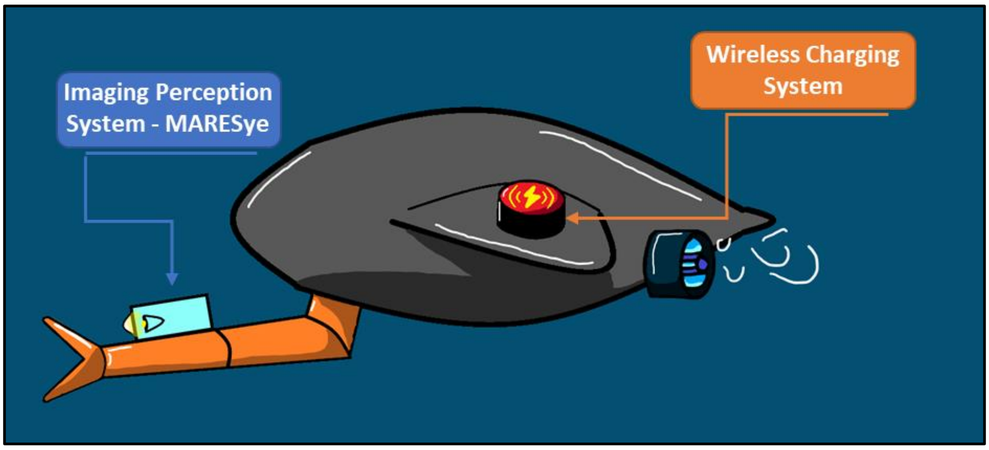

Figure 16. Visual representation of the WCH and IPSH attached to the AUV.

When considering metal components, corrosion is of large concern. Seawater is an aggressive and complex fluid that affects structural materials. In marine environments, there are two processes that operate simultaneous. The formation and repair of passive films on metallic materials due to the presence of dissolved oxygen, and the breakdown of these films due to chloride ion activity. The formation of passive films (oxides, hydrated oxides, or oxyhydroxides) reduces ionic transport of reactive species through the layer. A material ability to resist corrosion depends largely on the passivation film to resist the ionic transport through the layer [114]. Whenever two different types of metal are in contact, they are susceptible to galvanic corrosion when submerged in an aqueous liquid that can ensure the ionic conduction between the metal with the more electronegative potential acting as the anode, and the metal with the more electropositive potential acting as a cathode if the difference in potential is at least 100 mV. The salinity of saltwater further aggravates the intensity of reaction [115].

Another point of concern is that the housings need to be waterproof, as the contact between water and the electronic equipment can cause short-circuits, which may lead to permanent damage and ruin the electric components that can be very expensive to replace/repair.

The two components being designed are intended to achieve different depths. The WCH should be able to go 300 meters deep, while the IPSH only needs reach 150 meters depth

The pressure exerted from the water column (h) is directly proportional to the seawater density (ρ_{sw}), which is about 1025 kg/m^3, and the acceleration of gravity (g) as shown by equation (3).

$$P = \rho_{sw} h g = 1025 \times 300 \times 9.81 = 3.0\ \mathrm{MPa} \tag{3}$$

For 300 meters depth the housings need to endure a pressure of 3.0 MPa, and 1.5 MPa for 150 meters, which is roughly equivalent to 30 and 15 times (respectively) the pressure exerted by air at sea level. The components should not require a lot of effort to be moved vertically underwater. So, a slightly positive to neutral buoyancy is desirable, i.e., the housings need enough weight to barely float.

Since the intended production is of very low volume, the housings will be outsourced to be produced by CNC machining. This process is available for a wide variety of materials and allow for complex geometries, producing parts with high dimensional accuracy. Furthermore, in the case of low volume production, it is one of the faster methods available.

3.3 Product description

3.3.1 Underwater imaging perception system housing

MARESye is a computer vision system technology aimed at gathering 3D object information in very low visibility conditions, due to the underwater environment having high turbidity and high light absorption. This technology uses lasers and a stereo camera system as well as a pair of LED lights, employing light stripe ranging and photometric stereo techniques to achieve a 3D reconstruction (Figure 17) [31]. This component is an integral part for interventive missions.

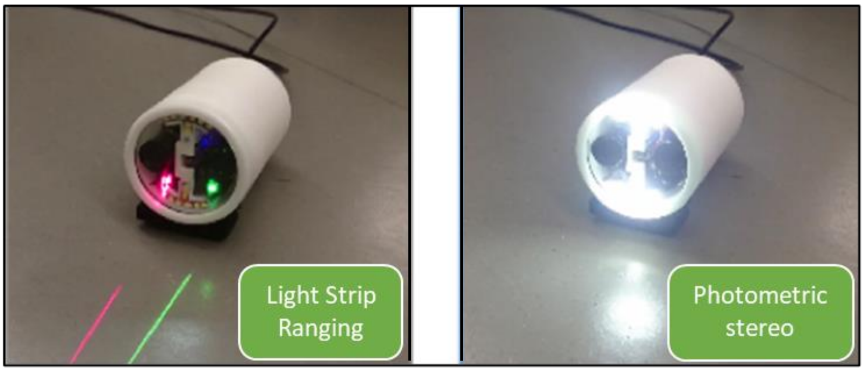

Figure 17. First version of MARESye [31].

The IPSH consists of a box that houses all the electronics and a lid with the appropriate holes, covered with transparent material, which enables the cameras and lasers to visualize their targets. The electronic components are assembled outside the box using 3D printed parts to hold them in place. All access to the housing's interior, such as the lid and box interface or the cable holes, need to be sealed with O-rings, so that the electronic components are protected from contact with water. A set of 2 LED lights are integrated within the housing. Since the LEDs and cameras require calibration, the housing may have to be opened several times, thus an easy to assemble approach is required. Additionally, the design should be compact to prevent interference during future integrations.

3.3.2 Underwater wireless charger housing

The wireless charging system technology serves the purpose of extending the mission life of the AUV. Wireless charging works by transferring energy from a transmitter to a receptor via magnetic induction. The transmitter uses an induction coil to generate an alternating electromagnetic field, the near field power induces voltage/current across the receiver coil [116], which is then used to charge the batteries, allowing the AUV to remain underwater for larger periods of time. This concept is illustrated in Figure 18. The WCH consists of a box housing all the electronic components and a lid that can be attached to another surface, and the interface between the two parts is sealed with an O-ring. This system is composed of two WCHs, the transmitter connected to a docking station, and the receiver connected to the AUV, as shown in Figure 16. The energy transmission is done by contact between the transmitter and receiver boxes bottom walls, where the coils are placed.

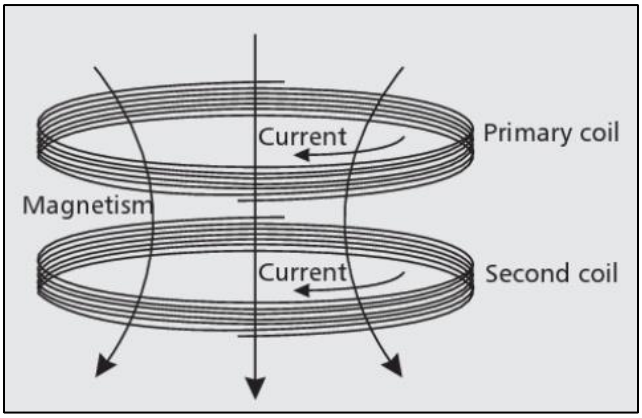

Figure 18. Wireless charging concept [116].

The WCH must accommodate three different wireless systems acquired from Taidacent™, for 12 V, 24 V and 48 V (Figure 19). Table 7 lists the different electrical properties and dimensions provided by the supplier for each of the modules. The goal is to enable interchangeability between modules without changing the WCH in a "one fits all" design. It is also of note that the output current decreases with the distance between coils, so the thickness of the wall of the bottom wall, where the coils are placed, must be carefully considered.

Table 7. Wireless module Taidacent™ specifications

Module	12 V	24 V	48 V
Input voltage	24 V	24 to 32 V	48 V
Output voltage	12 V	24 V	48 V
Output current	3 A	4 A	3~4 A
Output power	36 W	100 W	200 W
Coil inner diameter	30 mm	30 mm	80 mm
Coil outer diameter	82 mm	105 mm	135 mm
Minimum distance between coils	5 mm	7 mm	5 mm

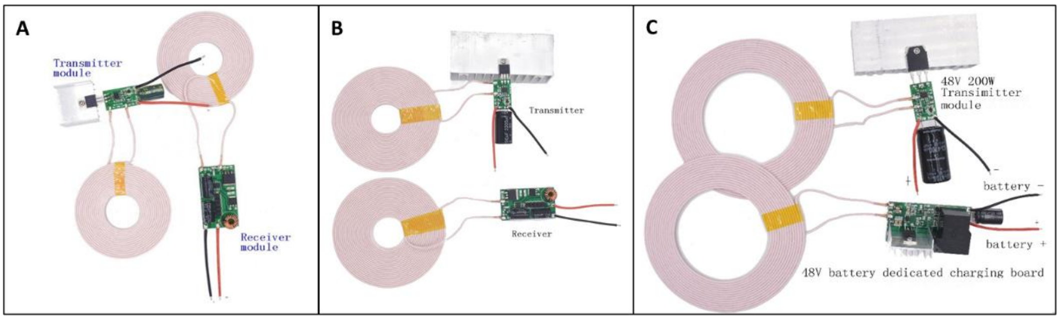

Figure 19. Taidacent™ wireless modules: a) 12 V; b) 24 V; c) 48 V

3.4 Study and critical analysis of existing equipment

The concept of charging AUV batteries via electromagnetic induction has been a target of research in AUV industry. However, there are no commercially available products for this technology yet. That is not the case for imaging perception systems, since both Sexton™ and 2G Robotics™ have several solutions for this technology. Considering the purpose of the proposed housings, a closer analysis to other unrelated pressure vessels can provide a better understanding of the common practices utilized in housing design for pressure forces. For this purpose, Omni subsea™, Nortek™, and BlueRobotics™ products were also analyzed.

Nortek™ DVL500 for 300 meters depth (Figure 20 a) uses POM as its structural material. However, in the 6000 meters version (Figure 20 b) the bottom cylinder is made of titanium while the top part remains POM. This is due to the very high strength of titanium, which makes it a more suitable material for depths that generate hydrostatic pressures of greater magnitude (300 meters – 3,0 MPa and 6000 meters – 60,3 MPa). Sextonco™ GoDeep Stereo (Figure 20 c) uses aluminum for the housing, and acrylic domes for the camera windows. This housing has a depth rate of 500 meters and differs from the other analyzed products because of its shape. The rectangular shape usually allows for a more optimized use of space since most electronic components are not circular, and, by rounding the edges, the structural integrity of the housing is improved. Acrylic domes, besides being more resistant to hydrostatic forces than flat discs, also help retaining the native field of view of the cameras, which is distorted by the refraction of light traversing through three different mediums: water, acrylic, then air, before reaching the lens. Omni subsea™ has two different pressure housing solutions. The 300-meter version (Figure 20 d) is made of aluminum and has ribs along the cylinder. Compared to increasing the wall thickness, this design technique can improve the structural integrity without adding much more material, resulting in a lighter component. The 4000-meter version (Figure 20 e) opts for stainless steel, which is a cheaper alternative to titanium, although, it weighs considerably more (stainless steel is about 2 times denser than titanium, and 3 times denser than aluminum). BlueRobotics™

also has a series of watertight enclosures, (Figure 20 f) made of both aluminum and/or acrylic. Their solutions range between 2 inches and 8 inches of internal diameter. Figure 21 shows a comparison between the inner diameter and the respective depth rating of BlueRobotics™ aluminum end caps of its different series. Since these aluminum end caps share the same thickness (6 mm) and material (AW 6061-T6) between series, changing only in diameter, this figure serves as a good basis to better understand the relation between a flat surface area and pressure induced stress. The analyzed housings share some similarities between them, such as the more common materials, which present excellent corrosion properties and high specific strength.

Figure 20. a) Nortek™ DVL500 – 300 m; b) Nortek™ DVL500 – 6000 m; c) Sextonco™ GoDeep Stereo Aluminum 500 m; d) Omni subsea™ aluminum housing – 300 m; e) Omni subsea™ stainless-steel housing – 4000 m; f) BlueRobotics™ Watertight enclosure series.

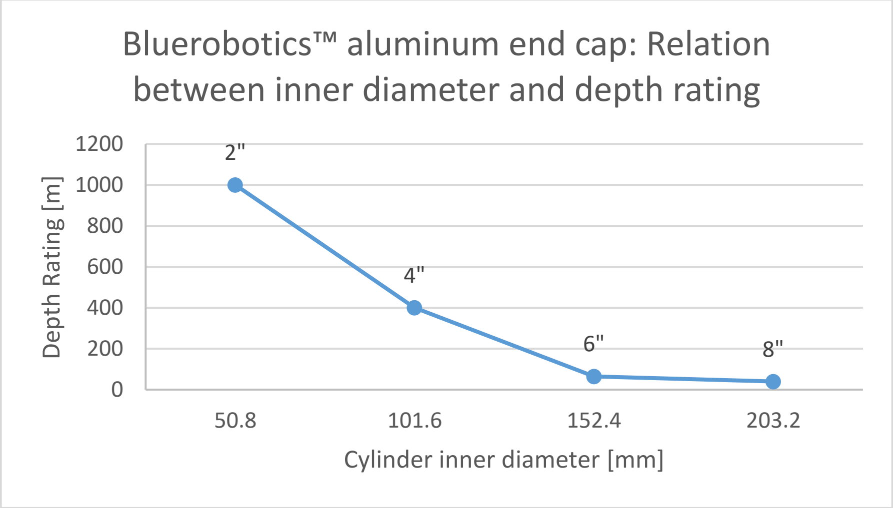

Figure 21. Comparison between the 2”, 4”, 6” and 8” series of BlueRobotics™ aluminum end caps and tested depth rating.

Whenever possible these products have a cylindrical shape, although the space cannot be as well utilized as rectangular shapes, their mechanical performance when submitted to pressure forces, usually determines this shape as the best solution. For this reason, most pressure vessels are cylindrical. However, when a compact design is needed the rectangular shapes can be reinforced by rounding the edges or reinforcing the corners with ribs, thus improving its structural performance.

Both the IPSH and WCH have static seals, either axial or radial (Figure 22), to remain waterproof and most underwater housings use O-rings for this purpose. The rubber O-ring should be considered as an incompressible, viscous fluid having a very high surface tension and, when pressure is applied, the rubber is forced to deform and fill the groove it is in, producing a zero-clearance, blocking the flow of the fluid being sealed. The tendency of elastomers to return to their original shape is the reason O-rings are excellent sealants. Therefore, the compression rate of O-rings is a major consideration when designing with O-rings. In static applications the recommended squeeze is usually between 15-30%. Being incompressible, if elastomeric O-rings overfill the groove they will extrude into the gap or break, so, negative free groove volume must be avoided [117].

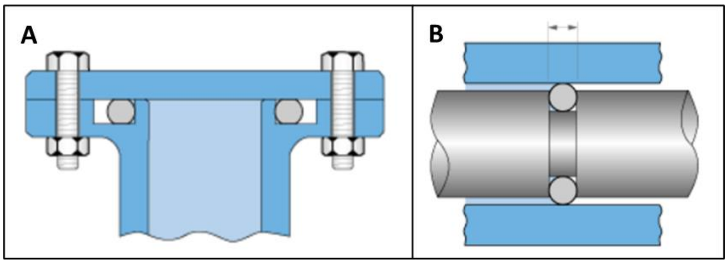

Figure 22. Schematic representation of static seals: a) Axial, b) radial [117]

3.5 Methodology

The methodology used to design both housings follows a 6 steps cycle, described in Figure 23. The process begins with the product concept and definition of its key features and principal requisites. Moving on to the design phase, the product CAD is developed accounting for key features and fabrication process, and, after achieving a satisfactory design that can fulfill those requirements, the project advances to the FEA stage. In this stage, stresses and strains are calculated to determine if the design is structurally reliable. If the results are acceptable, the project can advance to its production phase. If this is not the case, the process should go back to the design phase to be improved upon. After the production phase, which will be outsourced, the products will be tested at the desired pressure in a hyperbaric chamber to verify its structural integrity and waterproofness.

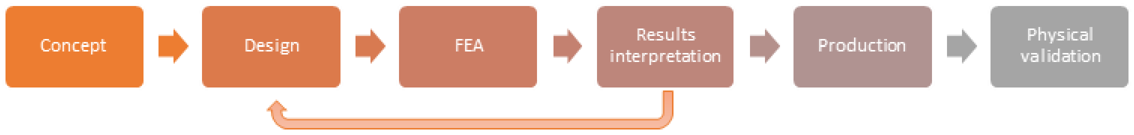

Figure 23. Approached methodology for the design of the IPSH and the WCH

The concretization of the housings follows a design for excellence and modular design approach.

The design for excellence approach focuses on improving certain aspects of the design. This methodology allows for clearer and better-defined goals, that the design should meet, leading to better communication and decision making. This approach is to be defined by visual scorecards similar to those presented in reference [92], where both effectiveness and efficiency metrics are used to determine the success of the design. Effectiveness determines the distance to the design variable target, while efficiency determines how much the variable is exceeded, thus generating waste. A practical example of this concept can be given by the desired factor of safety (FOS) of the housings. By determining a goal of 1.5 for the FOS, a 1.3 value provides an 87% (1.3/1.5) effectiveness, and, since it has not achieved its goal, efficiency cannot be measured since there is no waste. However, assuming the FOS is 1.6, then the effectiveness is 100% since the goal has been met, and since it is generating waste by surpassing the 1.5 value, then its efficiency is 94% (1.5/1.6). Figure 24 represents the scorecard visual representation.

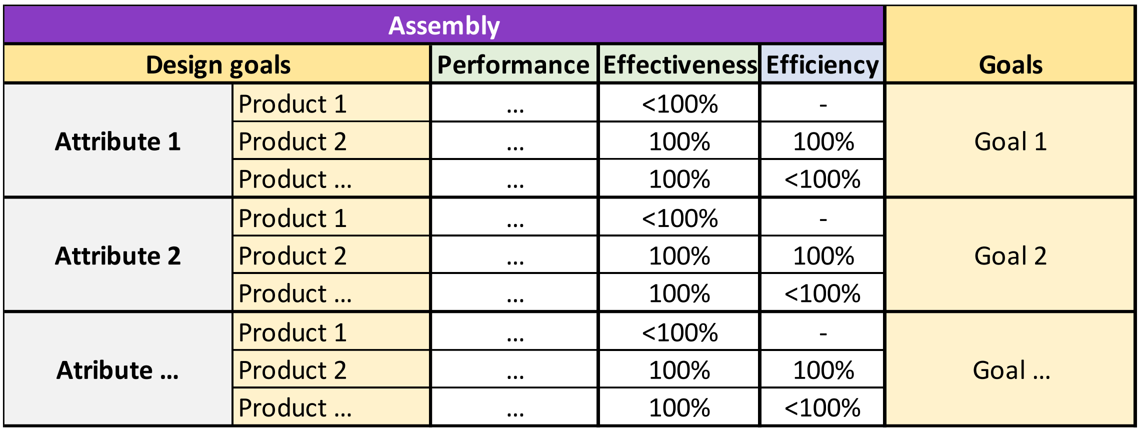

Assembly					**Goals**
Design goals		**Performance**	**Effectiveness**	**Efficiency**	
Attribute 1	Product 1	...	<100%	-	Goal 1
	Product 2	...	100%	100%	
	Product ...	...	100%	<100%	
Attribute 2	Product 1	...	<100%	-	Goal 2
	Product 2	...	100%	100%	
	Product ...	...	100%	<100%	
Atribute ...	Product 1	...	<100%	-	Goal ...
	Product 2	...	100%	100%	
	Product ...	...	100%	<100%	

Figure 24. Design visual scorecard representation example

Due to the nature of the institution INESC TEC, the housings are intended to be used in further research work and, as such, they are not intended for commercial availability. These products should be as adaptable as possible, so they can be easily installed as a complement to any AUV, hence why modularity is heavily desired. This calls for easy to repair/substitute design choices, using as many standardized elements as possible, such as fasteners and O-rings. One aspect of modular design being applied in the WCH is the ability to alter between coils and have a reliable and efficient energy transmission for 36, 100, and 200 Watt capacity. This allows one housing to be able to adapt to the preferred energy potency. Another example for the IPSH housing is the adaptability when positioning the light sources, as well as different ways to connect the camara to whatever surface or object it needs to. When designing with modularity in mind, it allows for one product to be as flexible as possible, which is a valuable feature for the nature of work these housings are destined to.

3.6 Pre-design

The main concepts for the housings are discussed in this stage. The geometrical layout and key components are identified, as well as how those key components are connected and general O-ring placements.

3.6.1.1 Underwater imaging perception system housing

The initial concept for the second version of the MARESye (Figure 25) was already under development before this thesis, although this IPSH design could not meet the 150-meter depth rating. The IPSH assembly consists of a box housing all the electronic components and a lid with a flange, where a set of two custom O-rings fit to ensure that the components in the interior do not come into contact with water. This design would also have the LED lights connected to the outside through 3D printed polylactic acid (PLA) parts. Through this initial concept, some initial constraints are imposed on the future design of the IPSH, such as the box interior dimensions, since the custom O-ring had been already manufactured and the electronic components placement was already defined.

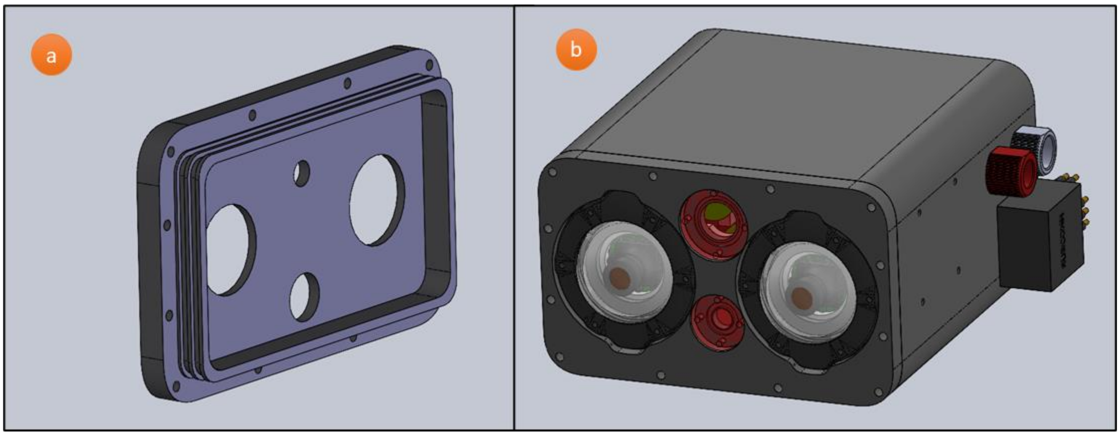

Figure 25. Initial design for the second version of the MARESye; a: Lid backside, b: IPSH full assembly.

This design suffers from very large flat surfaces, mainly at the top and bottom, which would require very thick walls to be able to withstand the pressure at 150 meters underwater. Despite being very compact, this concept is too heavy and cannot withstand the pressure at 150 m depth. That, in the end, would compromise the performance of the manipulator.

Initially, some sketches were made to ascertain which direction should the IPSH design take (Figure 26). At first, the possibility of integrating the LED lights directly into the housing design was considered. However, this approach quickly proved to be inefficient, since it meant less modularity and possible configurations, as well as an even more complicated milling shape, thus this idea was abandoned.

As seen in Figure 26 a, the idea to improve the structural resistance of the housing was to make the top and bottom walls of the IPSH curved. This concept evolved into Figure 26 b, with the walls curved and hollowed. These features will give the IPSH better structural resistance as well as a bigger volume, to improve its buoyancy, and still allow the use of the same flange O-ring. The box corners are reinforced with extra material, due to the abrupt change in geometry, which makes it likely to have high stresses.

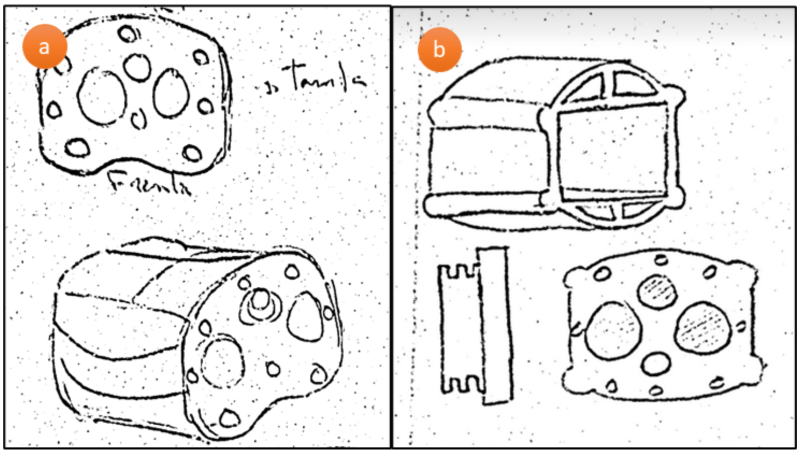

Figure 26. Concept sketches of the IPSH; a: First concept sketch of the curved walls, b: Final concept sketch design.

3.6.1.2 Underwater wireless charger housing

As mentioned in section 3.3.2, the WCH consists of two main parts, a box, and a lid. These two components are fastened with standard ISO bolts, with a standard axial O-ring sealing the interface between them, making it easier to maintain or replace parts, as well as changing between the different coils. The coil axisymmetric geometry allows for a cylindrical housing without wasting too much space. This geometry choice also provides better resistance to the imposed pressure. The electromagnetic current transfer occurs by joining both bottom walls of the transmitter and receiver boxes, this allows the transmitting coil to transfer current to the receiving coil (Figure 18). The 24 V and 48 V coils have large aluminum dissipators. These large dissipators can be replaced by making the lid act as the dissipator instead, allowing for boxes of smaller dimensions, therefore reducing volume and weight. Using structural ribs in the lid enable higher strength and weight ratio optimization. This technique also augments the surface area improving heat dissipation. A power cable of two conductors passes through the lid through a BlueRobotics™ penetrator filled with epoxy. The coils' inner hole allow for a supporting pillar, improving the structural resistance at the middle of the flat surfaces, where the stress is critical, which in turn allow for thinner bottom walls. The concepts and features mentioned are illustrated in Figure 27.

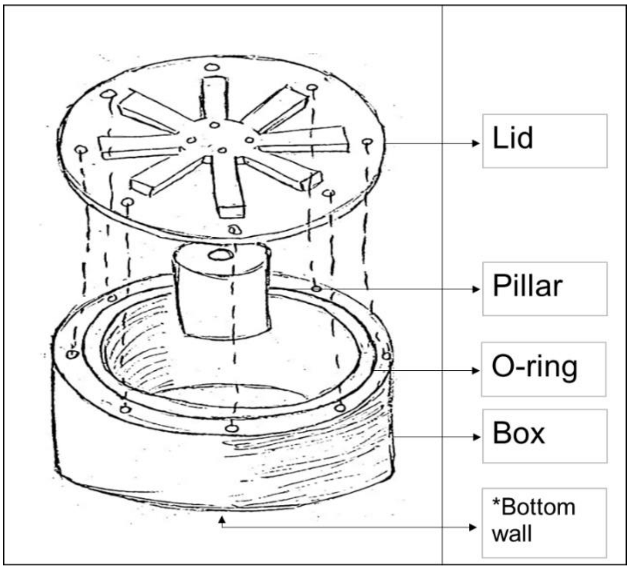

Figure 27. Concept sketch of the WCH design.

3.7 Material selection

The material selection process is a fundamental part of product design/development. An adequate choice of material can greatly improve the efficiency and performance of a product for minimum cost [63]. Underwater environments present extreme and harsh conditions that make mechanical design more challenging [4], so materials need to be researched to ensure they can thrive in these environments while being able to perform their functions. For this work, the Ashby material selection method [63] is adopted to aid the selection process. The next two chapters address the process for each of the housings, following the 4 steps of the Ashby selection method. Firstly, the initial constraints and requirements of the product are clearly defined. Secondly, different available materials are screened, identifying which ones can properly meet the necessary requirements and eliminating those that do not. The few selected materials are then ranked by measuring their performance in the required properties against each other. The raking is done by attributing each property a weight relative to their importance to the design following the process described in section 2.2.2.

3.7.1 Underwater imaging perception system housing

This section is dedicated to the material selection process of the IPSH.

3.7.1.1 Key attributes for the imaging perception system housing

Material strength indicates the ability of the material to resist to an applied load. Strength is usually characterized by the yield stress, where the material starts deforming permanently, although this varies with the nature of the material. In fact, the strength of brittle materials is usually characterized by their ultimate strength since they fracture with little to no plastic deformation. For materials subjected to cyclic loads, the criteria is fatigue strength. The IPSH needs to withstand considerable pressures at 150 m depth, and its square shape makes it less efficient at withstanding those pressures, so a strong material is required. However, since its purpose is to be attached to a manipulator, a neutral buoyancy is desired, to not hinder the arm movements. This feature calls for the use of least mass for the most structural performance. Thus, it is sensible to rank the materials by specific strength, σ_f/ρ, where σ_f is the stress point that indicates failure of the material, and ρ is the material density.

The housing also serves as heat sink for the enclosed electronic components, allowing heat generated from said components to be transferred to the surrounding fluid. The material ability to conduct heat is measured by its thermal conductivity, which represents the power (Watt) conducted per meter thickness of the material, per degree of temperature difference between one side and the other. So, the higher the thermal conductivity of a material the better it performs as a heat sink.

Since the IPSH needs to remain underwater for large periods of time, corrosion caused by the marine environment needs to be considered. The optimum choice of materials and corrosion control measures will prolong structural life. As such, the IPSH material must have good to excellent corrosion resistance. And, if the material performs lower than intended, it needs to be able to go through an adequate process to improve its corrosion resistance (i.e., anodizing) to an acceptable degree.

Stiffness is also a desirable trait for the IPSH since it dictates the rate of the deformation as stress increases. Although high deformations are undesirable it is not a critical aspect of the design.

From the available material families, metals make the most sense considering the desired properties, and fabrication process. Ceramics and glasses usually possess excellent corrosion resistance and high strength. Furthermore, some ceramics also possess very high thermal conductivity. However, they are usually heavy, brittle and hard to mill [118]. Most available engineering plastics are very poor thermal conductors making them unfit for the IPSH as well. Due to its cost effectiveness and reliability, metals are generally preferred over composite materials.

Considering the aforementioned attributes, research was conducted on several materials with potential for the IPSH. All selected metals are present in Table 8. These metals were preferred due to their common application in underwater environments.

Table 8. Screened metals for the material selection process of the IPSH

Aluminum alloys	The more common alloys are the AW 6061-T6, AW 6082-T6 and the AW 7075-T6. These three were considered for the selection process, along with AW 7068-T6 the strongest aluminum available. The attractiveness of aluminum is related to its low density concurrently with high strength. Aluminum alloys also possess high thermal conductivity, decent to good corrosion resistance and are recyclable. The aluminum resistance to corrosion is due to an aluminum oxide film that forms on its surface [119]. Overall, the 6000 series outperforms the 7000 series when it comes to corrosion resistance, while the 7000 series generally have higher strength.
Stainless steel	To make steel corrosion resistant, carbon content in the material must be low, and the addition of chromium in the alloy forms a passive film that protects the underlying material from corrosion. The more common stainless steel is the AISI 316L, where the "L" stands for low carbon, which is also the only one selected. Stainless steels outperform aluminum alloys in their ability to resist corrosion and are relatively stronger than most aluminum alloys. However, they are three times denser and, when compared to the more common aluminum alloys, they are more expensive [120].
Titanium alloys	In the marine industry, titanium alloys can be very valuable due to their very high strength-to-weight ratio, and excellent resistance to corrosion and erosion [121]. The most used titanium alloy, Ti–6Al–4V, is one of the selected materials. Despite its remarkable mechanical properties and corrosion resistance, it is also the most expensive material considered.
Aluminum bronzes	Copper-based alloys in which aluminum is the main alloying element. Aluminum bronzes offer good mechanical properties paired with corrosion resistance. Consequently, they have been very common over the decades in marine applications, such as ship propellers, especially nickel–aluminum bronzes like the UNS C63000 (CuAl10Fe5Ni5). Its corrosion resistance is attributed to a protective film of aluminum and copper oxides [122].

3.7.1.2 Material ranking for the imaging perception system housing

To rank the materials, the attribute's importance and weight must be assigned relatively to their importance towards a successful design. To do this, all properties are assigned a percentual value, out of a hundred, against one of the properties, working as the reference. The sum of this percentage is equal to 100%. For example, the specific strength is considered the most valuable property along with cost and corrosion resistance. Thus, when averaged against stiffness, specific strength is valued at 70% while stiffness is at 20%, indicating that the specific strength is 1,5 times more valuable than stiffness. The reference property is then assigned a weight (w_i^*) of 1, and other properties are attributed a w_i^* by dividing its percentual performance over the reference performance. For example, the w_i^* of thermal conductivity, 0,429, is determined by dividing 70 over 30. The w_i^*, is then normalized (w_i) on a scale of 0 to 1 using equation (4). The results are displayed in Table 9.

$$w_i = \frac{w_i^*}{\sum w_i^*} \tag{4}$$

Table 9. Properties index weight attribution for the IPSH.

Index attribution	**1 - 2**	**1 - 3**	**1 - 4**	**1 - 5**	w_i^*	w_i
Properties						
Specific strength	50	50	70	80	1.000	0.272
Corrosion resistance	50				1.000	0.272
Cost		50			1.000	0.272
Thermal conductivity			30		0.429	0.117
Stiffness				20	0.250	0.068
				∑	3.679	1.000

Table 10 cells are divided according to Figure 28. In the “A” slot are the properties of the selected materials, which were obtained via the MatWeb [123] and Makeitfrom [124] websites. The “B” slot uses equation (1) when maximization is desired (↑), and equation (2) when minimization is desired (↓), to determine the material index (M_i). In the “C” slot is the weighted index (W_i), determined by multiplying w_i with the M_i. The values highlighted in green correspond to the best performing property in each column. The sum of W_i determines which material is considered the optimal selection.

Results show that the AW 6061-T6 aluminum alloy is be the best option. Aluminum alloys are very attractive due to their low density combined with decent mechanical properties. Although the 6061 alloy is the weakest of the aluminums ranked, it is also the cheapest together with the AW 6082-T6. Besides, being categorized in the 6000 series, it possesses very good corrosion resistance, which can be further improved by anodizing. This specific alloy is also one of the standards in marine applications, justifying its suitability for the desired application. However, the aluminum market has been heavily affected by the pandemic, and so it was not possible to obtain AW 6061-T6, despite being a very common alloy. This problem only came to light after the design was concluded, which is why, in section 3.9.1, the material used in the simulation studies is the AW 6061-T6. Instead, the IPSH was manufactured using the AW 6082-T6, which has similar mechanical properties to AW 6061-T6, with slightly less strength, making it a suitable alternative.

Table 10. Material and weighted index for the IPSH

Properties Materials	Specific strength↑ [MPa/(g/cm^3)]		Corrosion resistance↑ [1-5]		Cost ↓ [1-5]		Thermal conductivity↑ [W/m·K]		Stiffness↑ [GPa]		W_i
AW 7068 T6	239.6 1.00	0.272	3.0 0.60	0.163	3.9 0.26	0.070	190.0 1.00	0.117	70.0 0.36	0.025	0.646
AW 6061 T6	101.9 0.43	0.116	4.0 0.80	0.217	1.0 1.00	0.272	167.0 0.88	0.102	70.0 0.36	0.025	0.732
AW 6082 T6	93.3 0.40	0.109	4.0 0.80	0.217	1.0 1.00	0.272	170.0 0.89	0.104	70.0 0.36	0.025	0.727
AW 7075 T6	179.0 0.75	0.203	3.0 0.60	0.163	1.4 0.74	0.200	130.0 0.68	0.080	70.0 0.36	0.025	0.671
AISI 316L	30.0 0.13	0.034	4.0 0.80	0.217	2.4 0.41	0.112	15.0 0.08	0.009	193.0 1.00	0.068	0.440
Ti6 Al-4V	200.2 0.84	0.227	5.0 1.00	0.272	5.0 0.20	0.054	6.7 0.04	0.004	113.8 0.59	0.040	0.598
UNS C63000	62.0 0.26	0.070	4.0 0.80	0.217	3.9 0.25	0.069	37.7 0.20	0.023	115.0 0.60	0.040	0.420

A	C
B	

Figure 28. Table 13 cell Format; A: Property value, B: Material index (M_i), C: Weighted index (W_i)

3.7.2 Underwater wireless charger housing

This section is dedicated to the material selection process of the WCH, which follows the same procedure as the material selection for the IPSH.

3.7.2.1 Key attributes for the wireless charger housing

Stronger materials can withstand higher stresses, and since the box bottom wall thickness determines the energy transmission efficiency, then a strong material is required. Paired with this, the density of the chosen material is of equal importance, since the housing should, ideally, achieve neutral buoyancy, so the AUV moves with greater energy efficiency. For this reason, despite its corrosion resistance to saltwater environments, stainless steel is not commonly used in AUV components, due to its high density. Since both the material strength and weight are of equal importance, materials are ranked by specific strength, similarly to the IPSH material selection.

Ideally, during the charging process, both coils should be concentric and parallel to each other. However, due to the exerted pressure, some deformation is unavoidable. The elastic modulus defines how much a material is deforms as stress increases. Materials with higher elastic modulus require more stress to be deformed. So, to maintain dimensional stability at 300 meters depth, a high stiffness is important to the success of the housing.

Wirelessly charging the AUV occurs while the AUV is stationed at a docking station. When the AUV is docking it will lower itself onto the required position, where the bottom wall of the receiver will contact to the bottom wall of the transmitter. Due to the possible low positional precision of the AUV while docking, it is very possible that impact occurs. This occurrence, combined with the unpredictability of the ocean environment, suggests that toughness is also an important property to consider. While the forces of impact might not be significant, overtime it can generate fractures that can lead to component failure.

The generated electromagnetic field interaction with highly conductive materials results in temperature rise and efficiency deterioration [125], thus, for better energy transfer efficiency, the bottom wall material must have low electrical conductivity. This condition excludes all metals from the material selection process of the box and pillar materials, as metals present high electrical conductivity when compared to the other families of materials.

Also, despite their high strength, environment corrosion resistance, and excellent electrical insulation, both ceramic and glass materials are usually hard to mill, brittle, and heavy [118]. These are not desirable traits for the required application, thus excluding them as well from the selection process, leaving only polymers and fiber reinforced composites as the available options.

Despite generally possessing lower moduli, some polymers can compete with metals when considering their specific strength. This characteristic, added to underwater corrosion resistance, easiness to process complicated shapes and mill, makes them attractive options for the intended purposes of the WCH. For this project, due to their lower cost, polymers are deemed preferable over fiber reinforced composites.

One characteristic of polymers is its capacity to absorb moisture from its environment, affecting dimensional stability when underwater. Therefore, water absorption should be considered during the selection process.

Considering the key attributes, research was conducted to determine which materials presented the better solution, analyzing its general properties, as well as relative costs via the Ensinger™ [126] website. All the selected polymers (Table 11) possess very good chemical resistance and are commonly used in the aerospace, automotive, and food processing industry, in the form of gears, supports, sliding elements, spacers and valve components.

Table 11. Screened polymers for the material selection process of the WCH.

POM	POM, also known as acetal, is a high strength and stiff plastic. It has good wear resistance and low water absorption. These features together with the ease of machinability make POM one of the more used materials in underwater robotics. There are two variants of POM, depending on their polymerization. It can be copolymer, POM-C, or homopolymer, POM-H. The key difference is that the POM-C possesses better chemical resistance and lower melting point, while the POM-H has overall better mechanical properties [127]. However, their performance is not distant from each other, both chemically and mechanically.
PA	Polyamide (PA), or nylon, possesses high strength, stiffness, and good chemical resistance, as well as lower density than POM. Most commercial applications use either PA 6 or PA 66. Their names relate to the crystal structure of the polymer, which influences properties related to temperature, which are not relevant for the needed requirements. However, it also affects mechanical properties, and the PA 66 is both stronger and more rigid than the PA 6 by a small margin [128]. However, the PA 66 is also more expensive.
PEEK	PEEK possesses higher strength and moduli, as well as higher resistance to both chemical and physical degradation than the other selected polymers for the WCH [129]. Despite its excellent chemical and mechanical properties, it is also, by large, the most expensive polymer considered.
PET	Polyester (PET) has a higher glass transition temperature, as well as better mechanical properties than low-cost thermoplastics, such as PA. It can also achieve negative permittivity, favoring its use for wireless power transfer [130].

3.7.2.2 Material ranking for the wireless charger housing

The material ranking for the WCH is the same as the IPSH. Table 12 shows the assigned values of each property and their calculated w_i. Since all the selected polymers present excellent corrosion resistance properties, this attribute is not weighted. The properties of the selected materials in Table 13 where obtained via the Ensinger™ [126] and PolyLanema™ [131] (ANNEXES) websites, the table also shows the calculation of the weighted index that leads to the appropriate material selection following the same process used for Table 10. Since the desired attributes of the WCH lid coincide with the IPSH, the selected material is the same.

Table 12. Properties index weight attribution for the WCH.

Index attribution / Properties	1 - 2	1 - 3	1 - 4	1 - 5	w_i^*	w_i
Specific strength	60	75	50	75	1.000	0.300
Stiffness	40				0.667	0.200
Toughness		25			0.333	0.100
Cost			50		1.000	0.300
Water absorption				25	0.333	0.100
				∑	3.333	1.000

Table 13. Material and weighted index for the WCH.

Properties / Materials	Specific strength ↑ [MPa/(g/cm^3)]		Stiffness ↑ [MPa]		Toughness ↑ [kJ/m^2]		Cost ↓ [1-5]		Water Absorption ↓ [%]		$\sum W_i$
POM - C	47.5	0.161	2600	0.124	8	0.053	1	0.300	0.10		0.678
	0.54		0.62		0.53		1		0.30	0.030	
POM - H	55.2	0.187	3400	0.171	15	0.100	1	0.300	0.10		0.789
	0.62		0.86		1.00		1		0.30	0.030	
PA 6	68.4	0.232	3300	0.138	7	0.047	1	0.300	0.60		0.741
	0.77		0.69		0.47		1		0.05	0.005	
PA 66	73.0	0.247	3500	0.148	5	0.033	2	0.150	0.40		0.605
	0.82		0.74		0.33		0.5		0.08	0.008	
PEEK	88.5	0.300	4200	0.200	4	0.027	4	0.075	0.03		0.702
	1.00		1.00		0.27		0.25		1.00	0.100	
PET	65.5	0.222	3500	0.162	5	0.027	2	0.150	0.03		0.672
	0.74		0.81		0.27		0.5		1.00	0.100	

Results show that POM-H is the optimum choice for the WCH. It presents good mechanical properties, although its specific strength is not one of the highest, due to having higher density than the others. However, this is compensated by its accessible cost, and especially impact resistance, where it outperforms the other plastics by a significant margin. It is also the second most stiff, being surpassed only by PEEK. POM has good machinability [132], a reliable reputation, and it is commonly used in underwater applications, as described in section 3.4.

Unfortunately, the same issue that happened with the IPSH also occurred with the WCH, being that POM-H, a usually easy and common to obtain material was not available, and again, this issue only came to light after there was no time to redesign the components. This means that the replacement material needs to match the mechanical properties of POM-H (ANNEXES) especially yield strength, Young's modulus, and density since one of the main goals is neutral buoyancy. This guarantees that the current design is functional with the substitute material. Only three of the listed materials fulfill those requirements: PA 66, PEEK and PET. Since PEEK is considerably more expensive than the other two options, and PA 66 has a much lower density, which would affect the buoyancy, and higher water absorption than POM-H. PET is the material of choice to substitute the POM-H, since it has similar mechanical properties, excluding toughness which is considerably lower.

3.8 Design

3.8.1 Underwater imaging perception system housing

The IPSH is an AUV component and as such, it is desirable that it can easily integrate in any AUV build. In this section, all design choices as well as the different components and what roles they perform within the assembly are explained and justified.

3.8.1.1 Box

The IPSH box final design is shown in Figure 29. One of the critical aspects analyzed in section 3.4 was the relation between a flat surface are and the hydrostatic pressure it can withstand. One of the main problems with the original design (Figure 25) is that the bottom and top walls have a large flat surface area and, to be able to go 150 meters underwater, it would require a sizable thickness. To overcome this issue, the final design shape has rounded the top and bottom walls (Figure 29 a) and, by hollowing these walls (Figure 29 b), the design is able to successfully withstand the pressure and remove excessive material, thus reducing weight. Another advantage of this feature is the increase of the overall volume, improving the IPSH buoyancy. Due to the more abrupt change in geometry of the box corners, stress concentrations can be expected in those areas. To mitigate this issue, all four corners of the box are reinforced with extra material (Figure 29 c). An undercut at the top and bottom contact zones with the lid (Figure 29 d) helps alleviating stress in those areas since, throughout the several iterations, it was verified that one of the stress critical zones was the center of the top and bottom contact zones with the lid.

The lid is connected to the box with eight M5 fasteners (Figure 29 e). Compared to the initial design, the number of fasteners is reduced from 12, which translates into slightly less weight. The three holes at the right-side wall (Figure 29 f, g and h) are for components that need to be outside the IPSH, namely a BlueRobotics™ vent and penetrator, and a SubConn™ ethernet connector. The vent's purpose is to verify the IPSH sealing, by connecting it to a vacuum pump, if the pressure remains stable overtime. The lights on the exterior need to be connected to the rest of the system in the interior. This is done via the penetrator, through which passes the cable that makes the connection. And lastly, the ethernet connector allows signal and power supply to be connected in one unified solution.

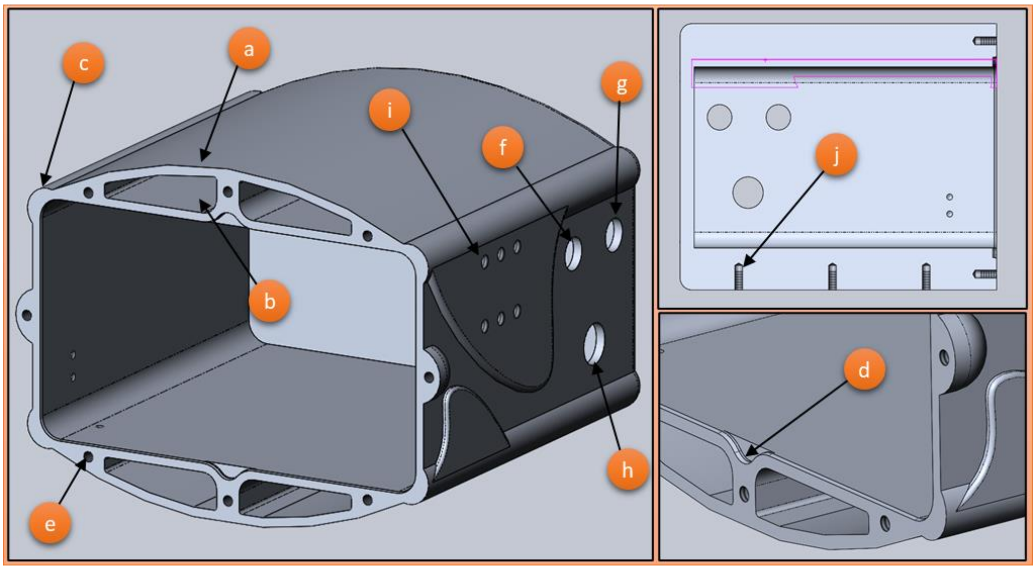

Figure 29. IPSH box final design; a: Curved form, b: 4× Hollowed space, c: Corner reinforcement, d: Contact undercut, e: Lid connection (8× M4 tapped hole), f: Vent hole, g: Penetrator hole, h: Ethernet hole, i: Light system connection (6×M5 tapped hole), j: Outside connection (3×M5 tapped hole).

At the time of developing the IPSH the light system was still an uncertainty. Six M5 tapped holes were added to the side walls, to enable some flexibility as to how the system would be attached to the box (Figure 29 i). The thickness of the side walls (3 mm) did not allow to reliably drill a tapped M5 hole, thus material was added in an ocean wave form to keep the box aesthetically coherent with its application. The IPSH is intended to be used alongside a manipulator and, as such, a way to connect this housing to an exterior component is needed. This connection is done through a set of three M4 tapped holes (Figure 29 j) along the center of the bottom wall.

3.8.1.2 Lid

The IPSH final design is shown in Figure 30. The principle of the MARESye technology described in section 3.3.1 requires the use of multiple lasers and two cameras, all aiming at the same target. The holes inside the pockets on the lid (Figure 30 a, b, and c) align with these components and, around each hole, there is an O-ring groove. The O-ring is then compressed against transparent acrylic components, thus waterproofing these zones while letting light reach the target. The connection between these acrylic components and the pockets is done through twenty M2 fasteners. The lid has eight M4 clearance holes (Figure 30 d) that match the M4 tapped holes (Figure 29 e) in the box.

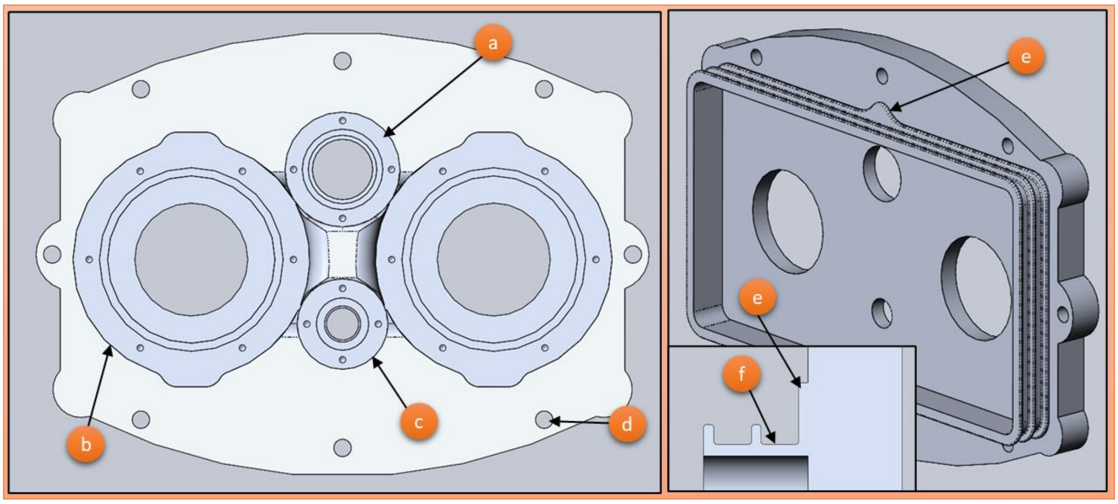

Figure 30. IPSH lid final design; a: Top lasers pocket, b: 2×Camera pocket, c: Bottom lasers pocket, d: Box connection (4×M5 clearance holes), e: Contact boss, f: Flange O-ring groove.

To ensure that no water enters the interior of the box, the lid has a flange with two bosses at the top and bottom (Figure 30 e) matching the contact undercuts of the box (Figure 29 d). This flange also has two O-ring grooves (Figure 30 f) for the two custom O-rings that get compressed against the box interior walls.

3.8.1.3 Light system

The light system is designed as seen in Figure 31, consisting of two 3D printed PLA components where the BlueRobotics™ lights (Figure 31 a) are attached. This system is designed to fit in the sets of six M5 tapped holes on side walls of the box (Figure 29 i). One of the two components is the light holder (Figure 31 b). This component is designed to take advantage of the PLA ability to achieve considerable deformations while maintaining a linear elastic behavior. The other component is the light positioner (Figure 31 c). Its main function is to support and guide the angle adjustment system (Figure 31 d). This system works by increasing or decreasing the gap between the light holder and the positioner, thus adjusting the angle of the lights. The light holder has a large, curved bend, which works as a spring, in the sense that in can achieve high deformations through the clamping force of the angle adjustment system, and then return to its original shape when this force is removed.

The lights are connected to the system on the interior via a cable that passes through the penetrators in the lights (Figure 31 e) and the penetrator at the side of the box (Figure 29 g). These penetrators are filled with epoxy around the hole the cable is inserted, thus preventing water from getting in through this hole.

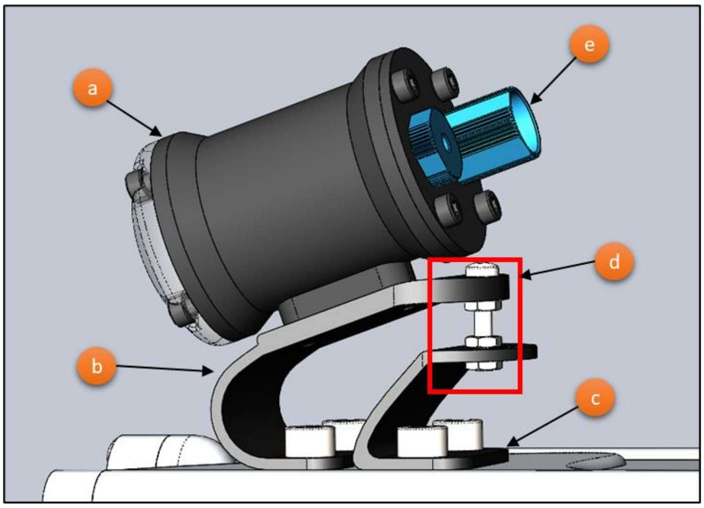

Figure 31. Light system final design; a: BlueRobotics™ Lumen light, b: Light holder, c: Light positioner, d: Angle adjustment system, e: Penetrator.

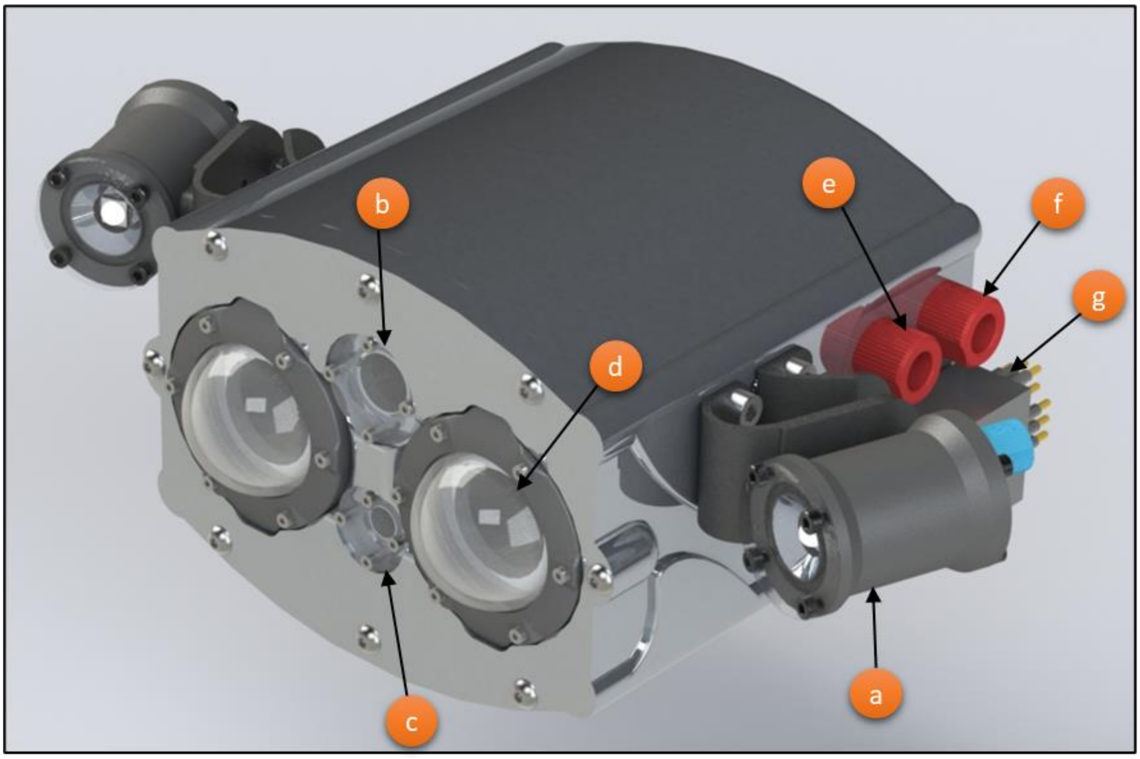

Figure 32. Rendered design IPSH final exterior build; a: Light system, b: Top lasers pocket acrylic, c: Bottom laser pocket acrylic, d: Camera pocket BlueRobotics™ acrylic dome, e: BlueRobotics™ vent, f: BlueRobotics™ penetrator, g: SubConn™ ethernet connector.

All the exterior components that incorporate the full build of the IPSH are visible in Figure 32, including the light system (Figure 32 a) described above. The acrylics that fit the top lasers (Figure 32 b) and bottom laser pockets (Figure 32 c) are manufactured at the INESC TEC laboratories, via CNC milling. For the cameras, using hemispherical acrylic pieces helps reducing the refractive effects of the light while traversing through different mediums, leading to less effort calibrating the projection center of the cameras. These dome ports (Figure 32 d) are from BlueRobotics™, which are acquired with an acrylic dome, and an aluminum support to keep the dome in place, which is fastened to the lid. Both the vent (Figure 32 e) and the penetrator (Figure 32 f) are also acquired from BlueRobotics™, and the ethernet connector is acquired from SubConn™. These three components are threaded and fixed to the box by a nut at the box interior. These components also have an O-ring groove and an O-ring at the underside that gets pressed against the box wall, ensuring that no water can get through the holes.

3.8.1.4 Imaging perception system assembly

A step-by-step guide of the IPSH assembly is described in Table 14. It is important to note that the purpose of this thesis does not include the design of the electronic system; thus, the assembly of this system is omitted from Table 14. Instead, the interior of the MARESye is considered as a single element. While assembling the components, it is important to carefully examine each O-ring to make sure it is not damaged and undertake proper lubrication with silicone grease to prevent damages.

Table 14. Step by step assembly of the IPSH

Step 1: The O-rings must be placed in their respective grooves at the light penetrator, vent, and ethernet connector which are assembled to the box with a nut at the interior.	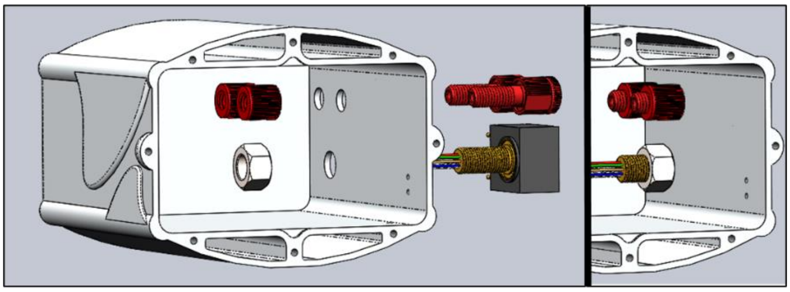 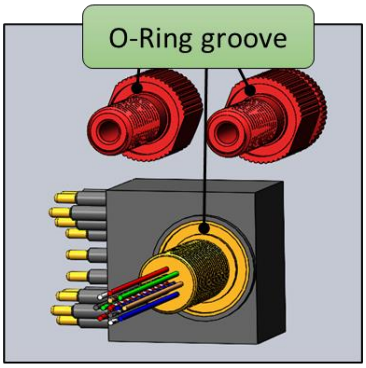

Step 2: The light system is assembled to the sides of the box.

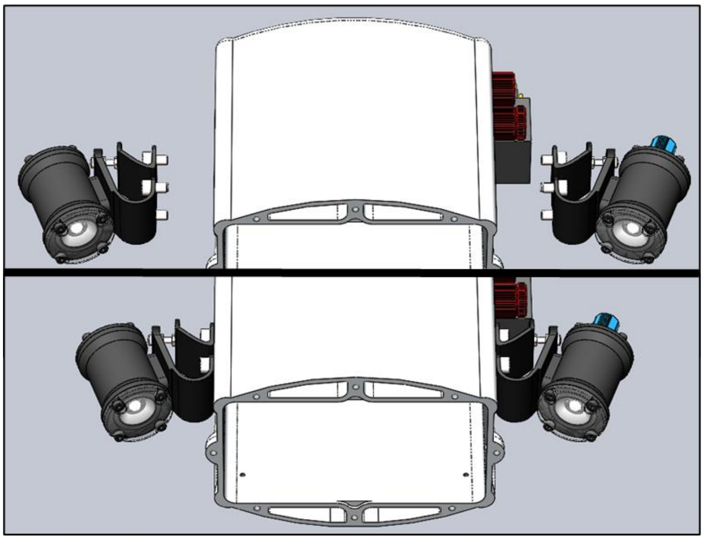

Step 3: The electronic system is assembled before going inside the box. After the system is fully connected, then the electronic system is inserted inside the box.

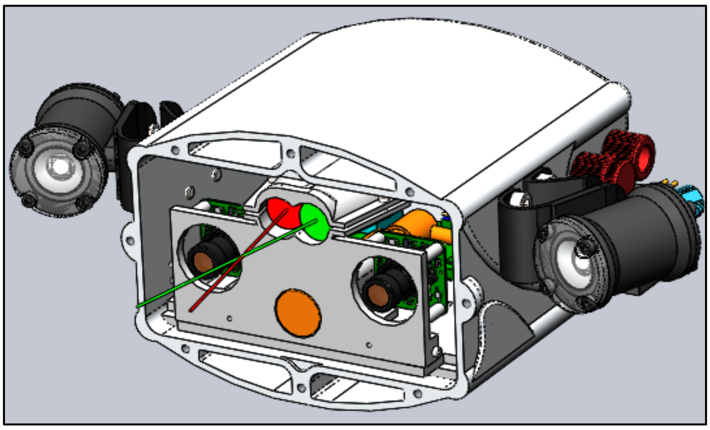

Step 4: Before assembling the lid, the O-rings must be placed at the flange grooves. Then the lid is carefully inserted and fastened to the box.

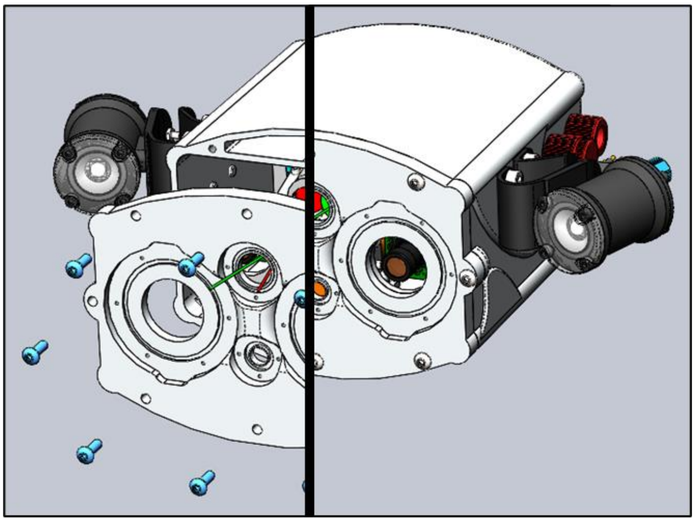

Step 5: The pocket O-rings are inserted into the grooves before the acrylic components are fastened to the lid.

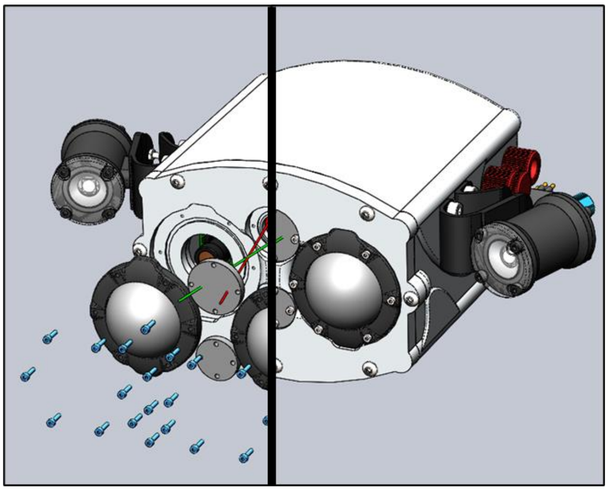

To verify the buoyancy, all component weights need to be quantified. The electronic components, light system printed parts, acrylics, penetrator, vent, and ethernet connector were weighted on a scale (± 0.5 g). Some of these components were weighted together, while the box and lid weights were obtained from the evaluate tool "mass properties" from SolidWorks™. These weights will then be used to obtain the underwater apparent weight.

The weight of these sets of components as well as the full assembly are listed in Table 15. The BlueRobotics™ Lumen lights weight is not accounted for, as the underwater apparent weight is already provided by the supplier (53 g).

Table 15. IPSH components weight and buoyancy analysis

Imaging perception system housing	
Component	**Weight [g]**
Interior electronic components	635
Light system – printed parts and fasteners only	20
Lid components – acrylics, domes, and fasteners	33
Ethernet, penetrator, and vent	231
Lid	275
Box	1088
∑ (full assembly without Lumen lights)	2282

The exterior volume of the IPSH is obtained via the "mass properties" tool of SolidWorks™, with a 3D model imitating the exterior aspect of the IPSH assembly, as shown in Figure 33. The density of the IPSH is obtained by dividing its total weight with the exterior volume and is then compared to ρ_{sw}. Equation (5) is used to obtain the underwater apparent weight, where $Mass_{total}$ is the total mass of the assembly, and

$Volume_{total}$ is the total volume of the same assembly. The light's underwater apparent weight is then added to the total.

$$Underwater\ apparent\ weight = Mass_{total} - \rho_{sw} \times Volume_{total} \tag{5}$$

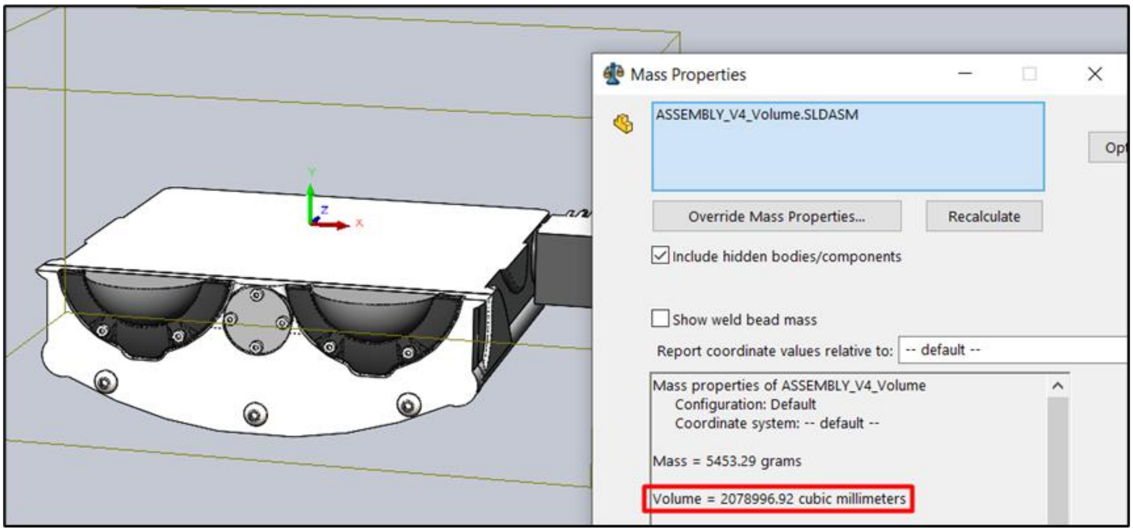

ASSEMBLY_V4_Volume.SLDASM

☑ Include hidden bodies/components

☐ Show weld bead mass

Report coordinate values relative to: -- default --

```
Mass properties of ASSEMBLY_V4_Volume
    Configuration: Default
    Coordinate system: -- default --

Mass = 5453.29 grams

Volume = 2078996.92 cubic millimeters
```

Figure 33. Solid body used to measure the exterior volume of the IPSH.

With a total volume of 2078.99 cm^3 and a total mass of 2223.79 g:

Density [g/cm^3]: 1.098

Underwater apparent weight without the Lumen lights [g]: 151.0

Underwater apparent weight with the Lumen lights [g]: 151.0 + 2 × 53 = 257.0

Ideally, the underwater apparent weight should be negative, meaning the IPSH floats. However, to increase the buoyancy of the IPSH the volume would need to increase as well, which means less compactness. The trade-off between compactness and underwater apparent weight is one of the more challenging aspects of this design process. Despite the IPSH sinking, the achieved performance is still a considerable upgrade over the previous version. This final design weights about the same as the initial concept in Figure 25. However, with better buoyancy, due to the increase in volume, and much better structural strength.

Further tests were made with the physical prototype fully assembled. The underwater apparent weight was measured with a dynamometer at the FEUP CRAS center pool (Figure 34). The MARESye was tied to a string so it would not sink to the bottom. The experimental results obtained (0.260 kg) are very similar to the ones calculated above, thus proving the method used to calculate the underwater apparent weight effective.

Figure 34. Measuring the Underwater apparent weight with a dynamometer – 0,260 kg.

3.8.2 Underwater wireless charger housing

The WCH follows a modular design, varying according to the power required for the mission. In this section, all design choices as well as the different components and what roles they perform within the assembly are explained and justified. It is important to note that the 12 V module shares the same components as the 24 V module, except the electronic components described in section 3.3.2. However, there are significant differences in the 48 V module, namely in the pillars and the electronic casings. For clarity, the names of these components are either followed by 24 V, belonging to the 12 and 24 V module, or 48 V, belonging to the 48 V module. Some components may also have either transmitter or receiver in their name depending on the housing configuration they belong.

3.8.2.1 Box

The WCH box is designed as seen in Figure 35. The curvature that leads from the bottom wall to the side walls (Figure 35 a) has a 12 mm radius and largely reduces any stress concentration that would be present if the corners were sharp edges. With this curvature, stress is significantly lowered, allowing the bottom wall to be thinner, thus improving the inductive transfer efficiency. Consequently, since the coils need to be concentric and parallel to the bottom wall, the WCH has a larger diameter. The flat surface at the bottom has 138 mm diameter, enough to accommodate the largest coil of 135 mm diameter. However, due to the mentioned curvature, this diameter is increased up to 162 mm.

The eight flanges (Figure 35 b), evenly spaced along the circumference, have a tapped M8 hole (Figure 35 d) where fasteners join the lid to the box. The box side wall cannot hold both the fasteners and the O-ring within the top surface area. Since the walls can already withstand the pressure, these flanges add the required area only where it is needed, leading to a lighter box than would occur, for example, by increasing the overall wall thickness.

The box has an O-ring groove visible on the top surface. The selected O-ring has 170 mm inside diameter and 2 mm cross-section diameter. The groove (Figure 35 c) dimensions are 169 mm and 174 mm for the inside and outside diameter, respectively, and a groove height of 1.6 mm, compressing the O-ring cross section by 20% (1.6 is 80% of the 2 mm cross section) when the lid is assembled. To not tear the O-ring, all sharp corners of the groove are filleted with a 0.2 mm radius.

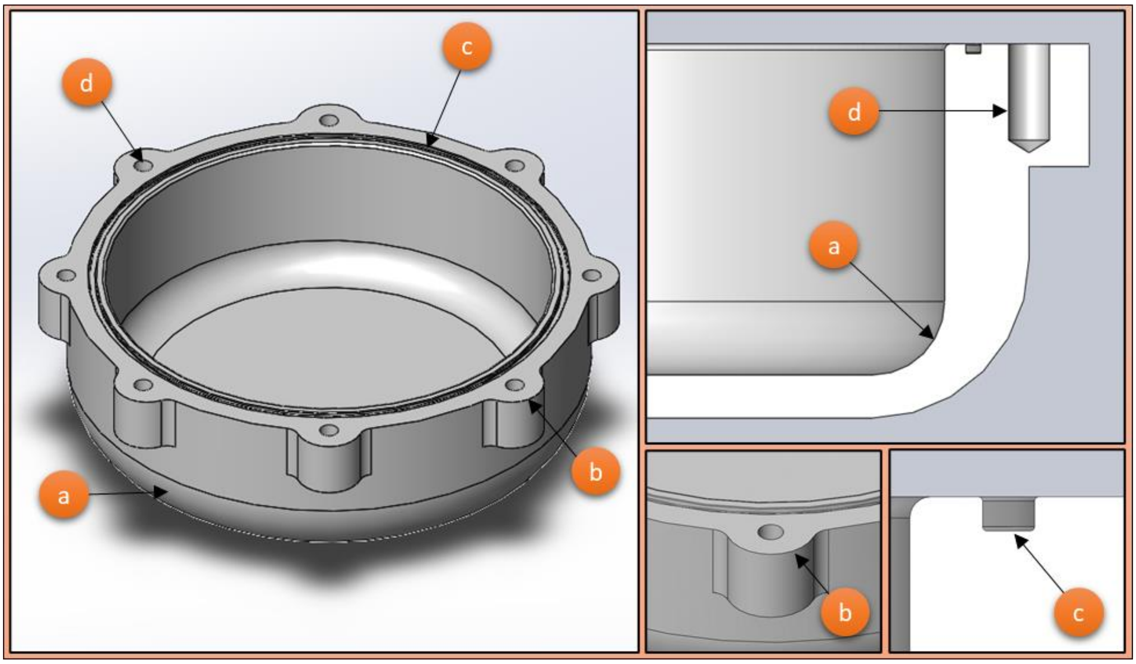

Figure 35. WCH box final design; a: Curved corner, b: 8×flanges, c: O-ring groove, d: Lid connection (8×M8 tapped hole)

3.8.2.2 Lid

The WCH lid is designed as seen in Figure 36. Just like the box, the lid possesses eight flanges (Figure 36 a), with eight 8.5 mm diameter clearance holes instead of tapped holes. The undercuts (Figure 36 b) serve the purpose of removing mass where the stress is less critical. This feature allows the part to be lighter, while maintaining good structural performance. There are eight undercuts in total, with one being different from the rest due to the penetrator hole (Figure 36 c), where the 2-core cable passes through. Besides, there are also 6 tapped M3 holes (Figure 36 d) on the top surface, with an orientation equal to the previous version. These holes serve to connect the wireless to an exterior part (i.e., the AUV) and, by maintaining the same display, it allows for an easier upgrade.

The bottom the lid possesses a small boss (Figure 36 e), which facilitates the flange's alignment between the box and the lid. And, since the pressure exerted on the box causes the walls to deform inwards, there would be a large stress concentration on the connector holes. This ledge impedes the inward deformation of the box, thus alleviating concentrated stresses around the flange's holes.

For the lid to properly function as a heat sink, the metal oxide semiconductor field effect transistor (MOSFET) of the electronic components needs to be touching the aluminum. The 2 tapped M3 holes (Figure 36 f) serve that purpose, one for the 24 V assembly (which can also accommodate the 12 V coils), and one for the 48 V assembly. There is also a tapped M8 hole in the center (Figure 36 g) that enables the connection between the pillars and the lid.

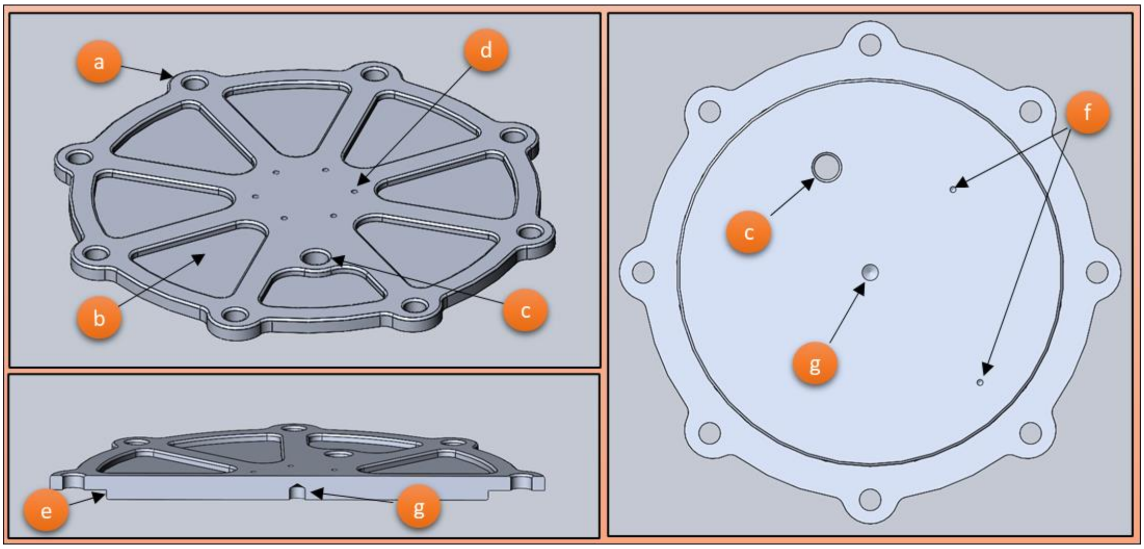

Figure 36. WCH lid final design; a: 8× flange (M8 clearance hole), b: 8× undercuts, c: penetrator hole, d: exterior connection (6×M6 tapped holes), e: bottom boss, f: MOSFET connection (2× M3 tapped holes), g: pillar connection (M8 tapped hole)

3.8.2.3 Pillar for the 24 V assembly

In an initial design phase, the WCH design had only a 28 mm structural pillar to prevent the box from collapsing at its center. This was the maximum allowed diameter since it needed to house all three coils (with an inner diameter of 30 mm for 12 and 24 V and 80 mm for 48 V). However, this solution required a much thicker bottom wall, or a stronger material, such as PEEK, which is much more expensive. This problem surged due to the size of the surface area at the bottom of the box being too large, and therefore having a resulting force that compromised a 28 mm pillar. The solution to this problem is found at designing a specific pillar for each assembly. As such, each pillar is named after its assembly, pillar 24 and pillar 48.

Due to the more limited diameter of pillar 24, an outer ring (Figure 37 a) is added to reduce the stress on the center column (Figure 37 b). The column and the outer ring are connected by two non-structural joists (Figure 37 c) that also help maintaining the 12 and 24 V coils parallel, concentric, and touching the bottom wall. The center column has slightly less height than the outer ring. This 1 mm gap allows the box bottom wall to deform in the shape of the center column, so the stress is more evenly distributed around the circular area instead of concentrating around the edges of the box-pillar interface. The curvatures displayed in both the center column and outer rings (Figure 37 d, highlighted by the red circles) have large radii and are tangent to the flat surface adjacent to them. Further justification for the existence of this curvatures is detailed in section 3.9.2.2.

On the top surface in the center column there is a M8 tapped hole (Figure 37 e) where the pillar is connected to the lid. This connection is made by a threaded M8×20 mm rod, allowing for an easy assembly.

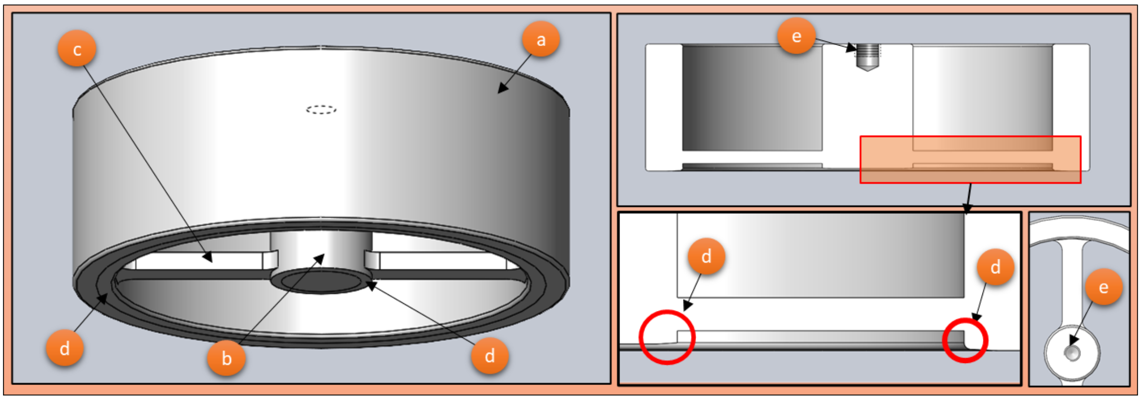

Figure 37. Pillar 24 final design, a: outer ring, b: center column, c: non-structural joist, d: edge curvature, e: lid connection (M8 tapped hole)

3.8.2.4 Pillar for the 48 V assembly

Since the 48 V coil has a larger inner diameter, of 80 mm, the challenges that existed with the pillar 24 do not translate to this assembly. This pillar (Figure 38) consists of a single 78 mm diameter solid column with a 1 mm gap in height between the pillar and the box bottom wall. A revolved cut at the bottom is also present (Figure 38 a), where a 3D printed component is fitted to maintain the coil in place. The bottom edge also has a large radius curvature (Figure 38 b) to prevent stress concentrations around the edge of the pillar, as it shares the same issue as pillar 24. At the top surface of the pillar, there is the same M8 tapped hole (Figure 38 c) found in pillar 24, which enables the connection to the lid.

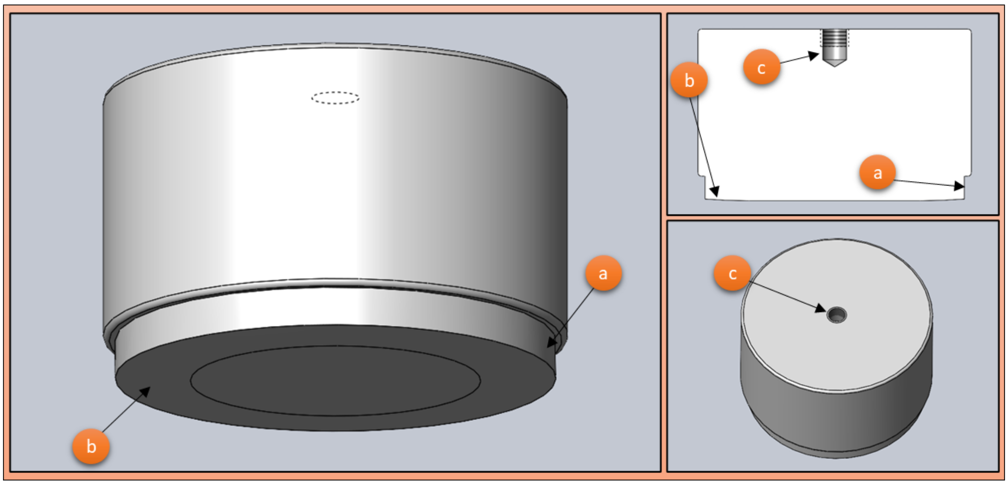

Figure 38. WCH pillar 48 final design, a: revolved cut, b: edge curvature, c: lid connection (M8 tapped hole)

3.8.2.5 Non-structural components

Non-structural components refer to components that do not perform any structural task. Therefore, these parts are not subjected to any stresses. Due to this factor, these components are 3D printed with PLA filament, which reduce the costs of the fabrication process of these models, since a 3D printer is available at the CRAS center.

To facilitate the WCH assembly, separate casings (Figure 39) were created to lodge the electronic parts inside, while only allowing the MOSFET to be connected to the aluminum lid, serving as a heat sink, and separate the conductive tracks of the printed circuit board (PCB) with the aluminum, since it may cause a short circuit. For the 12 V and 24 V coils, the electronic casings are the same, since the pillar is shared between the modules, and the electronic components of the 12 V version are similar, albeit smaller than the 24 V coil. The 48 V electronic casings are larger, both for the transmitter and the receiver. However, due to the disposition of the MOSFET in the 48 V receiver coil, it cannot be connected reliably to the aluminum lid, and since the original heat sinker is not as large as the transmitter’s, it is not removed. These casings consist of two parts, a box, and a lid, connected by 3 M2 bolts. These models were then 3D printed and assembled with the electronic components as seen in Figure 40.

Another component is the 48 V coil holder. This component is inserted in the pillar 48 revolved cut with the purpose of holding the 48 V coil parallel, concentric, and touching the bottom wall.

The purpose of these components is to facilitate the assembly process, which enables faster and easier repair in case some of the components fail, as well as facilitating the interchangeability between the modules. They also hold all the electronics in a confined space, enabling the MOSFETs to transfer heat through the lid, and avoid contact between components that could lead to short circuiting the system.

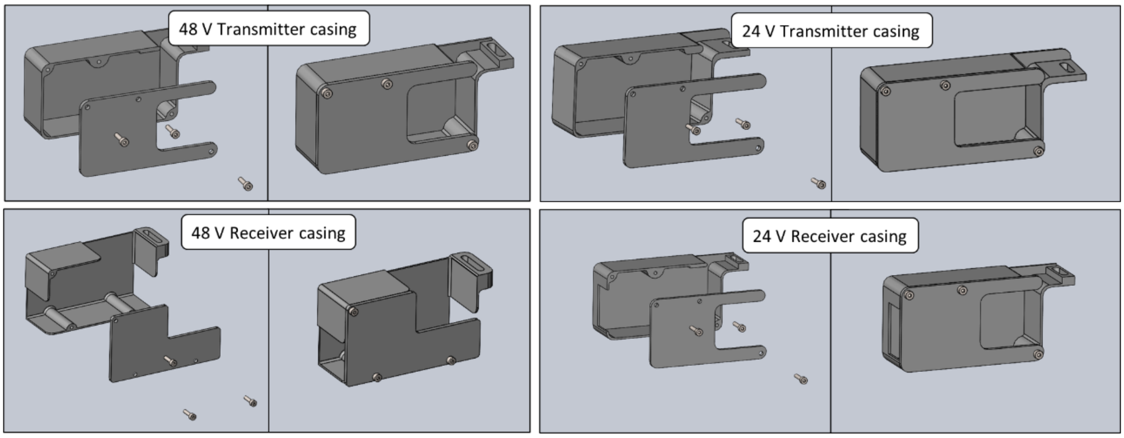

Figure 39. Electronic components casings final design for the WCH

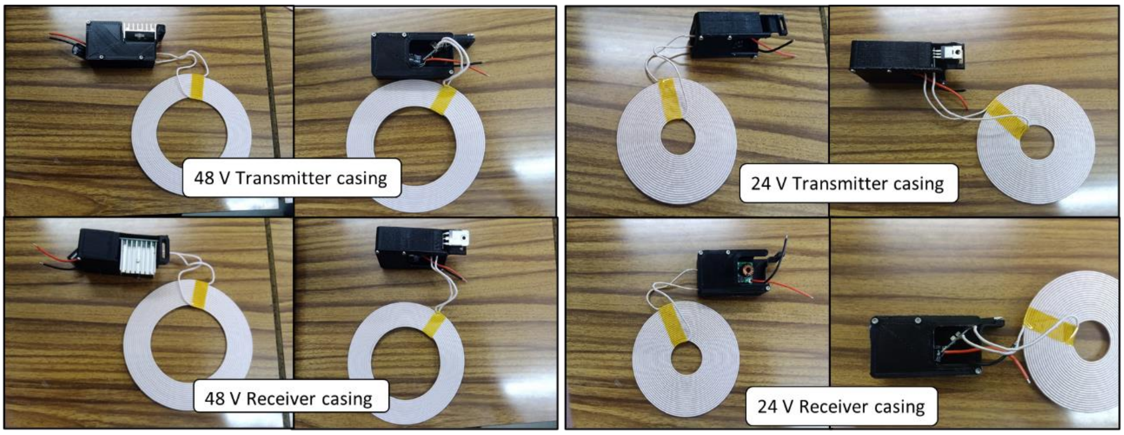

Figure 40. 3D printed electronic components casings.

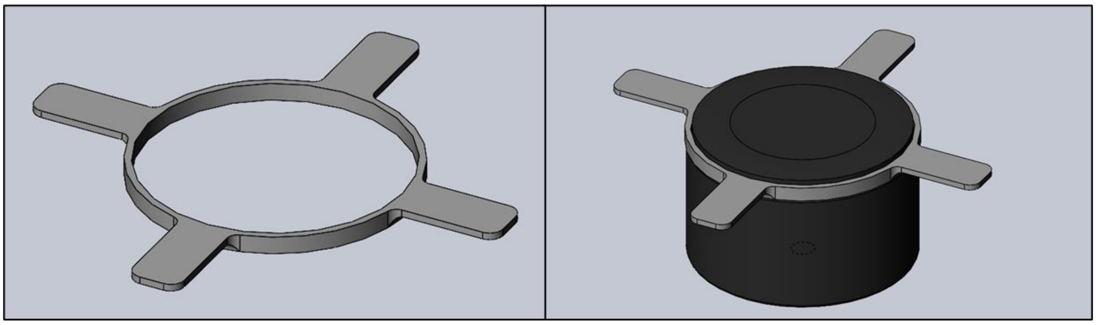

Figure 41. WCH 48 V coil holder final design

3.8.2.6 *Wireless charger housing assembly*

Table 16 details the assembly process of the WCHs, including a brief description of each step in the left column aided with figures in the right column. These figures only show the 24 V transmitter housing. However, all housings share these same steps, except for the 48 V configurations that need to add the coil holder. Similarly to the IPSH, it is important to carefully examine each O-ring to make sure it is not damaged, and lubricate them with silicone grease to prevent damaging the rubber when assembling the components.

Table 16. Step by step assembly of the WCH

Step 1: The BlueRobotics™ Penetrator is connected to the lid with its corresponding nut. Through this penetrator passes a two-core cable from the same producer that conducts the power to and from the coils.	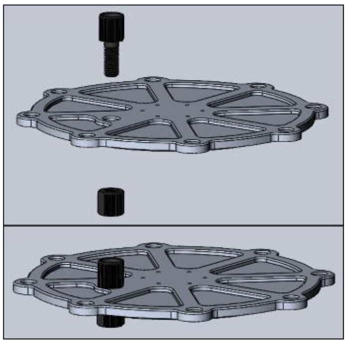
Step 2: The pillar is connected to the lid with an ISO 4026 M8 x 8 mm screw (hexagon socket set screws with flat point).	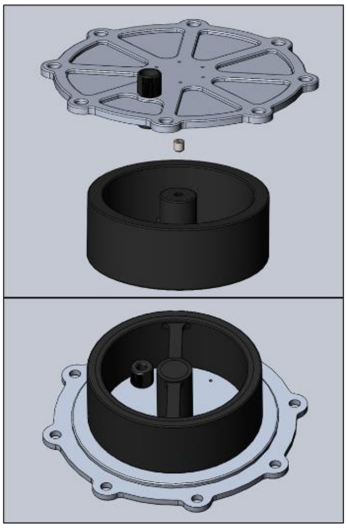
Step 3: The electronic components casings attached to the lid with an ISO 7380 M3 x 8 mm screw (hex socket button), the cables are connected, and the coil is placed on top of the joists (for the 24 V module) or the coil holder (for the 48 V module).	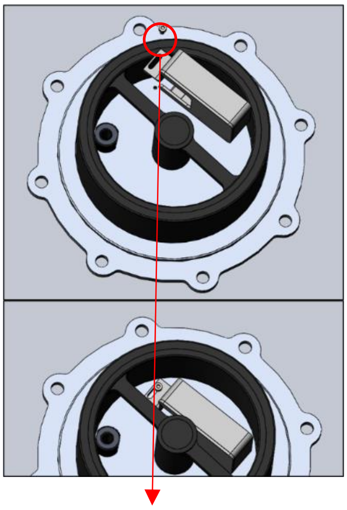

Step 4: The box is attached to the lid with eight ISO 7380 M8 x 20 mm screws (hex socket button) completing the assembly.

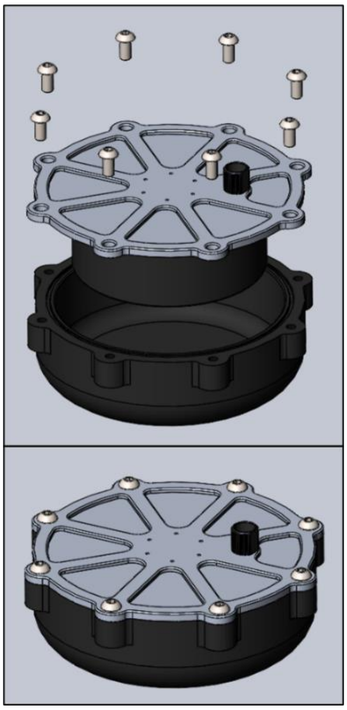

To verify the buoyancy, all component weights need to be quantified. The electronic components and the penetrator were weighted on a scale, as shown in Figure 42, while the box and lid were taken from the evaluate tool “mass properties” from SolidWorks. All component weights are shown in Table 17.

Figure 42. Measuring the 48 V transmitter electronic components plus casing.

Table 17. WCH components weight and buoyancy analysis

Wireless charger housing	
Component	**Weight [g]**
Electronic component receiver 24 + casing	83
Electronic component transmitter 24	85
Electronic component receiver 48	141
Electronic component transmitter 48	122
Lid	580
Box	797
Pillar 24	362
Pillar 48	320
ISO 4026 M8 x 8 screw	1.9
8 x ISO 7380 M8 x 16 screws	64
ISO 7380 M3 x 8 screw	0.5
Penetrator	14

All the different WCH modules total weights are calculated in Table 18, Table 19, Table 20, and Table 21. The exterior volume of the WCH is obtained via the "mass properties" tool of SolidWorks™, with a 3D model imitating the exterior aspect of the WCH assembly, as shown in Figure 43. The density of each configuration is obtained by dividing its weight with the WCH exterior volume and is then compared to the ρ_{sw}. equation (5) is then used to obtain the underwater apparent weight.

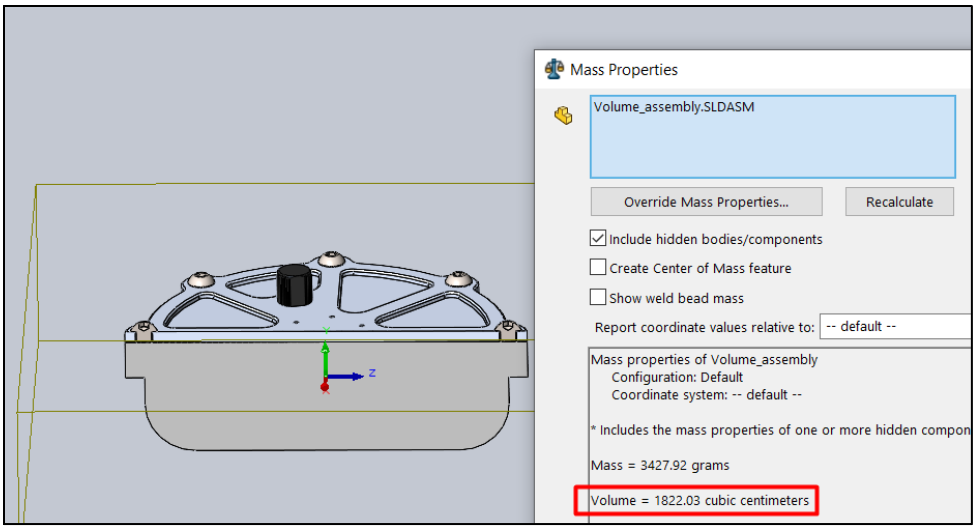

Volume_assembly.SLDASM

☑ Include hidden bodies/components
☐ Create Center of Mass feature
☐ Show weld bead mass
Report coordinate values relative to: -- default --

Mass properties of Volume_assembly
Configuration: Default
Coordinate system: -- default --

* Includes the mass properties of one or more hidden compon

Mass = 3427.92 grams

Volume = 1822.03 cubic centimeters

Figure 43. Solid body used to measure the total Volume of the WCH.

Table 18. WCH receiver 24 V total weight.

WCH receiver 24	
Component	**Weight [g]**
Electronic component receiver 24 + casing	83
Lid	580
Box	797
Pillar 24	362
ISO 4026 M8 x 8 screw	1.9
8 x ISO 7380 M8 x 16 screws	64
ISO 7380 M3 x 8 screw	0.5
Penetrator	14
∑	1888.4

Volume [cm^3]: 1822.6

Density [g/cm^3]: 1.036

Underwater apparent weight [g]: 20.3

Table 19. WCH transmitter 24 V total weight.

WCH transmitter 24	
Component	**Weight [g]**
Electronic component transmitter 24	85
Lid	580
Box	797
Pillar 24	362
ISO 4026 M8 x 8 screw	1.9
8 x ISO 7380 M8 x 16 screws	64
ISO 7380 M3 x 8 screw	0.5
Penetrator	14
∑	1890.4

Volume [cm^3]: 1822.6

Density [g/cm^3]: 1.037

Underwater apparent weight [g]: 22.3

Table 20. WCH receiver 48 V total weight.

WCH receiver 48	
Component	**Weight [g]**
Electronic component receiver 48 + casing	141
Lid	580
Box	797
Pillar 48	320
ISO 4026 M8 x 8 screw	1.9
8 x ISO 7380 M8 x 16 screws	64
ISO 7380 M3 x 8 screw	0.5
Penetrator	14
∑	1904.4

Volume [cm^3]: 1822.6

Density [g/cm^3]: 1.045

Underwater apparent weight [g]: 36.3

Table 21. WCH transmitter 48 V total weight.

WCH transmitter 48	
Component	**Weight [g]**
Electronic component transmitter 48	122
Lid	580
Box	797
Pillar 48	320
ISO 4026 M8 x 8 screw	1.9
8 x ISO 7380 M8 x 16 screws	64
ISO 7380 M3 x 8 screw	0.5
Penetrator	14
∑	1885.4

Volume [cm^3]: 1822.6

Density [g/cm^3]: 1.034

Underwater apparent weight [g]: 17.3

3.8.2.7 Wireless charger current transmission efficiency

The purpose of the wireless charger is to transfer current from a stationary dock to the AUV without a cable. Thus, the energy transmission efficiency is an important measure that determines the success of the WCH design. Power transfer via inductive charging is directly related to the distance and alignment of the coils. The transmitter is wired to the power supply and the power is set to 24 V or 48 V, depending on the module being tested. The receiver is wired to a rheostat where the resistance is determined using Ohms law (6), to achieve the output current given by the supplier (Table 7). The real current is measured with an ammeter and compared with the expected current. Figure 44 shows a schematic representation of the described circuit.

$$I = V/R \tag{6}$$

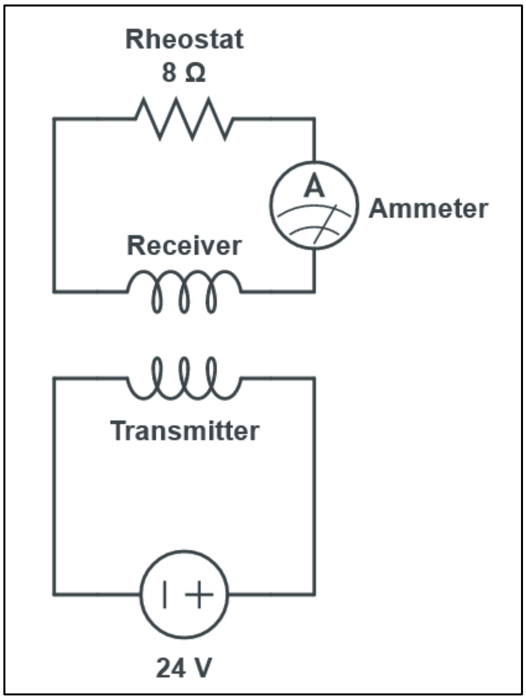

Figure 44. Simplified circuit used to test the energy efficiency of the WCH – 24 V

At the time the tests were performed, the 48 V module was damaged since it was not transferring any current. The cause of the damage is yet unknown. Thus, there was no power transfer between the coils. However, the 24 V module testing was more successful. The distance between coils is determined by the receiver and transmitter's box bottom walls, which is 7 mm thick. Therefore, the distance between coils is 14 mm. To achieve a current of 3 A, the receiver circuit needs 8 Ω (Figure 45) according to Ohms law. After the setup is complete, the power supply is turned on and the receiver begins to descend slowly until both the transmitter and receiver box's bottom walls are touching. Figure 46 shows both components already touching and the current that is being transferred to the receiver, which is 1.93 A. Comparing this current value (1.93 A) with the expected value (3 A), it is determined that the 24 V WCH module operates with an energy transmission efficiency of 64%.

Figure 45. Rheostat set to 8 Ω in 24 V circuit.

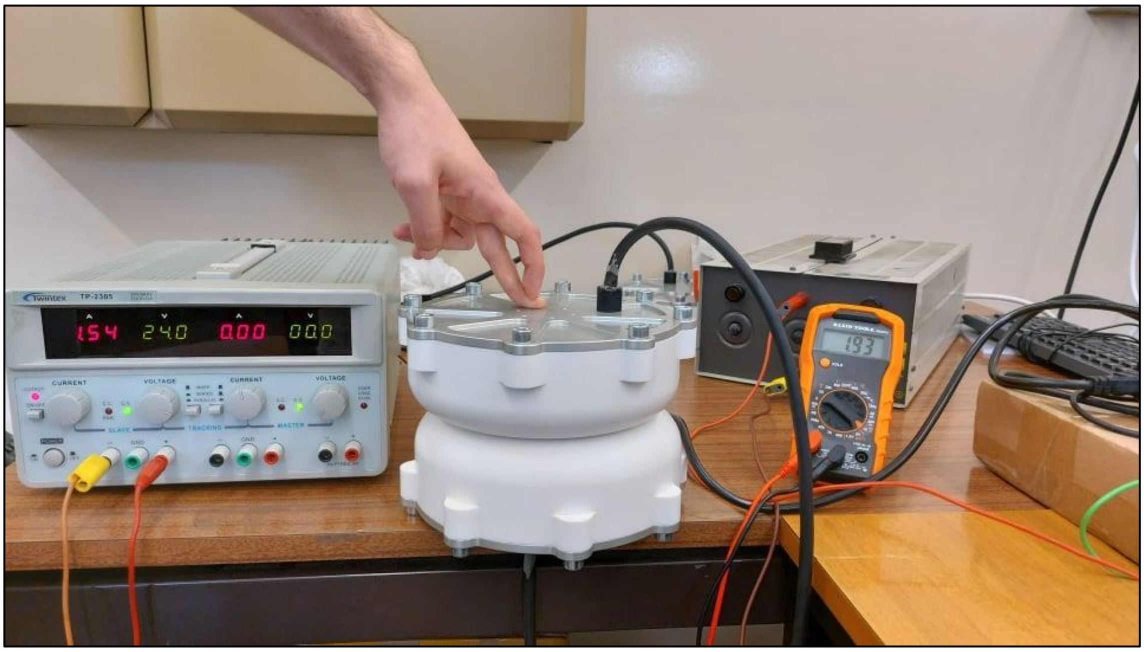

Figure 46. WCH 24 V module receiving current.

3.9 Structural validation

Traditionally, experimentation has been based on physical prototyping. However, this is usually very time and cost intensive, and consequentially, the main objective of physical prototyping has been verification in the later development phases. Virtual prototyping, or simulation, allows for more design iterations to be tested in a reduced time frame and significantly less cost than physical prototyping. Increasing the knowledge of the product and the probability of discovering more radical improvements and innovations. And reducing the number of physical prototypes and the probability of major rework in a later design phase [133].

Due to the application of the housings, their design calls for an optimized ratio between strength and weight, since it needs to endure the hydrostatic pressures at 300 meters depth, while maintaining an underwater apparent weight of 0. The housings materials follow Hooke's law of elasticity, exhibiting a linear elastic behavior while below their yield point. For this reason, and since the purpose of these simulations is to determine that there are no stress points above the admissible stress (σ_f/FOS), the analysis conducted are linear static.

The simulations conducted in this work were carried out in SolidWorks™ "simulation" add-on. This chapter only presents the final validation of the housings, despite that the design went through several iterations.

3.9.1 Underwater imaging perception system housing

3.9.1.1 Pre-processing

Pre-processing consists of the model preparation for the FEM analysis. Here the boundary conditions, loads, and mesh are defined. Thus, the steps followed for the model setup are detailed next. By far, the lengthiest task the computer must perform to solve these simulations is solving contact constraints. To simplify and speed-up this process, some simplifications are needed, such as reducing the number of components to only the structurally relevant ones. These simulations were executed with only the box and the lid. The pre-processing steps are defined sequentially as follows:

1st: The material's relevant properties for the analysis were assigned to their respective models. For this type of linear static analysis, the program requires the isotropic material properties for the Young's modulus and Poisson's ratio, and the material behavior must be linear elastic. SolidWorks™ also requests information on the density, despite gravity forces being assumed negligible in this model, and the yield point, which is not used in the numerical solver since it is a linear analysis. The SolidWorks™ material library already provides the AW 6061 – T6 properties. Figure 47 shows the window where the material inputs are listed.

2nd: The connections for the model are defined (Figure 48). For the IPSH there is a "no penetration" global contact, and 8 bolt connectors (ISO 7380 – M4 x 12) that connect the lid to the box. The bolt setup is automatically defined by the SolidWorks™ bolt function.

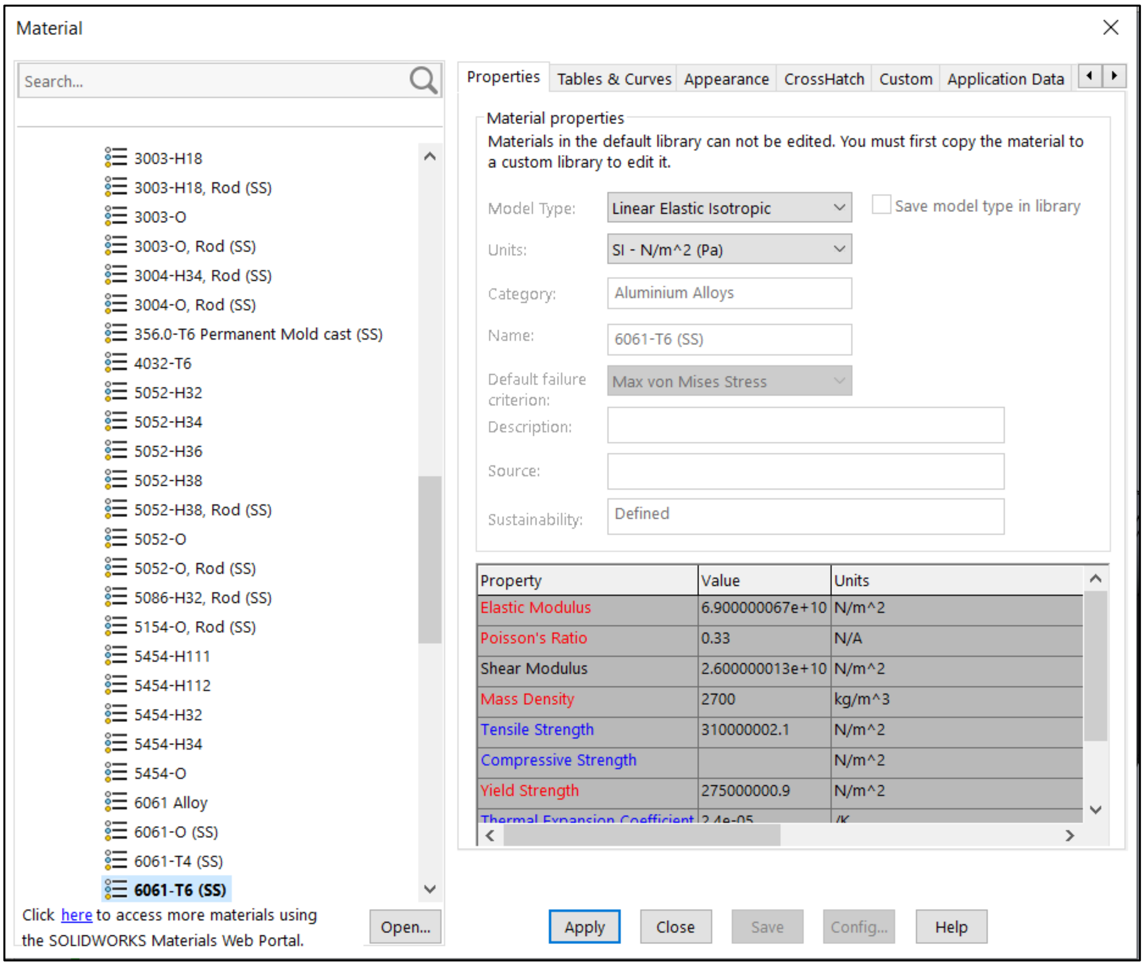

Material properties

Materials in the default library can not be edited. You must first copy the material to a custom library to edit it.

Model Type: Linear Elastic Isotropic ☐ Save model type in library

Units: SI - N/m^2 (Pa)

Category: Aluminium Alloys

Name: 6061-T6 (SS)

Default failure criterion: Max von Mises Stress

Description:

Source:

Sustainability: Defined

Property	Value	Units
Elastic Modulus	6.900000067e+10	N/m^2
Poisson's Ratio	0.33	N/A
Shear Modulus	2.600000013e+10	N/m^2
Mass Density	2700	kg/m^3
Tensile Strength	310000002.1	N/m^2
Compressive Strength		N/m^2
Yield Strength	275000000.9	N/m^2
Thermal Expansion Coefficient	2.4e-05	/K

Figure 47. AW 6061 – T6 properties input window for linear static analysis.

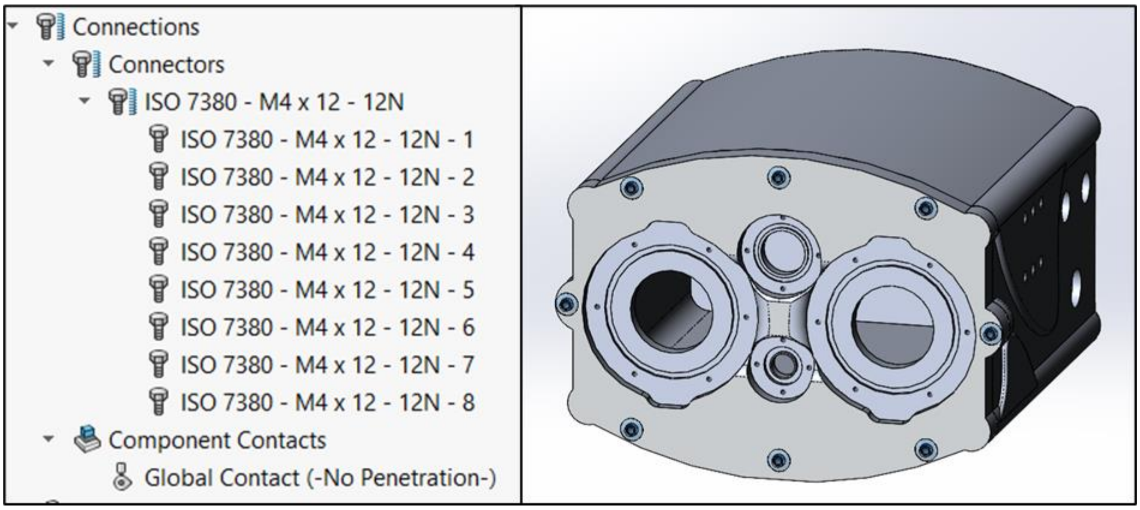
- Connections
  - Connectors
    - ISO 7380 - M4 x 12 - 12N
      - ISO 7380 - M4 x 12 - 12N - 1
      - ISO 7380 - M4 x 12 - 12N - 2
      - ISO 7380 - M4 x 12 - 12N - 3
      - ISO 7380 - M4 x 12 - 12N - 4
      - ISO 7380 - M4 x 12 - 12N - 5
      - ISO 7380 - M4 x 12 - 12N - 6
      - ISO 7380 - M4 x 12 - 12N - 7
      - ISO 7380 - M4 x 12 - 12N - 8
  - Component Contacts
    - Global Contact (-No Penetration-)

Figure 48. Connections defined for the WCH linear static analysis.

3rd: The fixtures, or boundary conditions, of the model are defined. The numerical solution is only possible if movement is restrained, and rigid body motion is prevented. Otherwise, the solution cannot reach equilibrium, and therefore it is unsolvable [97]. The fixture setup opted for this analysis restricts all translational displacements on the bottom outside connection holes and a virtual wall is applied in the same plane these holes are positioned (Figure 49) to represent the body where the is IPSH is connected. This setup is simulating the IPSH as if it were connected to another rigid body.

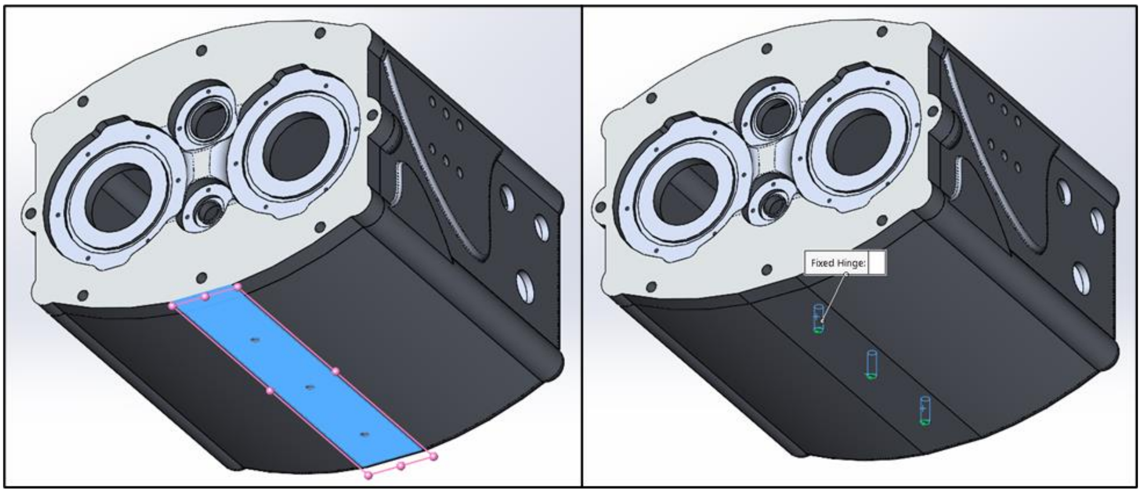

Figure 49. IPSH fixture setup

4th: Since the IPSH height is 110 mm between the top and bottom surfaces, by applying equation (3), the pressure differential amounts to 0.00110 MPa, which is negligible compared to 1.5 MPa. To emulate the hydrostatic pressure at 150 meters, a constant pressure load of 1.5 MPa normal to the selected faces is applied to all exterior surface areas that are in direct contact with water. These surfaces are highlighted in blue in Figure 50.

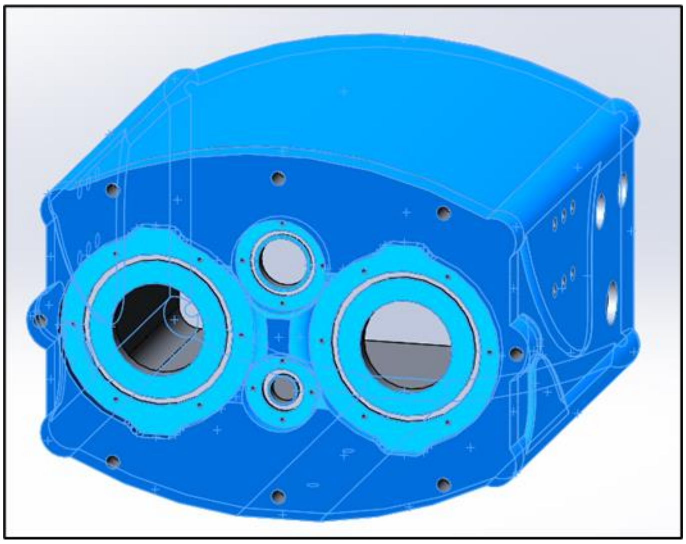

Figure 50. Area for pressure application in the IPSH

5th: Lastly, the mesh is created using 3D tetrahedral elements. Mesh manipulation can greatly improve the efficiency of the analysis. This process is done by refining the mesh in the areas where the stress gradient is more accentuated. This leads to a better resource utilization, improving the numerical solution time, with accurate results. For a better degree of trust in the model solution, the mesh should be refined until the results start converging. However, this can lead to exceedingly refined meshes, especially with more complex topologies, which would require more computational resources than what is available. The mesh is refined in areas where stress concentration is expected, i.e. corners, holes, abrupt geometry changes, and contact areas between components (highlighted in blue in Figure 51, Figure 52, and Figure 53, Figure 54).

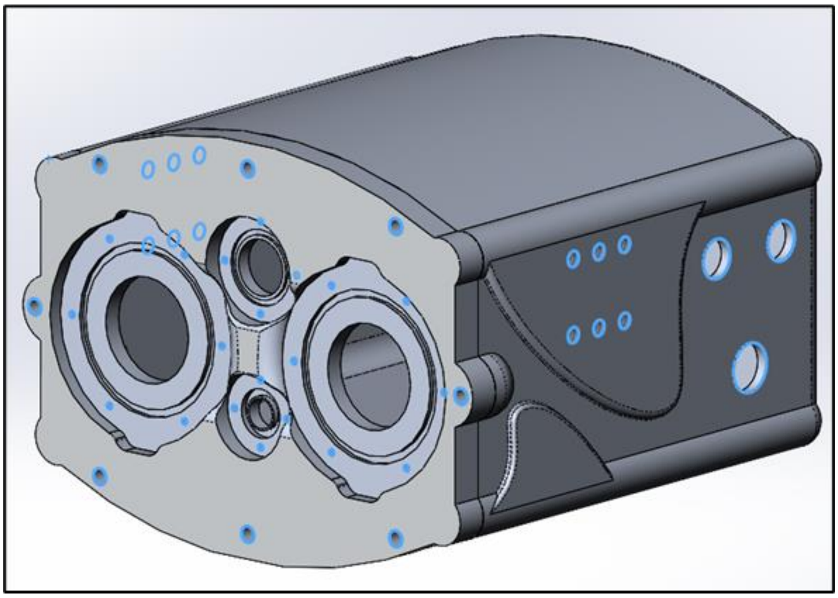

Figure 51 IPSH holes at the side walls and lid mesh refinement.

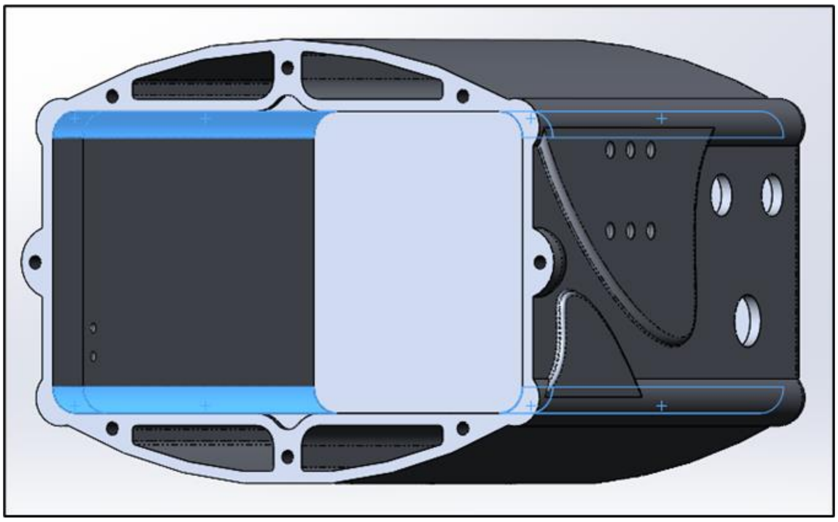

Figure 52. IPSH box corners mesh refinement.

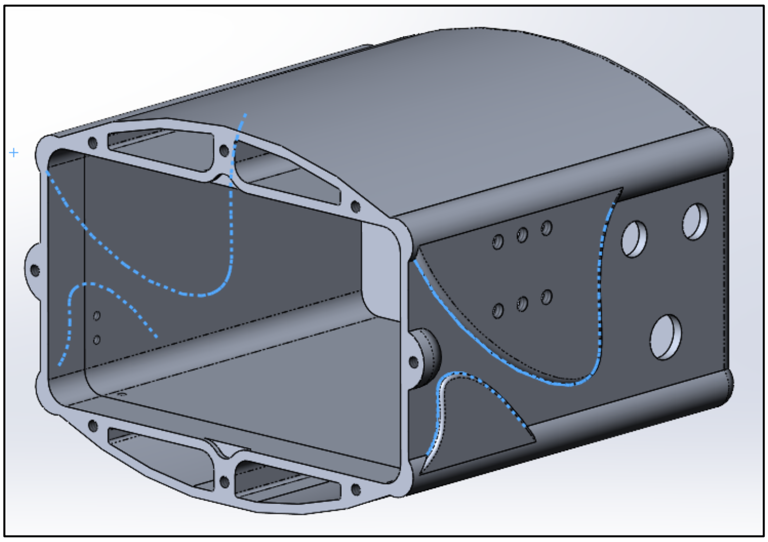

Figure 53. IPSH wave forms mesh refinement.

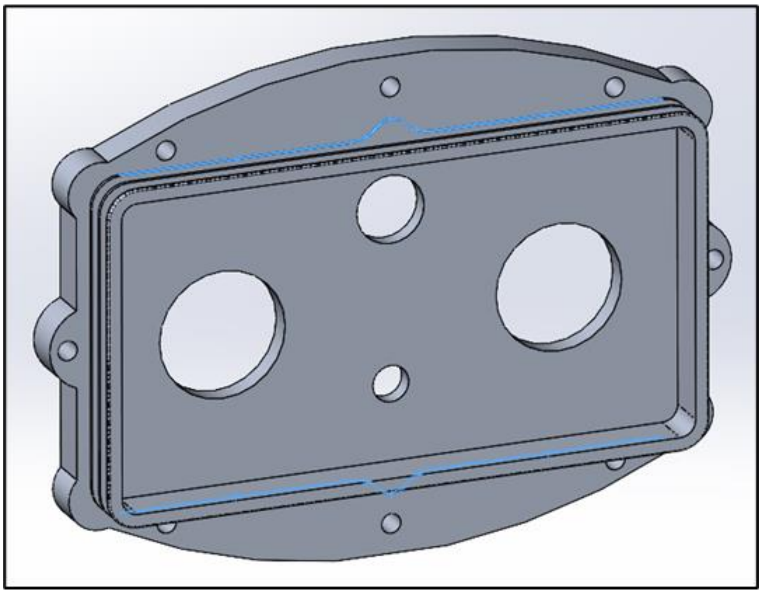

Figure 54. IPSH lid-box contact area mesh refinement.

3.9.1.2 Simulation and post processing

The simulation solver of choice is the Direct sparse solver. This method solves the set of equations directly without any approximations, thus providing more accurate results.

Figure 55 and Figure 56 show the von Mises stress results from the linear static analysis of the IPSH box and the lid, respectively. The highest stress point in the box is 202 MPa. However, this stress point coincides with one of the defined fixtures, which is most likely to be the cause for such a high stress. Dismissing this value, the highest stress induced on the box component takes place at the ethernet hole nearing the center of the side wall (signaled by the red arrow in Figure 55) with a value of 194 MPa. This result is coherent, since it occurs at the center of the wall where the strain is largest which, paired with the abrupt change in geometry induced by the hole, makes this spot prone to stress concentration.

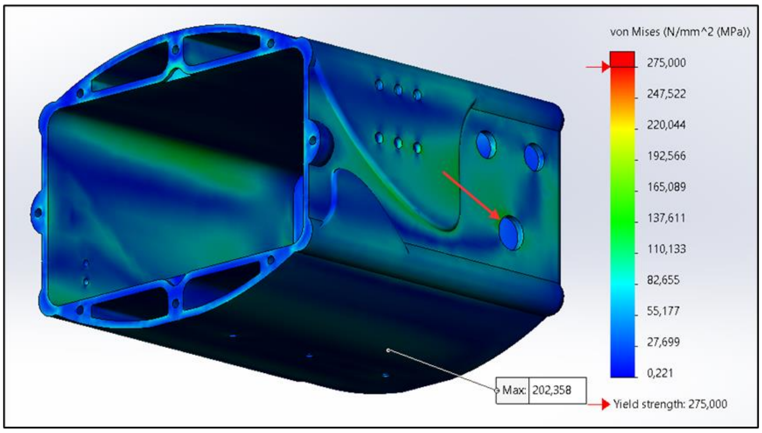

Figure 55. IPSH assembly linear static analysis results – von Mises stress - Box structural validation.

The highest calculated stress in the lid is 195 MPa and it is located in one of the holes that secure the lid to the box. More specifically, it takes place where the lid is restricted from deforming outwards. Thus, a higher stress concentration is expected in these areas.

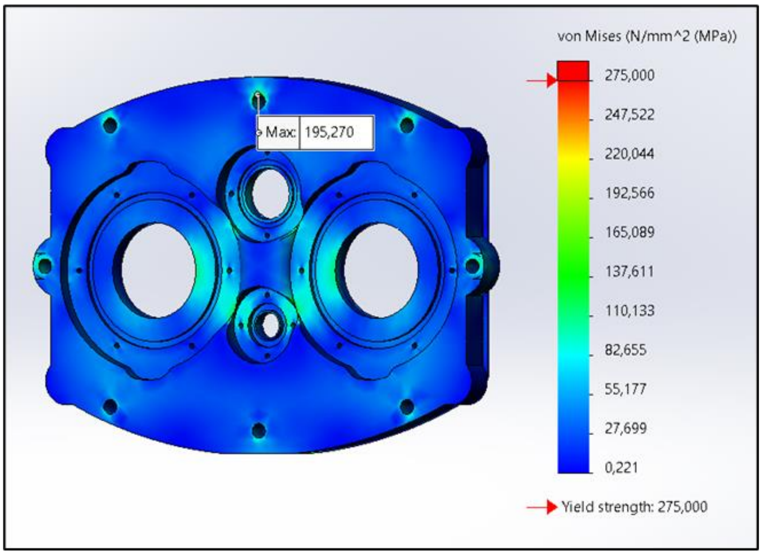

Figure 56. IPSH assembly linear static analysis results – von Mises stress - Lid structural validation.

Table 22 shows the maximum stress values and FOS obtained by dividing the maximum stress by the yield stress of the material. The simulations discussed in this chapter were made using the mechanical properties of AW 6061 – T6. However, since the AW 6082 – T6 mechanical properties used by the solver (Young's modulus and Poisson coefficient) are the same, the results are still accurate. Instead, the yield stress of AW 6082 is used to calculate the FOS.

Table 22. IPSH components - max stress and FOS

Components		Max stress [MPa]	Yield stress [MPa]	FOS
IPSH	Lid	195	260	1.3
	Box	194	260	1.3

3.9.2 Underwater wireless charger housing

3.9.2.1 Pre-processing

In this section the boundary conditions, loads, and mesh are defined for the WCH model. The pre-processing stage of the WCH follows the same steps as the IPSH, and only the structurally relevant components are included.

1st: Since the POM-H is not part of the library, the material properties were inserted manually by creating a custom material. Figure 57 shows the window where the material inputs are inserted.

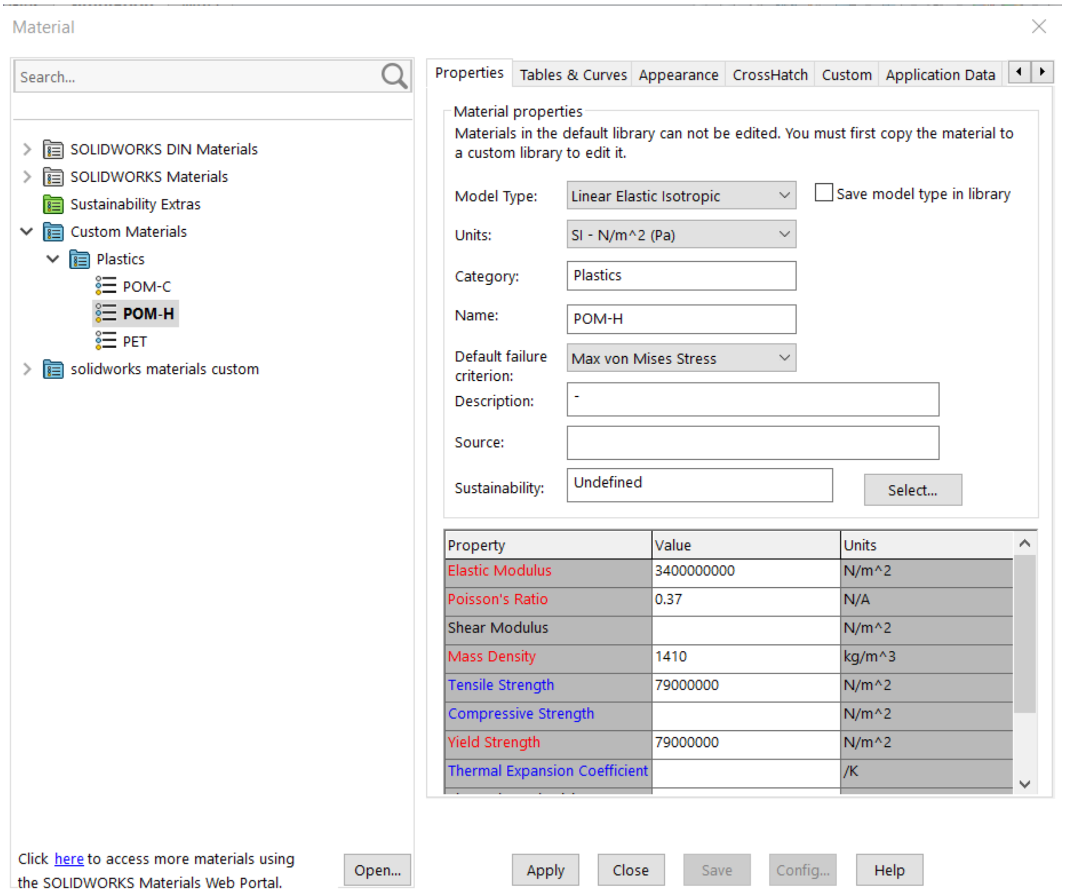

Click here to access more materials using the SOLIDWORKS Materials Web Portal.

Material properties

Materials in the default library can not be edited. You must first copy the material to a custom library to edit it.

Model Type: Linear Elastic Isotropic

☐ Save model type in library

Units: SI - N/m^2 (Pa)

Category: Plastics

Name: POM-H

Default failure criterion: Max von Mises Stress

Description: -

Source:

Sustainability: Undefined

Property	Value	Units
Elastic Modulus	3400000000	N/m^2
Poisson's Ratio	0.37	N/A
Shear Modulus		N/m^2
Mass Density	1410	kg/m^3
Tensile Strength	79000000	N/m^2
Compressive Strength		N/m^2
Yield Strength	79000000	N/m^2
Thermal Expansion Coefficient		/K

Figure 57. POM-H properties input window for linear static analysis.

2nd: The connections for the model are defined (Figure 58). For the WCH there is a "no penetration" global contact, and 8 bolt connectors (ISO 7380 – M8 x 20) that connect the lid to the box.

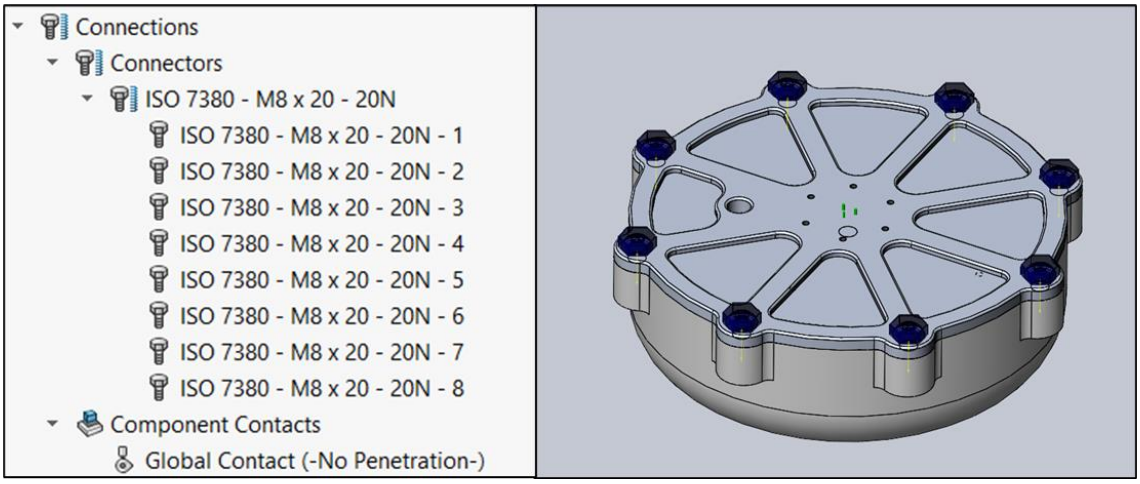

Figure 58. Connections defined for the WCH linear static analysis.

3rd: Constraining displacements in the M3 holes on the lid lead to unreasonably high stress points around those holes, leading to unsatisfied and even odd results. Instead, the fixtures were applied by fully restraining displacements in all directions in the lid-pillar connection and locking the rotation of the pillars, as shown in Figure 59. This set of boundary conditions led to stress concentration on the pillar hole, which is ignored, since in the real physical model, the hole is not completely restricted. However, the rest of the model showed more coherent results, deeming this approach successful.

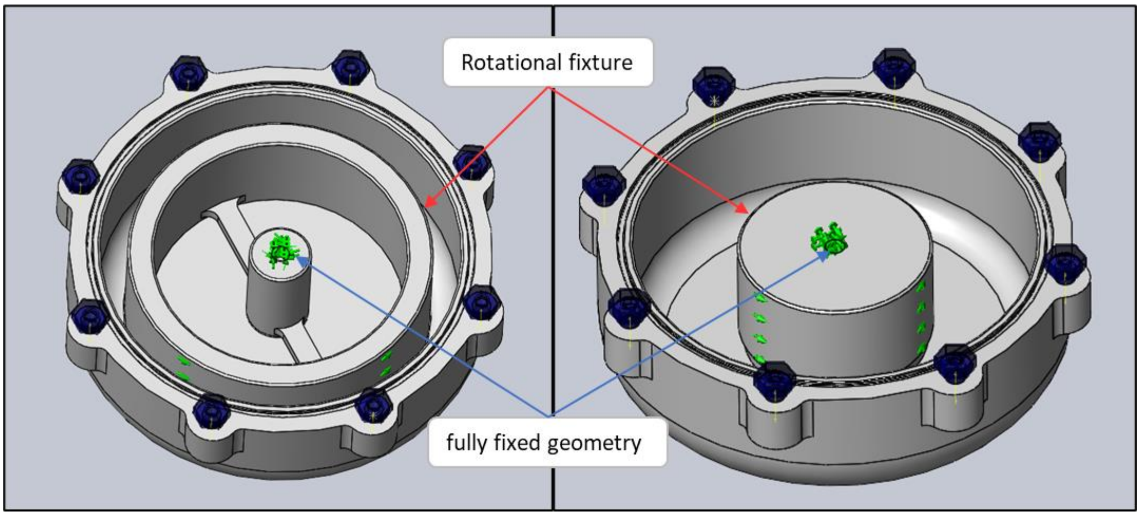

Figure 59. WCH fixture setup.

4th: The WCH height is 67 mm between the top and bottom surfaces Applying equation (3), the pressure differential amounts to 0.00067 MPa which is negligible compared to

3 MPa. A constant pressure load of 3 MPa is applied in all exterior surface areas that are in direct contact with water. These surfaces are highlighted in blue in Figure 60.

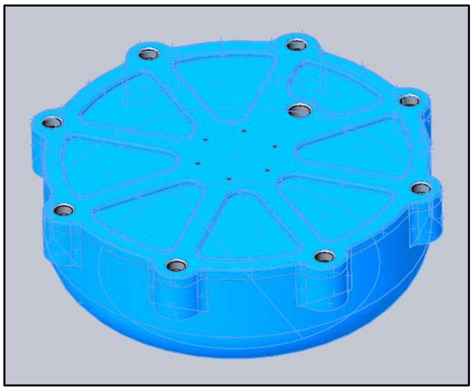

Figure 60. Pressure loads applied in the WCH.

5th: Finally, the mesh is created using 3D tetrahedral solid elements. All areas of contact between elements, corners, and holes (highlighted in blue in Figure 61, Figure 62, and Figure 63) have a more refined mesh than the rest of the model, since stress concentration is expected in these areas.

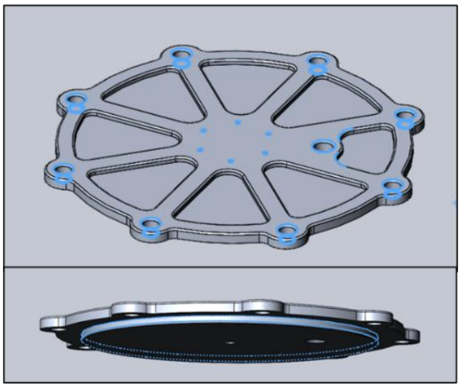

Figure 61. WCH lid mesh refinement.

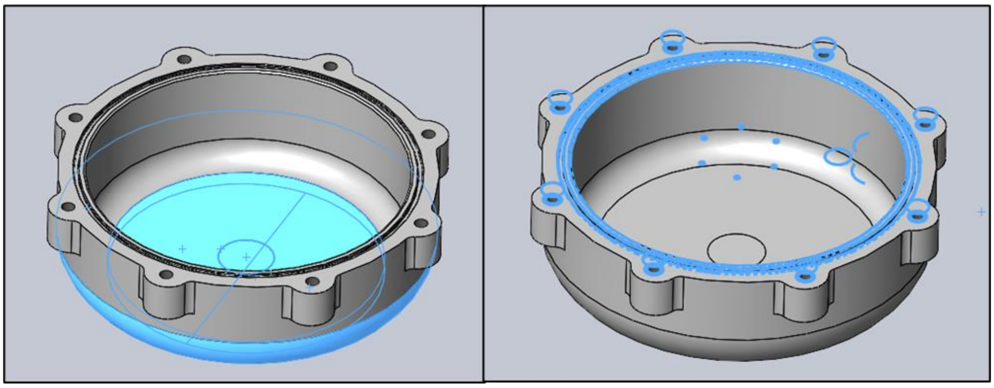

Figure 62. WCH box mesh refinement.

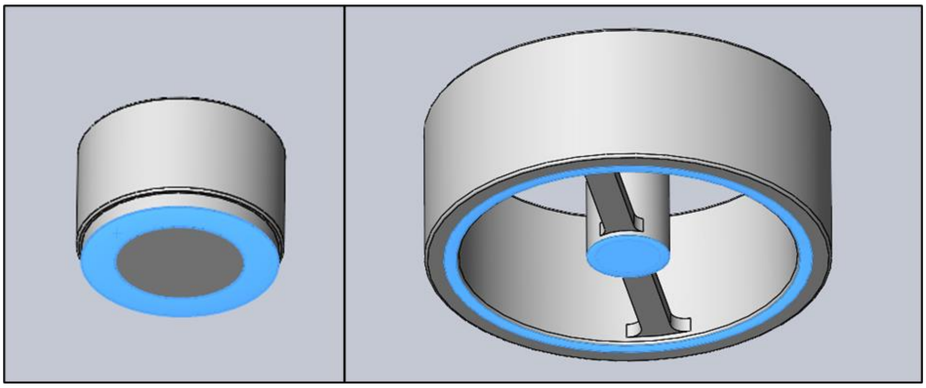

Figure 63. WCH pillars mesh refinement.

3.9.2.2 *Simulation and post processing*

The simulation solver of choice is the FFEPlus, due to its lower hardware requirements. This is an iterative solver, so the results may not be as accurate as direct solvers. However, for large problems, with a high number of degrees of freedom (typically over 100000) this is a much more efficient and faster solver.

In Figure 64 and Figure 65, the linear static analysis calculated von Mises stresses for the lid are presented. Overall, the stress is larger in the 48 V assembly. This difference is due to pillar configuration, since the pillar 24 outer ring provides better support to the lid than pillar 48. This is more evident by analyzing the rib's central areas, which is supported by the pillar 24 outer ring, and the stress is much lower. The higher stress values are 148 MPa for the 24 V assembly and 153 MPa for the 48 V assembly.

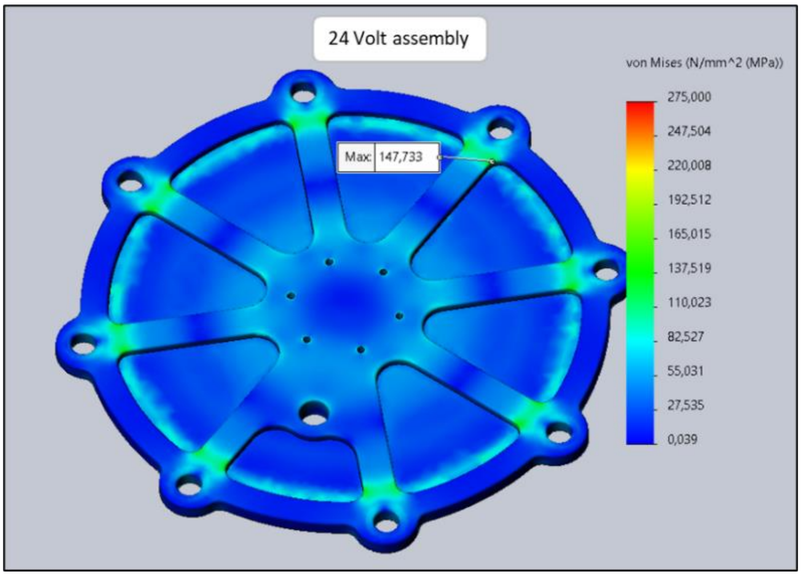

Figure 64. 24 V assembly linear static analysis results – von Mises stress - Lid structural validation.

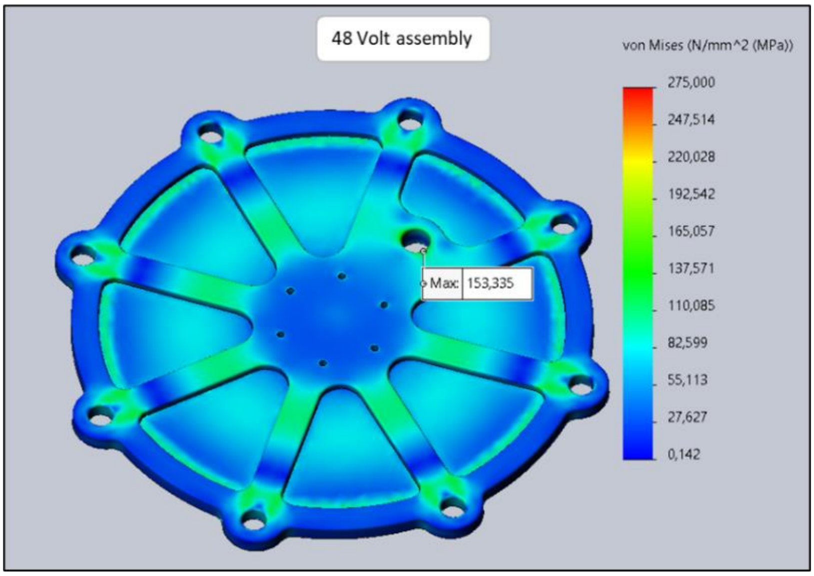

Figure 65. 48 V assembly linear static analysis results – von Mises stress - Lid structural validation.

Dismissing the stress concentration in the M8 hole that connects the pillars to the lid, the results shown in Figure 66 and Figure 67, showing that both pillars have higher stresses in the box-pillar interface, rather than in the lid-pillar interface. This can be attributed to the lower Young's modulus of POM-H, which causes higher displacements in the box, and therefore a harsher contact between the pillar and the box. Dismissing the stress concentration in the M8 hole (due to the fixture applied in the pre-processing phase), the highest stress is found at the bottom area of the pillars. Pillar 48 has a stress of 15 MPa, while pillar 24 has a stress of 48 MPa. Pillar 48 could be further optimized, but this design shares a similar weight with the pillar 24, which helps maintaining a similar weight between modules as well.

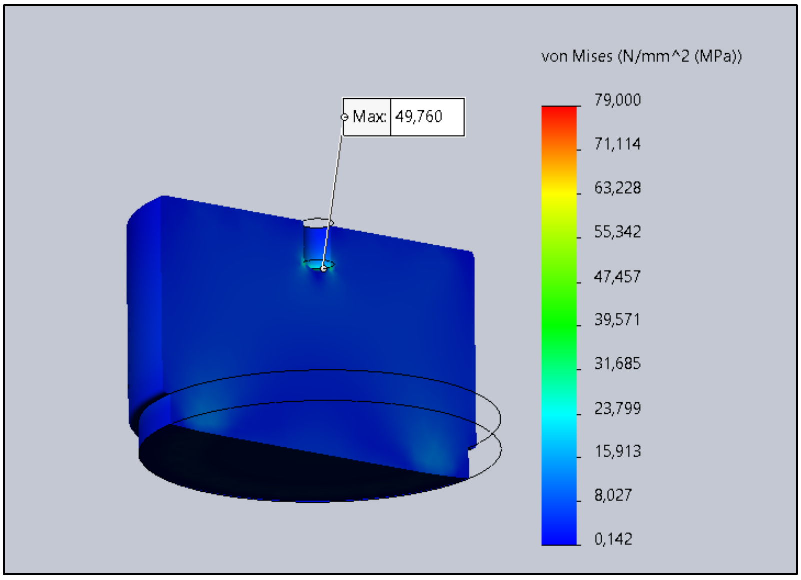

Figure 66. 48 V assembly linear static analysis results – von Mises stress - Pillar 48 structural validation.

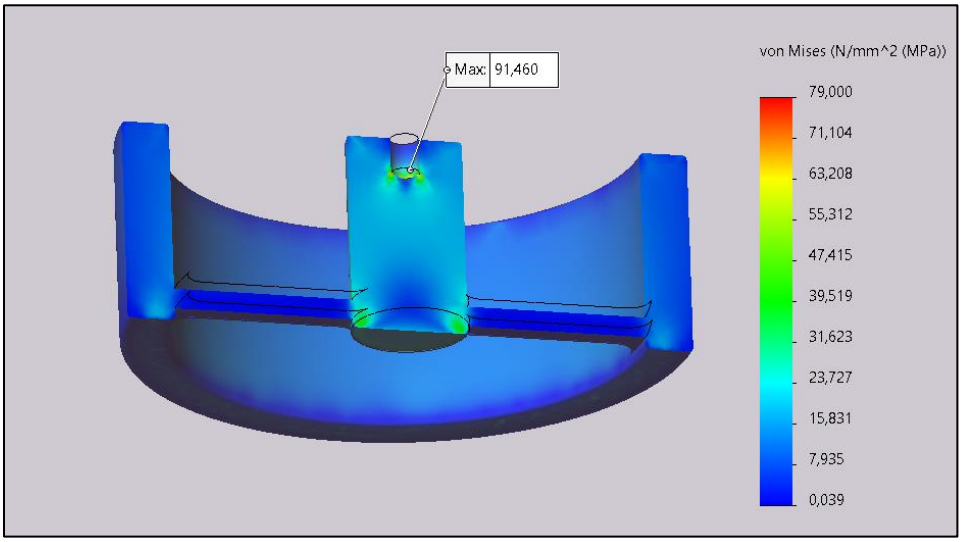

Figure 67. 24 V assembly linear static analysis results – von Mises stress - Pillar 24 structural validation.

These curvatures help preventing the concentration of stress around those edges, thus being a critical aspect of this design. Figure 68 shows an earlier iteration where the corners were filleted instead of the curvature displayed in the final design. The stress around the edge reached 130 MPa.

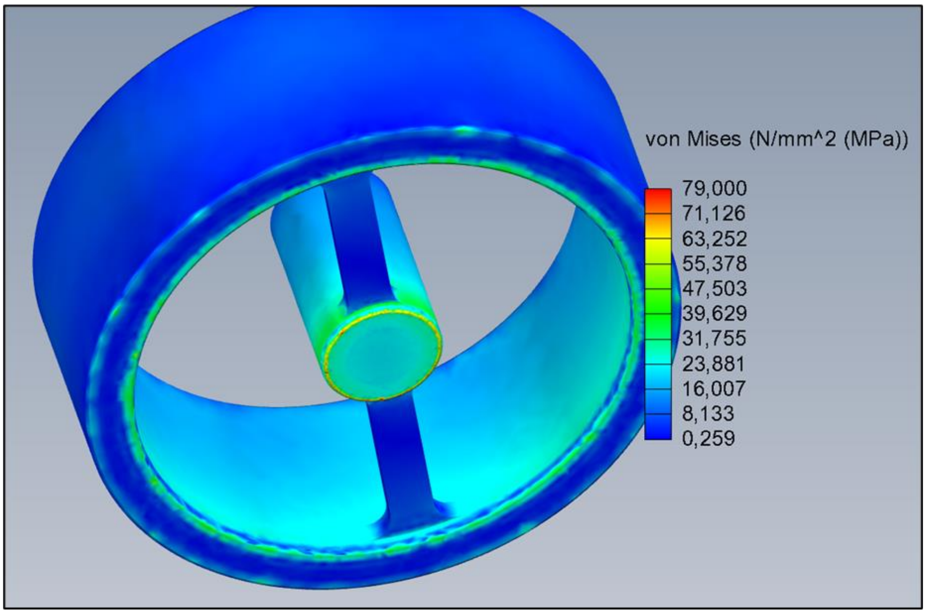

Figure 68. Stress concentration around the edge of the center column of pillar 24 from an early iteration.

The box results (Figure 69 and Figure 70) display odd singularities in the box interface with the lid boss. There was an attempt to eliminate this problem by further refining the mesh, but the available hardware could not preform the analysis. Still these nodes are scarce and follow no apparent pattern that could infer that these concentrations are legitimate. Dismissing these random nodes, the higher stress values for both assembly boxes are 53 MPa, although, these appear in different zones. In the 24 V assembly, the highest stress zone is near the center of the box, while in the 48 V assembly it is in the curvature zone. This behavior can be attributed once again to the pillar configuration. At the center there is a larger contact area between pillar 48 and the box, so lower stresses than the 24 V assembly are expected. However, the outer ring of pillar 24 restricts the displacement of the box corners, leading to a lower stress in that zone when compared to the 48 V assembly.

Table 23 shows the stress points and FOS obtained by dividing the maximum stress by the yield stress of the material. The simulations discussed in this chapter were made with the properties of POM-H. However, since the PET mechanical properties, namely the Young’s modulus and Poisson coefficient are very similar, the results would not be much different. So, the yield stress of PET is used to calculate the FOS.

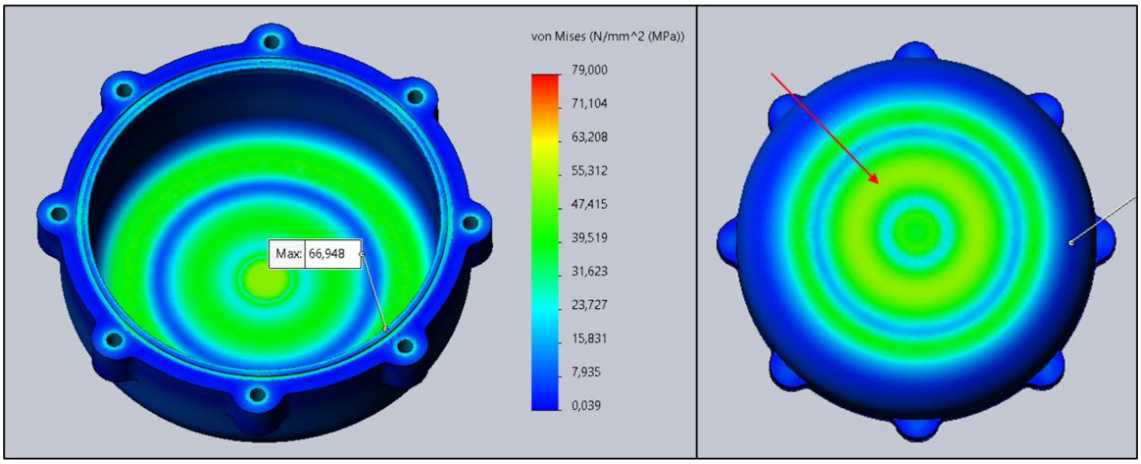

Figure 69. 24 V assembly linear static analysis results – von Mises stress - Box structural validation.

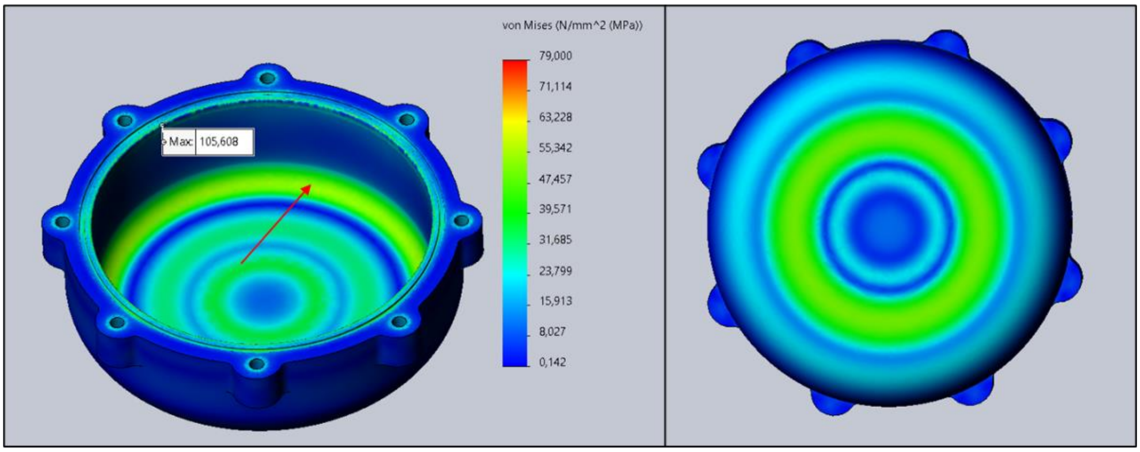

Figure 70. 48 V assembly linear static analysis results– von Mises stress - Box structural validation.

Table 23. WCH components - max stress and FOS

Components		Max stress [MPa]	Yield stress [MPa]	FOS
24 V Assembly	Lid	148	275	1.9
	Box	53	91	1.7
	Pillar 24	48	91	1.9
48 V Assembly	Lid	153	275	1.8
	Box	53	91	1.7
	Pillar 48	15	91	6.1

3.10 Pressure chamber test

To validate the FEA results obtained in section 3.9, the housings are experimentally subjected to an equivalent pressure of 1.5 MPa for the IPSH and 3 MPa for the WCH. This pressure is generated inside a pressure chamber, or hyperbaric chamber, located at the CRAS center ISEP facilities (Figure 71), with a 200-bar capacity (equivalent to 2000 meters depth). These tests verify if the assembled housing is completely waterproof by examining the pressure rate and the interior of the components once the test is complete. Although there is no concrete available way of verifying the stresses obtained via FEA, the structural integrity can be observed by examining the components and visualize any fractures or plastic deformations that may have occurred. If none are found and the interior of the housing is dry, then the product is validated.

Figure 71. Pressure chamber at ISEP - CRAS laboratory.

Pressure chambers are usually made of steel and possess very thick walls to be able to withstand the extreme pressures induced inside. Thus, the pressure chamber is extremely heavy, and caution is needed when operating this device. First, the lid is lifted with the help of a crane, as seen in Figure 72. At the underside of the lid, there are four connectors used to attach the tested subjects with a cord and a shackle, as seen in Figure 73, to prevent them from sinking to the bottom, which would make them difficult to retrieve. Subsequently, the lid is lowered in place and the bolts are manually fastened with nuts to tightly close the chamber. The sealing of the chamber is assured with a gasket that located between the interface of the chamber and the lid. Then water is added to the chamber from the bottom tap until it starts pouring out from the tap at the top of the lid – meaning it is completely full, then the taps are closed. It is common practice at CRAS to test components for an hour, while registering the pressure every second.

Figure 72. Pressure chamber lid being lifted with a crane

Figure 73. WCH tied to the lid connector with a cord and a shackle.

The IPSH was tested for 1 hour 18 minutes and 36 seconds total since the beginning of the log being recorded. The pressure was set to 15 bar, the equivalent to 150 meters depth. All exterior components were tested, except the ethernet cable, where a dummy was used instead. Figure 74 shows the registered pressure inside the hyperbaric chamber. Testing occurred as expected and it was validated since there was no pressure drop for the entire duration of the test.

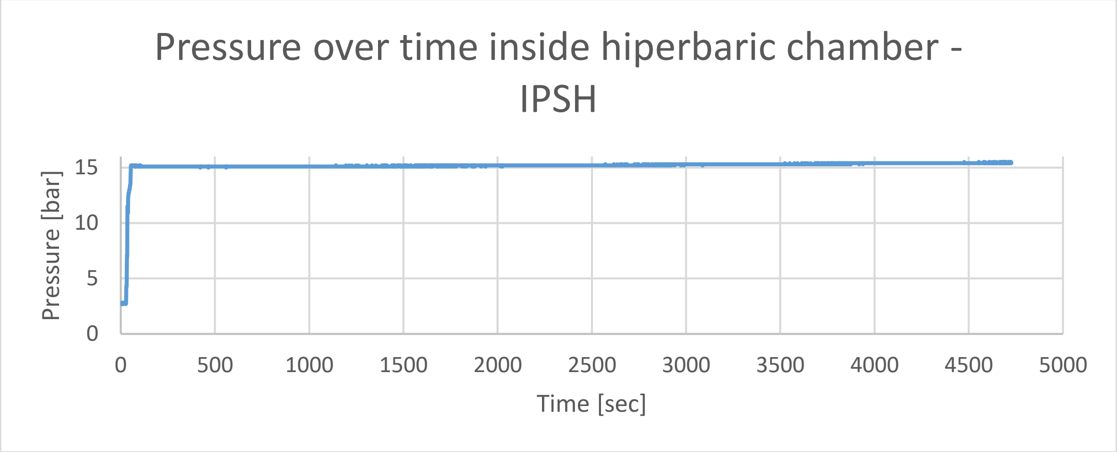

Figure 74. Pressure over timer inside hyperbaric chamber – IPSH

The WCH was tested for 1 hour, 1 minute and 47 seconds total since the log record was initiated. The pressure was set to 30 bar, the equivalent to 300 m depth. However, only the structural components were tested, while dummies were used instead of the penetrators. One of each WCH versions (24 and 48 V) were tested. Figure 75 shows the registered pressure inside the hyperbaric chamber over the duration of the test. Similarly to the IPSH, the test was validated since there was no pressure drop for the entire duration of the test.

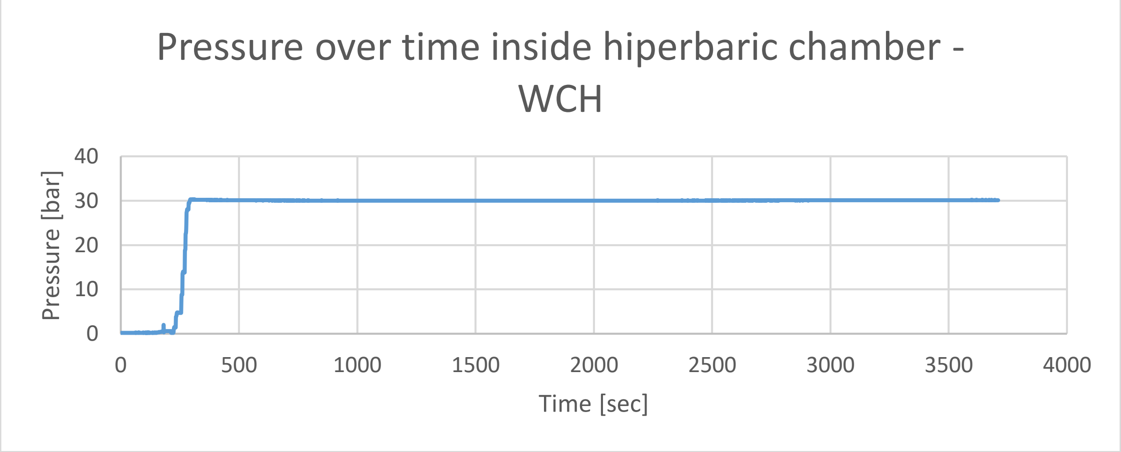

Figure 75. Pressure over timer inside hyperbaric chamber – WCH

After the tests are concluded the WCH and IPSH exterior are cleaned and dried with paper towels. Inspection proceeded with disassembling the housings and examining if the interior is dry. Then each component is visually observed for any plastic deformation or fractures that may have occurred. The test subjects of the WCH and IPSH were both dry and undeformed, which validates the FEA studies described in section 3.9, validating the IPSH for 150 meters depth rate and the WCH for 300 meters depth rate. Both housings can be seen in Figure 76, after they were extracted from the pressure chamber.

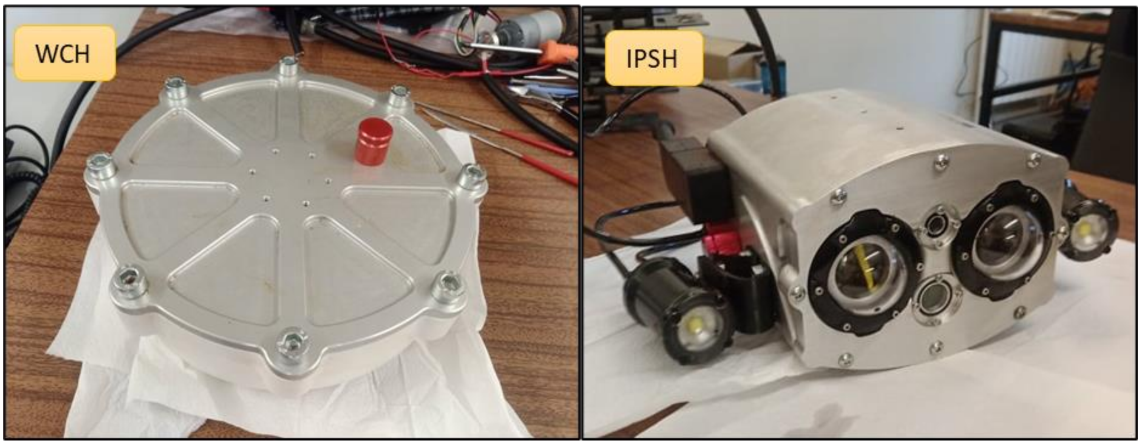

Figure 76. WCH and IPSH after the pressure chamber tests.

CONCLUSIONS AND FUTURE WORK PROPOSALS

4 CONCLUSIONS AND FUTURE WORKS PROPOSALS

This thesis described the design and development process of two AUV component housings. The visual scorecards (introduced in section 3.5) of the IPSH can be seen in Table 24, and of the WCH in Table 25. While the main objective of the housings is achieved by resisting the planned pressure rates, these scorecards provide a more detailed analysis regarding which design features design can be further improved, and which ones were successfully achieved.

Table 24. IPSH design visual scorecard.

MARESye					**Goals**
Design goals		**Performance**	**Effectiveness [%]**	**Efficiency [%]**	
Neutral Buoyancy	Assembly	1.098 [g/cc]	91.07		1.025 [g/cc]
Factor of safety	Lid	1.3	86.67		1.5
	Box	1.3	86.67		

Table 25. WCH design visual scorecard.

Wireless Charger					**Goals**
Design goals		**Performance**	**Effectiveness [%]**	**Efficiency [%]**	
Energy transmission	Assembly 24	1.93 A	64.33		3 [A]
	Assembly 48	-	-		
Neutral buoyancy	Assembly 24 receiver	1.036 [g/cc]	96.53		1.025 [g/cc]
	Assembly 24 transmitter	1.037 [g/cc]	96.43		
	Assembly 48 receiver	1.045 [g/cc]	95.69		
	Assembly 48 transmitter	1.034 [g/cc]	96.71		
Factor of Safety	Box	1.7	100.00	88.24	1.5
	Lid	1.8	100.00	83.33	
	Pillar 24	1.6	100.00	93.75	
	Pillar 48	5.7	100.00	26.32	

Both housings could not attain a neutral nor positive buoyancy. While the housings apparent underwater weight is still very reduced, these designs could greatly benefit from topology optimization to improve material distribution and reduce the density of these prototypes. However, the attained performance is still acceptable, considering the compromise between buoyancy (more volume) and compactness (less volume).

The FOS allows to identify which components are candidates for further mass reduction. As per standard industry practices, the design FOS goal is 1.5. This value is directly related to the degree of confidence in the product’s structural performance. Analyzing the achieved factor of safety for each component allows to identify which are overperforming or underperforming. While the IPSH components have not achieved neither the FOS, an FOS of 1.3 is still reliable, especially when dealing with well-known and commonly used materials, which is the case. Plus, the lower FOS translates to less weight as well. On the other hand, all WCH components achieved this goal, with a good efficiency rate, except the pillar 48 which has a 5.7 FOS. However, due to the focus on modular design of the WCH it is advantageous that both pillar 24 and pillar 48 have a similar weight, and so the different modules have similar weight. The aspect that can be improved the most in the WCH design is the effectiveness of the energy transmission, which can be achieved with a thinner bottom wall, or by developing a wireless system specifically for this application.

The iterative methodology used to design and develop these housings allowed to achieve a physical prototype that is functional and ready to be implemented in an AUV. Throughout the design process, the use of FEA validated the weight savings while the pressure requirements were successfully met. This was achieved by identifying critical zones, prone to high stresses, and non-critical zones, where mass could be removed, and thus achieve a better material distribution, and optimize the design for weight reduction. The physical validation of the housings in a pressure chamber further testifies the successful application of this methodology. And the visual scorecards proved to be a good communication tool, that easily allow to identify which aspects the design can be further improved. Overall, the housings design was successful. However, further improvements can be achieved with:

- Further topology and material distribution optimization;
- Improvement and adaptability of the wireless charger system for an underwater application (i.e., designing the coils so that it allows for a larger center pillar);
- Exploring composite options for the design of underwater housings;
- Study and optimize the hydrodynamic interactions of these components while the AUV is in mission;
- Designing the housings for more depth rate;
- Measurement of tensile strength during pressure test using strain gauges, and comparison with the simulated model;
- Identifying high deformation areas with an interior brittle coating.

BIBLIOGRAPHY AND OTHER SOURCES OF INFORMATION

5 BIBLIOGRAPHY AND OTHER SOURCES OF INFORMATION

[1] J. Ladenburg, P. Hevia-Koch, S. Petrović, and L. Knapp, “The offshore-onshore conundrum: Preferences for wind energy considering spatial data in Denmark,” *Renew. Sustain. Energy Rev.*, vol. 121, p. 109711, Apr. 2020, doi: 10.1016/j.rser.2020.109711.

[2] I. Arrambide, I. Zubia, and A. Madariaga, “Critical review of offshore wind turbine energy production and site potential assessment,” *Electric Power Systems Research*, vol. 167. Elsevier Ltd, pp. 39–47, Feb. 01, 2019. doi: 10.1016/j.epsr.2018.10.016.

[3] S. Heshmati-alamdari, A. Nikou, K. J. Kyriakopoulos, and D. V. Dimarogonas, “A Robust Force Control Approach for Underwater Vehicle Manipulator Systems,” *IFAC-PapersOnLine*, vol. 50, no. 1, pp. 11197–11202, Jul. 2017, doi: 10.1016/j.ifacol.2017.08.1245.

[4] S. W. Moore, H. Bohm, and V. Jensen, *Underwater Robotics : Science, Design & Fabrication*. Monterey, USA: Marine Advanced Technology Education (MATE) Center, 2010.

[5] A. Sahoo, S. K. Dwivedy, and P. S. Robi, “Advancements in the field of autonomous underwater vehicle,” *Ocean Engineering*, vol. 181. Elsevier Ltd, pp. 145–160, Jun. 01, 2019. doi: 10.1016/j.oceaneng.2019.04.011.

[6] M. Carreras, J. D. Hernandez, E. Vidal, N. Palomeras, D. Ribas, and P. Ridao, “Sparus II AUV - A Hovering Vehicle for Seabed Inspection,” *IEEE J. Ocean. Eng.*, vol. 43, no. 2, pp. 344–355, Apr. 2018, doi: 10.1109/JOE.2018.2792278.

[7] J. D. Hernández, K. Istenič, N. Gracias, N. Palomeras, R. Campos, E. Vidal, R. García, and M. Carreras, “Autonomous underwater navigation and optical mapping in unknown natural environments,” *Sensors (Switzerland)*, vol. 16, no. 8, p. 1174, Aug. 2016, doi: 10.3390/s16081174.

[8] R. Salazar, V. Fuentes, and A. Abdelkefi, “Classification of biological and bioinspired aquatic systems: A review,” *Ocean Engineering*, vol. 148. Elsevier Ltd, pp. 75–114, Jan. 15, 2018. doi: 10.1016/j.oceaneng.2017.11.012.

[9] H. Cozijn, H. Van Der Schaaf, B. De Kruif, and E. Ypma, “Design of an Underwater Vehicle for use in Basin Experiments, Development of MARIN’s Modular AUV,” in *IFAC-PapersOnLine*, 2019, vol. 52, no. 21, pp. 21–26. doi: 10.1016/j.ifacol.2019.12.277.

[10] M. Marcin, S. Adam, Z. Jerzy, and M. Marcin, “Fish-like shaped robot for

underwater surveillance and reconnaissance – Hull design and study of drag and noise," *Ocean Eng.*, vol. 217, p. 107889, Dec. 2020, doi: 10.1016/j.oceaneng.2020.107889.

[11] G. Liu, Y. Ren, J. Zhu, H. Bart-Smith, and H. Dong, "Thrust producing mechanisms in ray-inspired underwater vehicle propulsion," *Theoretical and Applied Mechanics Letters*, vol. 5, no. 1. Elsevier Ltd, pp. 54–57, Jan. 01, 2015. doi: 10.1016/j.taml.2014.12.004.

[12] A. Meschini, A. Ridolfi, J. Gelli, M. Pagliai, and A. Rindi, "Pressure Hull Design Methods for Unmanned Underwater Vehicles," *J. Mar. Sci. Eng.*, vol. 7, no. 11, p. 382, Oct. 2019, doi: 10.3390/jmse7110382.

[13] E. Simetti, F. Wanderlingh, S. Torelli, M. Bibuli, A. Odetti, G. Bruzzone, D. L. Rizzini, J. Aleotti, G. Palli, L. Moriello, and U. Scarcia, "Autonomous Underwater Intervention: Experimental Results of the MARIS Project," *IEEE J. Ocean. Eng.*, vol. 43, no. 3, pp. 620–639, Jul. 2018, doi: 10.1109/JOE.2017.2733878.

[14] D. Lodi Rizzini, F. Kallasi, J. Aleotti, F. Oleari, and S. Caselli, "Integration of a stereo vision system into an autonomous underwater vehicle for pipe manipulation tasks," *Comput. Electr. Eng.*, vol. 58, pp. 560–571, Feb. 2017, doi: 10.1016/j.compeleceng.2016.08.023.

[15] "Marin Develops Modular Autonomous Underwater Vehicle | SWZ|Maritime." https://www.swzmaritime.nl/news/2019/09/25/marin-develops-modular-autonomous-underwater-vehicle/?gdpr=accept (accessed Jan. 25, 2021).

[16] "Cybernetyczna foka lustruje dno." http://www.polska-zbrojna.pl/home/articleshow/27125?t=Cybernetyczna-foka-lustruje-dno (accessed Jan. 25, 2021).

[17] "University of Virginia MantaBot - YouTube." https://www.youtube.com/watch?v=fhgtdeIH89o (accessed Jan. 25, 2021).

[18] "A robot to find undersea carbon dioxide." http://www.isme.unige.it/news/38-a-robot-to-find-carbon-dioxide-in-the-sea (accessed Jan. 25, 2021).

[19] B. Norman, "Principles of GNSS, Inertial, and Multisensor Integrated Navigation Systems – Second Edition Paul D. Groves Artech House, 2013, 776 pp ISBN-13: 978-1-60807-005-3," *J. Navig.*, vol. 67, pp. 191–192, Jan. 2013, doi: 10.1017/S0373463313000672.

[20] J. Melo and A. Matos, "Survey on advances on terrain based navigation for autonomous underwater vehicles," *Ocean Engineering*, vol. 139. Elsevier Ltd, pp. 250–264, 2017. doi: 10.1016/j.oceaneng.2017.04.047.

[21] X. Mu, B. He, S. Wu, X. Zhang, Y. Song, and T. Yan, "A practical INS/GPS/DVL/PS integrated navigation algorithm and its application on Autonomous Underwater Vehicle," *Appl. Ocean Res.*, p. 102441, Dec. 2020, doi: 10.1016/j.apor.2020.102441.

[22] D. Sun, J. Gu, Y. Han, and J. Zhang, “Inverted ultra-short baseline signal design for multi-AUV navigation,” *Appl. Acoust.*, vol. 150, pp. 5–13, Jul. 2019, doi: 10.1016/j.apacoust.2019.01.033.

[23] H. Liu, Z. Wang, R. Shan, K. He, and S. Zhao, “Research into the integrated navigation of a deep-sea towed vehicle with USBL/DVL and pressure gauge,” *Appl. Acoust.*, vol. 159, p. 107052, Feb. 2020, doi: 10.1016/j.apacoust.2019.107052.

[24] E. G. Font, F. Bonin-Font, P. L. Negre, M. Massot, and G. Oliver, “USBL Integration and Assessment in a Multisensor Navigation Approach for AUVs,” *IFAC-PapersOnLine*, vol. 50, no. 1, pp. 7905–7910, Jul. 2017, doi: 10.1016/j.ifacol.2017.08.754.

[25] R. D. Christ and R. Wernli, “The ROV Manual: A User Guide for Remotely Operated Vehicles: Second Edition,” *ROV Man. A User Guid. Remote. Oper. Veh. Second Ed.*, pp. 1–679, Jan. 2013.

[26] V. Djapic, D. Nad, F. Mandic, N. Miskovic, and A. Kenny, “Navigational Challenges in Diver-AUV interaction for underwater mapping and intervention missions,” *IFAC-PapersOnLine*, vol. 51, no. 29, pp. 366–371, Jan. 2018, doi: 10.1016/j.ifacol.2018.09.496.

[27] K. M. Lankowicz, H. Bi, D. Liang, and C. Fan, “Sonar imaging surveys fill data gaps in forage fish populations in shallow estuarine tributaries,” *Fish. Res.*, vol. 226, Jun. 2020, doi: 10.1016/j.fishres.2020.105520.

[28] B. Chen, Y. Yang, J. Zhou, Y. Zhuang, and M. McFarland, “Damage detection of underwater foundation of a Chinese ancient stone arch bridge via sonar-based techniques,” *Meas. J. Int. Meas. Confed.*, vol. 169, pp. 263–2241, Feb. 2021, doi: 10.1016/j.measurement.2020.108283.

[29] T. Pillay, H. C. Cawthra, and A. T. Lombard, “Characterisation of seafloor substrate using advanced processing of multibeam bathymetry, backscatter, and sidescan sonar in Table Bay, South Africa,” *Mar. Geol.*, vol. 429, p. 106332, Nov. 2020, doi: 10.1016/j.margeo.2020.106332.

[30] B. Embley and B. Chadwick, “NOAA Ocean Explorer: Submarine Ring of Fire 2004.” https://oceanexplorer.noaa.gov/explorations/04fire/background/mapping/mapping.html (accessed Jan. 16, 2021).

[31] A. M. Pinto and A. C. Matos, “MARESye: A hybrid imaging system for underwater robotic applications,” *Inf. Fusion*, vol. 55, pp. 16–29, Mar. 2020, doi: 10.1016/j.inffus.2019.07.014.

[32] F. Bruno, G. Bianco, M. Muzzupappa, S. Barone, and A. V. Razionale, “Experimentation of structured light and stereo vision for underwater 3D reconstruction,” *ISPRS J. Photogramm. Remote Sens.*, vol. 66, no. 4, pp. 508–518, Jul. 2011, doi: 10.1016/j.isprsjprs.2011.02.009.

[33] A. Sarafraz and B. K. Haus, “A structured light method for underwater surface

reconstruction," *ISPRS J. Photogramm. Remote Sens.*, vol. 114, pp. 40–52, Apr. 2016, doi: 10.1016/j.isprsjprs.2016.01.014.

[34] X. Xu, R. Che, R. Nian, B. He, M. Chen, and A. Lendasse, "Underwater 3D object reconstruction with multiple views in video stream via structure from motion," in *OCEANS 2016 - Shanghai*, Jun. 2016, pp. 1–5. doi: 10.1109/OCEANSAP.2016.7485694.

[35] M. Jeon, Y. Lee, Y. S. Shin, H. Jang, and A. Kim, "Underwater Object Detection and Pose Estimation using Deep Learning," in *IFAC-PapersOnLine*, Jan. 2019, vol. 52, no. 21, pp. 78–81. doi: 10.1016/j.ifacol.2019.12.286.

[36] F. Bonin-Font, A. Burguera, and G. Oliver, "Imaging systems for advanced underwater vehicles," *J. Marit. Res.*, vol. 8, pp. 65–86, Sep. 2011.

[37] M. Prazeres and W. Renema, "Evolutionary significance of the microbial assemblages of large benthic Foraminifera," *Biol. Rev.*, vol. 94, no. 3, pp. 828–848, Jun. 2019, doi: 10.1111/brv.12482.

[38] M. Castillón, A. Palomer, J. Forest, and P. Ridao, "State of the art of underwater active optical 3D scanners," *Sensors (Switzerland)*, vol. 19, no. 23. MDPI AG, Dec. 01, 2019. doi: 10.3390/s19235161.

[39] S. Sivčev, J. Coleman, E. Omerdić, G. Dooly, and D. Toal, "Underwater manipulators: A review," *Ocean Engineering*, vol. 163. Elsevier Ltd, pp. 431–450, Sep. 01, 2018. doi: 10.1016/j.oceaneng.2018.06.018.

[40] M. Imran, D. Shi, L. Tong, H. M. Waqas, and M. Uddin, "Design optimization of egg-shaped composite submersible pressure hull for minimum buoyancy factor," *Def. Technol.*, Nov. 2020, doi: 10.1016/j.dt.2020.11.002.

[41] Y. H. Kim, Y. D. Jo, S. Y. Bae, and S. J. Sin, "Material design of Al/CFRP hybrid composites for the hull of autonomous underwater vehicle," in *OCEANS'10 IEEE Sydney, OCEANSSYD 2010*, May 2010, pp. 1–5. doi: 10.1109/OCEANSSYD.2010.5603587.

[42] R. Salazar, A. Campos, V. Fuentes, and A. Abdelkefi, "A review on the modeling, materials, and actuators of aquatic unmanned vehicles," *Ocean Engineering*, vol. 172. Elsevier Ltd, pp. 257–285, Jan. 15, 2019. doi: 10.1016/j.oceaneng.2018.11.047.

[43] L. C. Ignacio, R. R. Victor, D. R. R. Francisco, and A. Pascoal, "Optimized design of an autonomous underwater vehicle, for exploration in the Caribbean Sea," *Ocean Eng.*, vol. 187, p. 106184, Sep. 2019, doi: 10.1016/j.oceaneng.2019.106184.

[44] T. Gao, Y. Wang, Y. Pang, and J. Cao, "Hull shape optimization for autonomous underwater vehicles using CFD," *Eng. Appl. Comput. Fluid Mech.*, vol. 10, no. 1, pp. 599–607, Jan. 2016, doi: 10.1080/19942060.2016.1224735.

[45] A. Alvarez, V. Bertram, and L. Gualdesi, "Hull hydrodynamic optimization of

autonomous underwater vehicles operating at snorkeling depth," 2008, doi: 10.1016/j.oceaneng.2008.08.006.

[46] Y. Zhu, W. Liang, X. Zhao, X. Wang, and J. Xia, "Strength and stability of spherical pressure hulls with different viewport structures," *Int. J. Press. Vessel. Pip.*, vol. 176, Sep. 2019, doi: 10.1016/j.ijpvp.2019.103951.

[47] J. Gelli, A. Meschini, N. Monni, M. Pagliai, A. Ridolfi, L. Marini, and B. Allotta, "Development and Design of a Compact Autonomous Underwater Vehicle: Zeno AUV," *IFAC-PapersOnLine*, vol. 51, no. 29, pp. 20–25, Jan. 2018, doi: 10.1016/j.ifacol.2018.09.463.

[48] H. K. Jeong and P. Henry, "Optimal Design of Deep-Sea Pressure Hulls using CAE tools," *J. Comput. Struct. Eng. Inst. Korea*, vol. 25, no. 6, pp. 477–485, Dec. 2012, doi: 10.7734/coseik.2012.25.6.477.

[49] S. Y. Yoo, B. H. Jun, H. Shim, and P. M. Lee, "Design and analysis of carbon fiber reinforced plastic body frame for multi-legged subsea walking robot, Crabster," *Ocean Eng.*, vol. 102, pp. 78–86, Apr. 2015, doi: 10.1016/j.oceaneng.2015.04.024.

[50] D. Sathianarayanan, S. B. Pranesh, T. Chowdhury, E. Chandrasekar, M. Murugesan, M. Radhakrishnan, A. N. Subramanian, G. A. Ramadass, and M. A. Atmanand, "Mechanical engineering challenges in the development of deepwater ROV (ROSUB 6000)," in *2017 IEEE OES International Symposium on Underwater Technology, UT 2017*, Mar. 2017, pp. 1–6. doi: 10.1109/UT.2017.7890286.

[51] S. Garcia and C. T. Trinh, "Modular design: Implementing proven engineering principles in biotechnology," *Biotechnology Advances*, vol. 37, no. 7. Elsevier Inc., p. 107403, Nov. 15, 2019. doi: 10.1016/j.biotechadv.2019.06.002.

[52] B. Allotta *et al.*, "Design of a modular Autonomous Underwater Vehicle for archaeological investigations," in *MTS/IEEE OCEANS 2015 - Genova: Discovering Sustainable Ocean Energy for a New World*, Sep. 2015, pp. 1–5. doi: 10.1109/OCEANS-Genova.2015.7271398.

[53] "Bluefin-21 Unmanned Underwater Vehicle (UUV) - General Dynamics Mission Systems." https://gdmissionsystems.com/products/underwater-vehicles/bluefin-21-autonomous-underwater-vehicle (accessed Jan. 14, 2021).

[54] "Autonomous Underwater Vehicles (AUVs) - Teledyne Marine." http://www.teledynemarine.com/autonomous-underwater-vehicles-auvs (accessed Jan. 29, 2021).

[55] "Underwater Systems | Security | Saab." https://www.saab.com/products/security/underwater-systems (accessed Jan. 29, 2021).

[56] "AUV Solutions | Eca Group." https://www.ecagroup.com/en/find-your-eca-solutions/auv?page=1 (accessed Jan. 29, 2021).

[57] “Blue Robotics - Underwater ROVs, Thrusters, Sonars, and Cameras.” https://bluerobotics.com/ (accessed Jan. 29, 2021).

[58] “The MacArtney Group is a global supplier of underwater technology.” https://www.macartney.com/ (accessed Jan. 29, 2021).

[59] N. Iheanachor, I. O. Umukoro, and O. David-West, “The role of product development practices on new product performance: Evidence from Nigeria’s financial services providers,” *Technol. Forecast. Soc. Change*, p. 120470, Dec. 2020, doi: 10.1016/j.techfore.2020.120470.

[60] K. T. Ulrich and S. D. Eppinger, *Product design and development*. 2016.

[61] R. Kumar, Jagadish, and A. Ray, “Selection of Material for Optimal Design Using Multi-criteria Decision Making,” *Procedia Mater. Sci.*, vol. 6, pp. 590–596, Jan. 2014, doi: 10.1016/j.mspro.2014.07.073.

[62] I. Emovon and O. S. Oghenenyerovwho, “Application of MCDM method in material selection for optimal design: A review,” *Results Mater.*, vol. 7, p. 100115, Sep. 2020, doi: 10.1016/j.rinma.2020.100115.

[63] M. F. Ashby, *Materials selection in mechanical design*. 2017.

[64] A. Rashedi, I. Sridhar, and K. J. Tseng, “Multi-objective material selection for wind turbine blade and tower: Ashby’s approach,” *Mater. Des.*, vol. 37, pp. 521–532, May 2012, doi: 10.1016/j.matdes.2011.12.048.

[65] Z. Mehmood, I. Haneef, and F. Udrea, “Material selection for Micro-Electro-Mechanical-Systems (MEMS) using Ashby’s approach,” *Mater. Des.*, vol. 157, pp. 412–430, Nov. 2018, doi: 10.1016/j.matdes.2018.07.058.

[66] A. Chauhan and R. Vaish, “Hard coating material selection using multi-criteria decision making,” *Mater. Des.*, vol. 44, pp. 240–245, Feb. 2013, doi: 10.1016/j.matdes.2012.08.003.

[67] M. C. L. De Oliveira, G. Ett, and R. A. Antunes, “Materials selection for bipolar plates for polymer electrolyte membrane fuel cells using the Ashby approach,” *Journal of Power Sources*, vol. 206. Elsevier, pp. 3–13, May 15, 2012. doi: 10.1016/j.jpowsour.2012.01.104.

[68] W. Franco, F. Barbera, L. Bartolucci, T. Felizia, and F. Focanti, “Developing intermediate machines for high-land agriculture,” *Dev. Eng.*, vol. 5, p. 100050, Jan. 2020, doi: 10.1016/j.deveng.2020.100050.

[69] J. Butchers, J. Cox, S. Williamson, J. Booker, and B. Gautam, “Design for localisation: A case study in the development and implementation of a low head propeller turbine in Nepal,” *Dev. Eng.*, vol. 5, p. 100051, Jan. 2020, doi: 10.1016/j.deveng.2020.100051.

[70] W. E. (East C. U. Howard and J. C. (Milwaukee S. of E. Musto, *Introduction to Solid Modeling Using Solidworks 2018*. New York: McGraw-Hill Education, 2018.

[71] C. González-Lluch, P. Company, M. Contero, J. D. Camba, and R. Plumed, “A survey on 3D CAD model quality assurance and testing tools,” *CAD Comput. Aided Des.*, vol. 83, pp. 64–79, Feb. 2017, doi: 10.1016/j.cad.2016.10.003.

[72] I. Stroud and H. Nagy, *Solid Modelling and CAD Systems*. Heidelberg: Springer, 2011. doi: 10.1007/978-0-85729-259-9.

[73] “CAD/CAM | Computer-Aided Design And Manufacturing | Autodesk.” https://www.autodesk.com/solutions/cad-cam (accessed Jan. 20, 2021).

[74] P. N. Rao, *CAD/CAM: Principles and Applications*. McGraw-Hill Education (India) Pvt Limited, 2004. [Online]. Available: https://books.google.dj/books?id=QaY_sQC4-5YC

[75] “Solutions | SOLIDWORKS.” https://www.solidworks.com/solutions (accessed Jan. 20, 2021).

[76] “Creo CAD Software: Enable the Latest in Design | PTC.” https://www.ptc.com/en/products/creo (accessed Jan. 20, 2021).

[77] “CATIA^{TM} V5 Portfolio - Dassault Systèmes® 3D Software.” https://www.3ds.com/products-services/catia/products/v5/portfolio/?woc=%7B%22category%22%3A%5B%22category%2Fchampions%22%5D%7D&wockw=card_content_cta_1_url%3A%22https%3A%2F%2Fblogs.3ds.com%2Fcatia%2F%22 (accessed Jan. 20, 2021).

[78] D. Rana, K. Ramasamy, M. Leena, R. Pasricha, G. Manivasagam, and M. Ramalingam, “Surface Functionalization of Biomaterials,” in *Biology and Engineering of Stem Cell Niches*, Elsevier Inc., 2017, pp. 331–343. doi: 10.1016/B978-0-12-802734-9.00021-4.

[79] A. Nazir, A. Azhar, U. Nazir, Y. F. Liu, W. S. Qureshi, J. E. Chen, and E. Alanazi, “The rise of 3D Printing entangled with smart computer aided design during COVID-19 era,” *J. Manuf. Syst.*, Oct. 2020, doi: 10.1016/j.jmsy.2020.10.009.

[80] M. İ. Sarı, İ. Şahin, H. Gökçe, and Ç. Öksüz, “Ring orthosis design and production by rapid prototyping approach,” *J. Hand Ther.*, vol. 33, no. 2, pp. 170–173, Apr. 2020, doi: 10.1016/j.jht.2019.02.003.

[81] U. M. Dilberoglu, B. Gharehpapagh, U. Yaman, and M. Dolen, “The Role of Additive Manufacturing in the Era of Industry 4.0,” *Procedia Manuf.*, vol. 11, pp. 545–554, 2017, doi: 10.1016/j.promfg.2017.07.148.

[82] B. Esmaeilian, S. Behdad, and B. Wang, “The evolution and future of manufacturing: A review,” *Journal of Manufacturing Systems*, vol. 39. Elsevier B.V., pp. 79–100, Apr. 01, 2016. doi: 10.1016/j.jmsy.2016.03.001.

[83] N. K. Maurya, V. Rastogi, and P. Singh, “An overview of mechanical properties and form error for rapid prototyping,” *CIRP Journal of Manufacturing Science and Technology*, vol. 29. Elsevier Ltd, pp. 53–70, May 01, 2020. doi:

10.1016/j.cirpj.2020.02.003.

[84] N. Anwer and L. Mathieu, “From reverse engineering to shape engineering in mechanical design,” *CIRP Ann. - Manuf. Technol.*, vol. 65, no. 1, pp. 165–168, Jan. 2016, doi: 10.1016/j.cirp.2016.04.052.

[85] L. Li, C. Li, Y. Tang, and Y. Du, “An integrated approach of reverse engineering aided remanufacturing process for worn components,” *Robot. Comput. Integr. Manuf.*, vol. 48, pp. 39–50, Dec. 2017, doi: 10.1016/j.rcim.2017.02.004.

[86] S. Zivkovic, L. Cerce, J. Kostic, V. Majstorovic, and D. Kramar, “Reverse engineering of turbine blades Kaplan’s type for small hydroelectric power station,” in *Procedia CIRP*, Jan. 2018, vol. 75, pp. 379–384. doi: 10.1016/j.procir.2018.04.037.

[87] B. Engel and S. S. H. Al-Maeeni, “An integrated reverse engineering and failure analysis approach for recovery of mechanical shafts,” in *Procedia CIRP*, Jan. 2019, vol. 81, pp. 1083–1088. doi: 10.1016/j.procir.2019.03.257.

[88] U. Dombrowski, S. Schmidt, and K. Schmidtchen, “Analysis and integration of design for X approaches in lean design as basis for a lifecycle optimized product design,” in *Procedia CIRP*, Jan. 2014, vol. 15, pp. 385–390. doi: 10.1016/j.procir.2014.06.023.

[89] G. C. Mantese, M. J. Bianchi, and D. C. Amaral, “The industrial symbiosis in the product development: An approach through the DFIS,” in *Procedia Manufacturing*, 2018, vol. 21, pp. 862–869. doi: 10.1016/j.promfg.2018.02.194.

[90] M. Auflem, J. F. Erichsen, and M. Steinert, “Exemplifying prototype-driven development through concepts for medical training simulators,” in *Procedia CIRP*, Jan. 2019, vol. 84, pp. 572–578. doi: 10.1016/j.procir.2019.04.202.

[91] C. Ji, J. Hu, B. Wang, Y. Zou, Y. Yang, and Y. Sun, “Mechanical behavior prediction of CF/PEEK-titanium hybrid laminates considering temperature effect by artificial neural network,” *Compos. Struct.*, p. 113367, Nov. 2020, doi: 10.1016/j.compstruct.2020.113367.

[92] A. J. Baptista, D. Peixoto, A. D. Ferreira, and J. P. Pereira, “Lean Design-for-X Methodology: Integrating Modular Design, Structural Optimization and Ecodesign in a Machine Tool Case Study,” *Procedia CIRP*, vol. 69, pp. 722–727, 2018, doi: https://doi.org/10.1016/j.procir.2017.12.003.

[93] R. Korsmik, I. Tsybulskiy, A. Rodionov, O. Klimova-Korsmik, M. Gogolukhina, S. Ivanov, G. Zadykyan, and R. Mendagaliev, “The approaches to design and manufacturing of large-sized marine machinery parts by direct laser deposition,” in *Procedia CIRP*, Jan. 2020, vol. 94, pp. 298–303. doi: 10.1016/j.procir.2020.09.056.

[94] A. L. Saldaña-Robles, A. Bustos-Gaytán, J. A. Diosdado-De la Peña, A. Saldaña-Robles, V. Alcántar-Camarena, A. Balvantín-García, and N. Saldaña-Robles, “Structural design of an agricultural backhoe using TA, FEA, RSM and ANN,”

Comput. Electron. Agric., vol. 172, p. 105278, May 2020, doi: 10.1016/J.COMPAG.2020.105278.

[95] S. N. Patnaik and D. A. Hopkins, “Strength of Materials A New Unified Theory for the 21st Century,” S. N. Patnaik and D. A. B. T.-S. of M. Hopkins, Eds. Burlington: Butterworth-Heinemann, 2004, pp. 1–53. doi: https://doi.org/10.1016/B978-075067402-7/50001-9.

[96] M. H. Sadd, *Elasticity : theory, applications, and numerics*. 2014.

[97] S. S. Rao, *The Finite Element Method in Engineering: Fifth Edition*. Elsevier Inc., 2010. doi: 10.1016/C2009-0-04807-7.

[98] “Introduction to Femap | Structural Design and Analysis.” https://structures.aero/fea-using-femap/ (accessed Jan. 26, 2021).

[99] F. Ahmadi, A. Rahbar Ranji, and H. Nowruzi, “Ultimate strength prediction of corroded plates with center-longitudinal crack using FEM and ANN,” *Ocean Eng.*, vol. 206, p. 107281, Jun. 2020, doi: 10.1016/j.oceaneng.2020.107281.

[100] A. Muhammad, M. A. H. Ali, and I. H. Shanono, “ANSYS - A bibliometric study,” in *Materials Today: Proceedings*, Jan. 2019, vol. 26, pp. 1005–1009. doi: 10.1016/j.matpr.2020.01.192.

[101] “About Ansys.” https://www.ansys.com/about-ansys (accessed Jan. 28, 2021).

[102] “Abaqus CAE - SIMULA™ by Dassault Systèmes®.” https://www.3ds.com/products-services/simulia/products/abaqus/abaquscae/ (accessed Jan. 28, 2021).

[103] “FEA Software for Performing Structural Analyses.” https://www.comsol.pt/structural-mechanics-module (accessed Jan. 28, 2021).

[104] C. Song, E. T. Ooi, and S. Natarajan, “A review of the scaled boundary finite element method for two-dimensional linear elastic fracture mechanics,” *Engineering Fracture Mechanics*, vol. 187. Elsevier Ltd, pp. 45–73, Jan. 01, 2018. doi: 10.1016/j.engfracmech.2017.10.016.

[105] S. Dölling, J. Hahn, J. Felger, S. Bremm, and W. Becker, “A scaled boundary finite element method model for interlaminar failure in composite laminates,” *Composite Structures*, vol. 241. Elsevier Ltd, p. 111865, Jun. 01, 2020. doi: 10.1016/j.compstruct.2020.111865.

[106] C. Grunwald, A. A. Khalil, B. Schaufelberger, E. M. Ricciardi, C. Pellecchia, E. De Iuliis, and W. Riedel, “Reliability of collapse simulation – Comparing finite and applied element method at different levels,” *Eng. Struct.*, vol. 176, pp. 265–278, Dec. 2018, doi: 10.1016/j.engstruct.2018.08.068.

[107] C. M. Rathnayaka Mudiyanselage, H. C. P. Karunasena, Y. T. Gu, L. Guan, and W. Senadeera, “Novel trends in numerical modelling of plant food tissues and their morphological changes during drying – A review,” *Journal of Food Engineering*,

vol. 194. Elsevier Ltd, pp. 24–39, Feb. 01, 2017. doi: 10.1016/j.jfoodeng.2016.09.002.

[108] A. Synek, S. F. Baumbach, and D. H. Pahr, “Towards optimization of volar plate fixations of distal radius fractures: Using finite element analyses to reduce the number of screws,” *Clin. Biomech.*, vol. 82, p. 105272, Jan. 2021, doi: 10.1016/j.clinbiomech.2021.105272.

[109] T. Tuswan, K. Abdullah, A. Zubaydi, and A. Budipriyanto, “Finite-element analysis for structural strength assessment of marine sandwich material on ship side-shell structure,” in *Materials Today: Proceedings*, Jan. 2019, vol. 13, pp. 109–114. doi: 10.1016/j.matpr.2019.03.197.

[110] W. Deng, X. Wang, X. Pan, S. Zhang, J. Ding, and G. Li, “Geometry design and performance optimization of a terrestrial radioisotope thermoelectric generator based on finite element analysis,” *Ann. Nucl. Energy*, vol. 151, p. 107883, Feb. 2021, doi: 10.1016/j.anucene.2020.107883.

[111] M. Vivekanandan, R. Venkatesh, T. Sathish, S. Dinesh, M. Ravichandran, and V. Vijayan, “Pressure Vessel Design using PV-ELITE Software with Manual Calculations and Validation by FEM,” 2019. Accessed: Jan. 29, 2021. [Online]. Available: https://www.researchgate.net/publication/342889389

[112] S. Nandhakumar, S. Seenivasan, A. Mohammed Saalih, and M. Saifudheen, “Weight optimization and structural analysis of an electric bus chassis frame,” *Mater. Today Proc.*, Aug. 2020, doi: 10.1016/j.matpr.2020.07.404.

[113] “Project Atlantis – The Atlantic Testing Platform for Maritime Robotics.” https://www.atlantis-h2020.eu/ (accessed Jul. 30, 2021).

[114] D. A. Shifler, “Understanding material interactions in marine environments to promote extended structural life,” in *Corrosion Science*, Oct. 2005, vol. 47, no. 10, pp. 2335–2352. doi: 10.1016/j.corsci.2004.09.027.

[115] C. Vargel, “Chapter C.13 - Galvanic corrosion,” C. B. T.-C. of A. (Second E. Vargel, Ed. Amsterdam: Elsevier, 2020, pp. 295–315. doi: https://doi.org/10.1016/B978-0-08-099925-8.00025-9.

[116] X. Lu, D. Niyato, P. Wang, D. I. Kim, and H. Zhu, “Wireless charger networking for mobile devices: Fundamentals, standards, and applications,” *IEEE Wirel. Commun.*, vol. 22, no. 2, pp. 126–135, Apr. 2015, doi: 10.1109/MWC.2015.7096295.

[117] ERIKS, “Technical O-ring Handbook,” 2013. https://o-ring.info/en/technical-info/technical-o-ring-handbook/ (accessed May 13, 2021).

[118] M. Vallet-Regí, “Ceramics for medical applications,” *J. Chem. Soc.{,} Dalt. Trans.*, no. 2, pp. 97–108, 2001, doi: 10.1039/B007852M.

[119] E. Canepa, R. Stifanese, L. Merotto, and P. Traverso, “Corrosion behaviour of

aluminium alloys in deep-sea environment: A review and the KM3NeT test results," *Mar. Struct.*, vol. 59, pp. 271–284, May 2018, doi: 10.1016/j.marstruc.2018.02.006.

[120] S. Gupta, D. Singh, A. Yadav, S. Jain, and B. Pratap, "A comparative study of 5083 aluminium alloy and 316L stainless steel for shipbuilding material," in *Materials Today: Proceedings*, Jan. 2020, vol. 28, pp. 2358–2363. doi: 10.1016/j.matpr.2020.04.641.

[121] Y. Fu, N. Guo, L. Zhou, Q. Cheng, and J. Feng, "Underwater wire-feed laser deposition of the Ti–6Al–4V titanium alloy," *Mater. Des.*, vol. 186, p. 108284, Jan. 2020, doi: 10.1016/j.matdes.2019.108284.

[122] J. A. Wharton, R. C. Barik, G. Kear, R. J. K. Wood, K. R. Stokes, and F. C. Walsh, "The corrosion of nickel-aluminium bronze in seawater," *Corros. Sci.*, vol. 47, no. 12, pp. 3336–3367, Dec. 2005, doi: 10.1016/j.corsci.2005.05.053.

[123] "Online Materials Information Resource - MatWeb." http://www.matweb.com/ (accessed May 20, 2021).

[124] "MakeItFrom.com: Material Properties Database." https://www.makeitfrom.com/ (accessed May 20, 2021).

[125] S. Niu, H. Xu, Z. Sun, Z. Y. Shao, and L. Jian, "The state-of-the-arts of wireless electric vehicle charging via magnetic resonance: principles, standards and core technologies," *Renewable and Sustainable Energy Reviews*, vol. 114. Elsevier Ltd, p. 109302, Oct. 01, 2019. doi: 10.1016/j.rser.2019.109302.

[126] Ensinger, "Product overview machinable plastics | Ensinger." https://www.ensingerplastics.com/en/shapes/products#/?filter=N4XyAA$$ (accessed May 19, 2021).

[127] K. Pielichowska, A. Szczygielska, and E. Spasówka, "Preparation and characterization of polyoxymethylene-copolymer/hydroxyapatite nanocomposites for long-term bone implants," *Polym. Adv. Technol.*, vol. 23, no. 8, pp. 1141–1150, Aug. 2012, doi: 10.1002/pat.2012.

[128] F. Chavarria and D. R. Paul, "Comparison of nanocomposites based on nylon 6 and nylon 66," *Polymer (Guildf).*, vol. 45, no. 25, pp. 8501–8515, Nov. 2004, doi: 10.1016/j.polymer.2004.09.074.

[129] A. E. Wiacek, K. Terpiłowski, M. Jurak, and M. Worzakowska, "Effect of low-temperature plasma on chitosan-coated PEEK polymer characteristics," *Eur. Polym. J.*, vol. 78, pp. 1–13, May 2016, doi: 10.1016/j.eurpolymj.2016.02.024.

[130] H. J. Um, Y. T. Hwang, K. H. Choi, and H. S. Kim, "Effect of crystallinity on the mechanical behavior of carbon fiber reinforced polyethylene-terephthalate (CF/PET) composites considering temperature conditions," *Compos. Sci. Technol.*, vol. 207, p. 108745, May 2021, doi: 10.1016/j.compscitech.2021.108745.

[131] "Plásticos de Engenharia | Poly Lanema." https://www.polylanema.pt/pt/plasticos-de-engenharia/ (accessed May 31, 2021).

[132] J. C. Campos Rubio, T. H. Panzera, and F. Scarpa, "Machining behaviour of three high-performance engineering plastics," *Proc. Inst. Mech. Eng. Part B J. Eng. Manuf.*, vol. 229, no. 1, pp. 28–37, Jan. 2015, doi: 10.1177/0954405414525142.

[133] J. Wall, "Simulation-Driven Design of Complex Mechanical and Mechatronic Systems," 2007.

ANNEXES

6 ANNEXES

In this table are listed the material properties that were used in Table 10. The standards used to obtain these values are not specified.

	Yield Stress [MPa]	Density [g/cm^3]	Corrosion resistance [1-5]	Cost [1-5]	Thermal conductivity [W/m·k]	Young's modulus [GPa]
AW 7068-T6	683	2.85	3	3.9	190	70
AW 6061-T6	275	2.7	4	1	167	70
AW 6082-T6	260	2.7	4	1	170	70
AW 7075-T6	503	2.81	3	1.4	130	70
AISI 316L	240	8	4	2.4	15	193
Ti6 Al-4V	885	4.42	5	5	6.7	113.8
UNS C63000	470	7.58	4	3.9	37.7	115

In this table are listed the material properties that were used in Table 13 as well as the respective norms used to obtain these values.

	Yield strength [MPa] (DIN EN ISO 527-2)	Density [g/cm^3]	Young's modulus [MPa] (DIN EN ISO 527-1/-2)	Toughness [kJ/m2] (DIN EN ISO 179-1eA)	Cost [1-5]	Water Absorption [%] (DIN EN ISO 62)
POM - C	67	1.41	2800	8	1	0.1
POM - H	79	1.43	3400	15	1	0.1
PA 6	78	1.14	3500	7	1	0.6
PA 66	84	1.15	3300	5	2	0.4
PEEK	116	1.31	4200	4	4	0.03
PET	91	1.39	3500	5	2	0.03

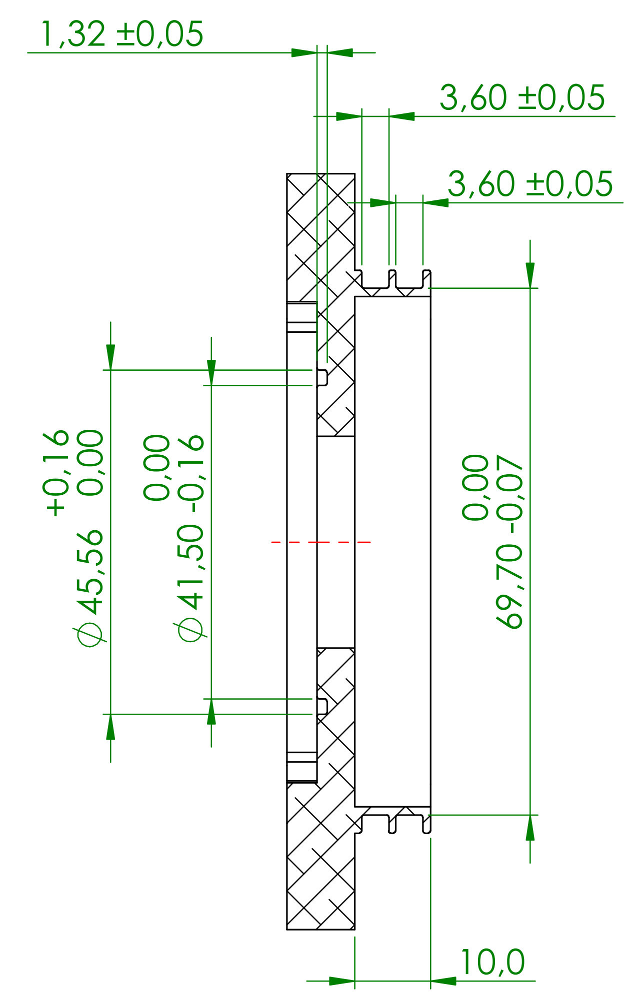

SECTION A-A

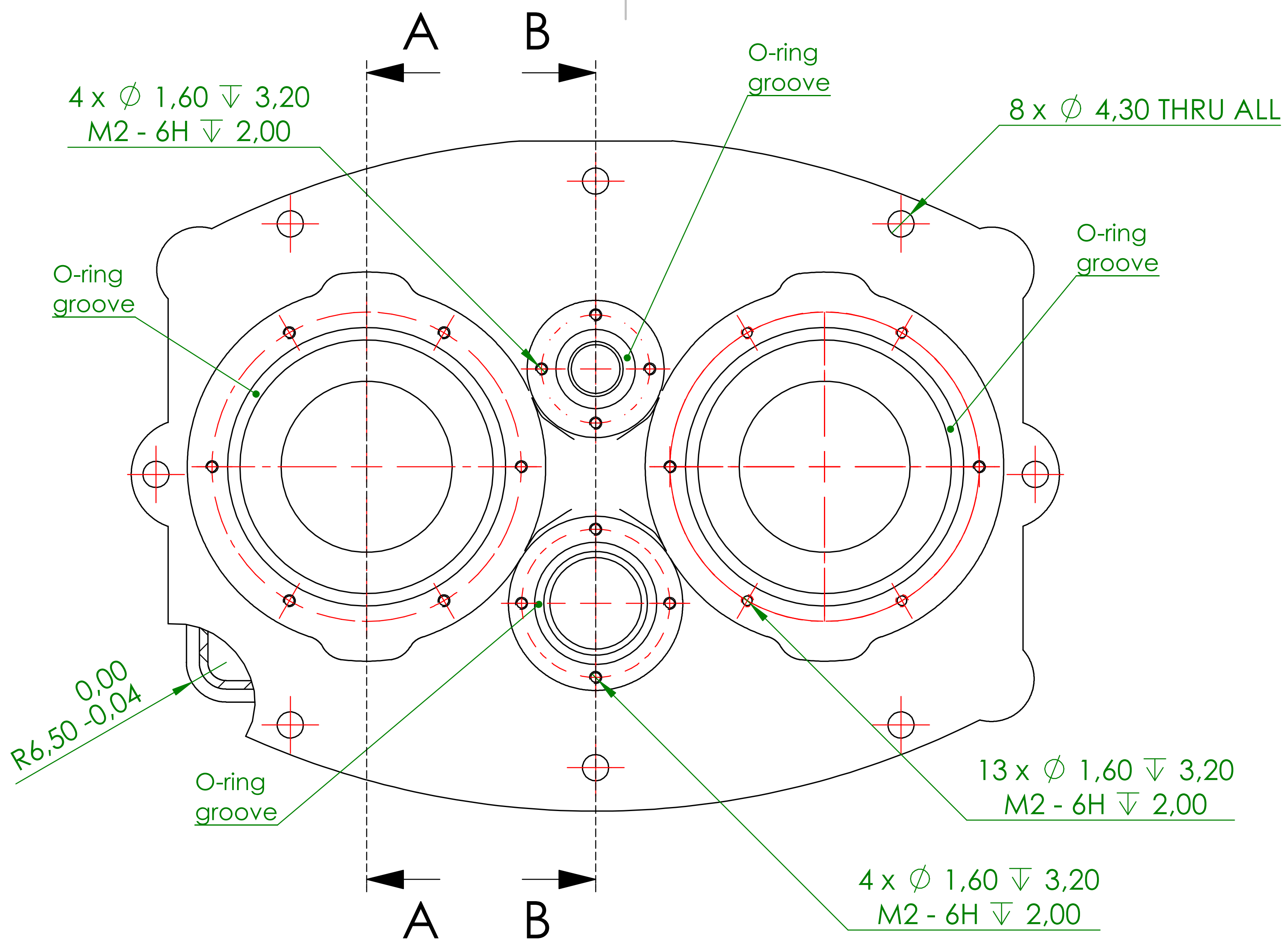

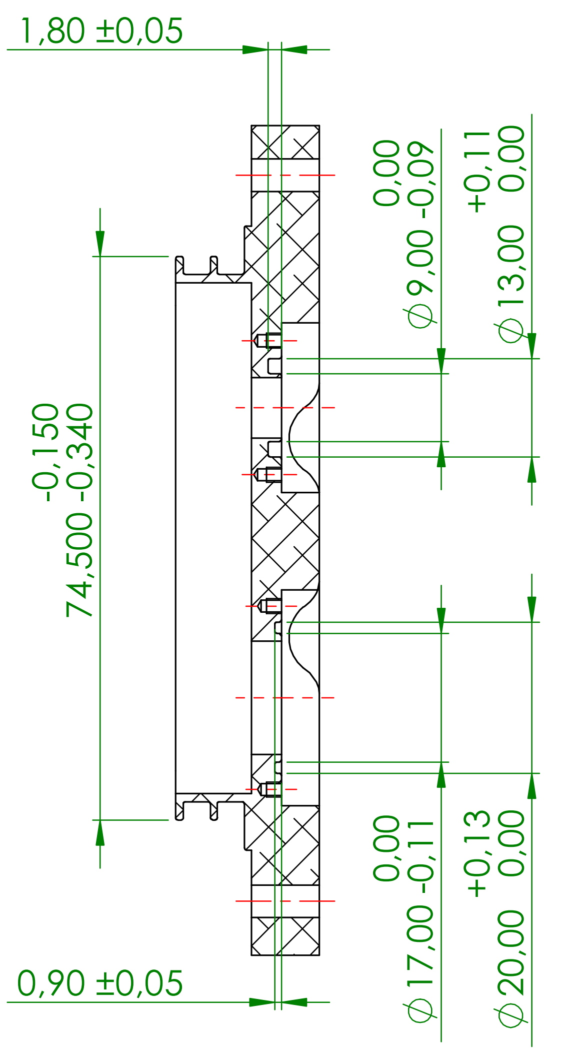

SECTION B-B

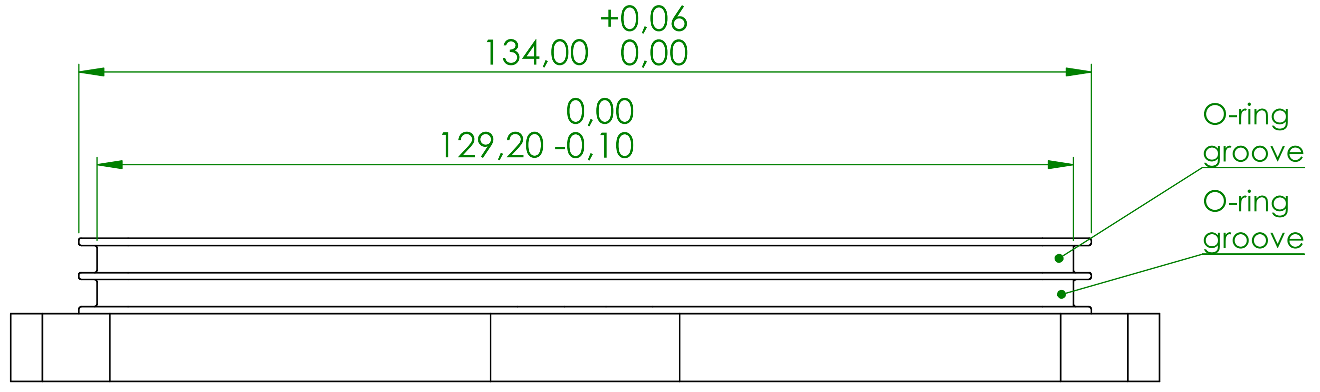

All O-Ring grooves must be filleted as follows:

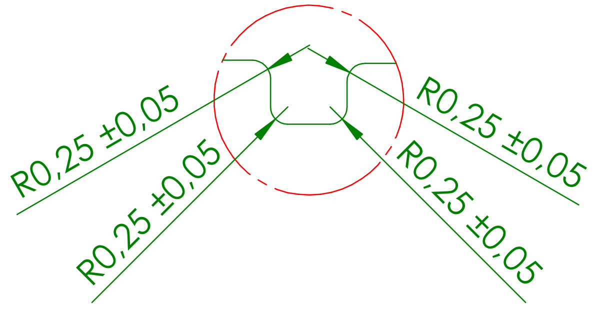

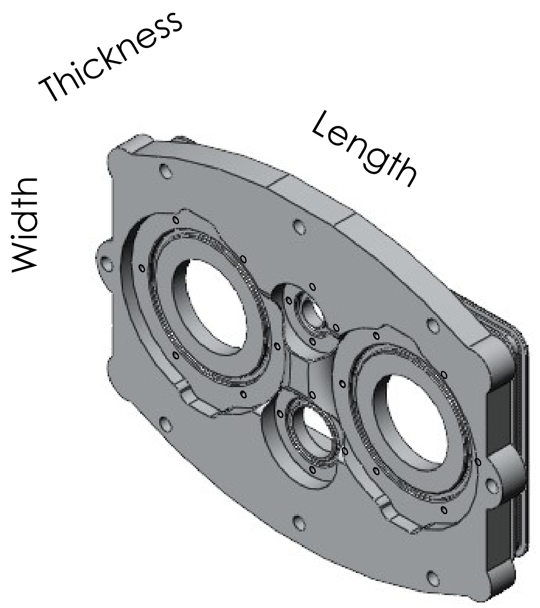

Length	152
Width	110
Thickness	19

Referring to solid model for geometry not dimensioned is permissible. All unspecified surfaces must match solid model within 0.1mm. All sharp corners are allowed up to 0.5 mm fillet

UNLESS OTHERWISE SPECIFIED:
DIMENSIONS ARE IN MILLIMETERS
SURFACE FINISH: 3.2 μm
TOLERANCES:
LINEAR: ± 0.1 mm
ANGULAR: ± 1°

Created by: Pedro Pereira

Drawing and tolerancing standard:
ISO 2768-1 | ISO 8015

INESCTEC
CRAS - Center of Robotics and Autonoous Systems

CONFIDENTIALITY NOTICE

THIS DRAWING AND INFORMATION CONTAINED HEREIN ARE THE EXCLUSIVE PROPERTY OF INESC TEC. AND SHALL BE RETURNED UPON DEMAND AND SHALL NOT BE REPRODUCED IN WHOLE OR IN PART TO ANYONE ELSE OR USED, WITHOUT THE WRITTEN CONSENT OF INESC TEC.

TITLE: IPSH

MATERIAL: Aw 6082-T6

DWG NAME: IPSH Lid

A3

WEIGHT: 275 g

SCALE:1:1

SHEET 1 OF 1

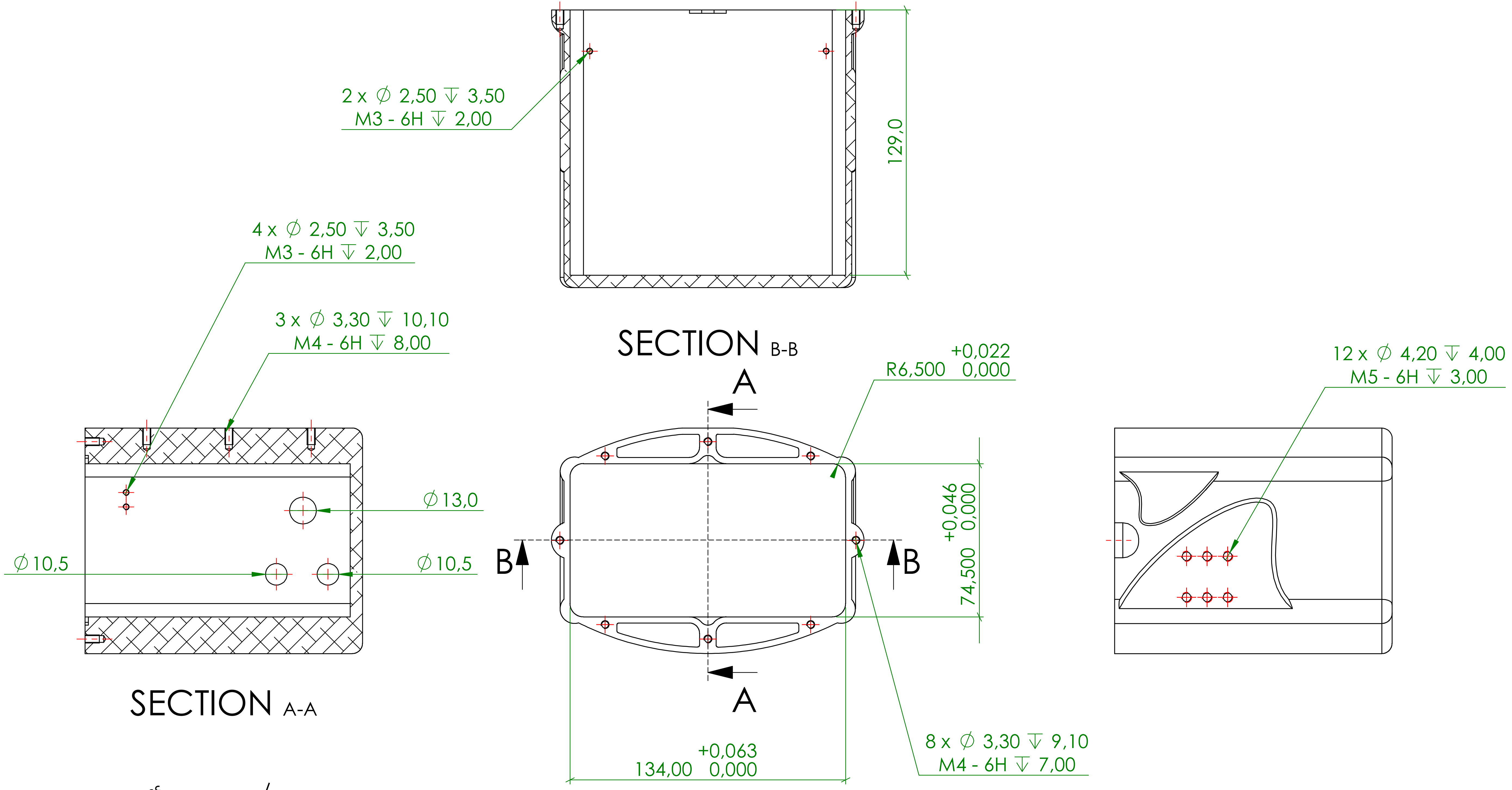

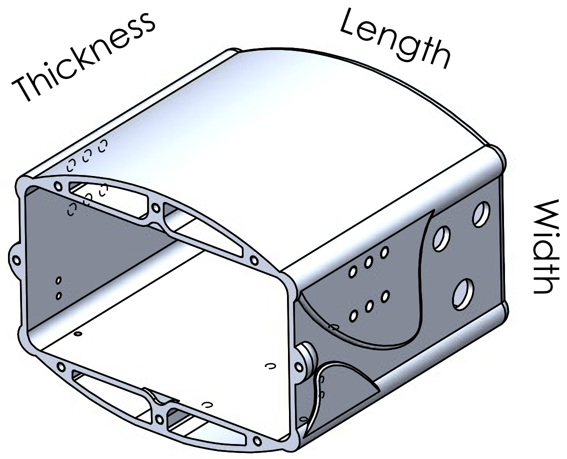

Length	152
Width	110
Thickness	135

Referring to solid model for geometry not dimensioned is permissible. All unspecified surfaces must match solid model within 0.1mm. All sharp corners are allowed up to 1 mm fillet

UNLESS OTHERWISE SPECIFIED:
DIMENSIONS ARE IN MILLIMETERS
SURFACE FINISH: 3.2 µm
TOLERANCES:
LINEAR: ± 0.1 mm
ANGULAR: ± 1°

Created by: Pedro Pereira

Drawing and tolerancing standard:
ISO 2768-mK | ISO 8015

INESCTEC
CRAS - Center of Robotics and Autonomous Systems

CONFIDENTIALITY NOTICE

TITLE:
IPSH

MATERIAL:
Aw 6082-T6

DWG NAME
IPSH BOX

A3

WEIGHT: 1088 g

SCALE:1:2

SHEET 1 OF 1

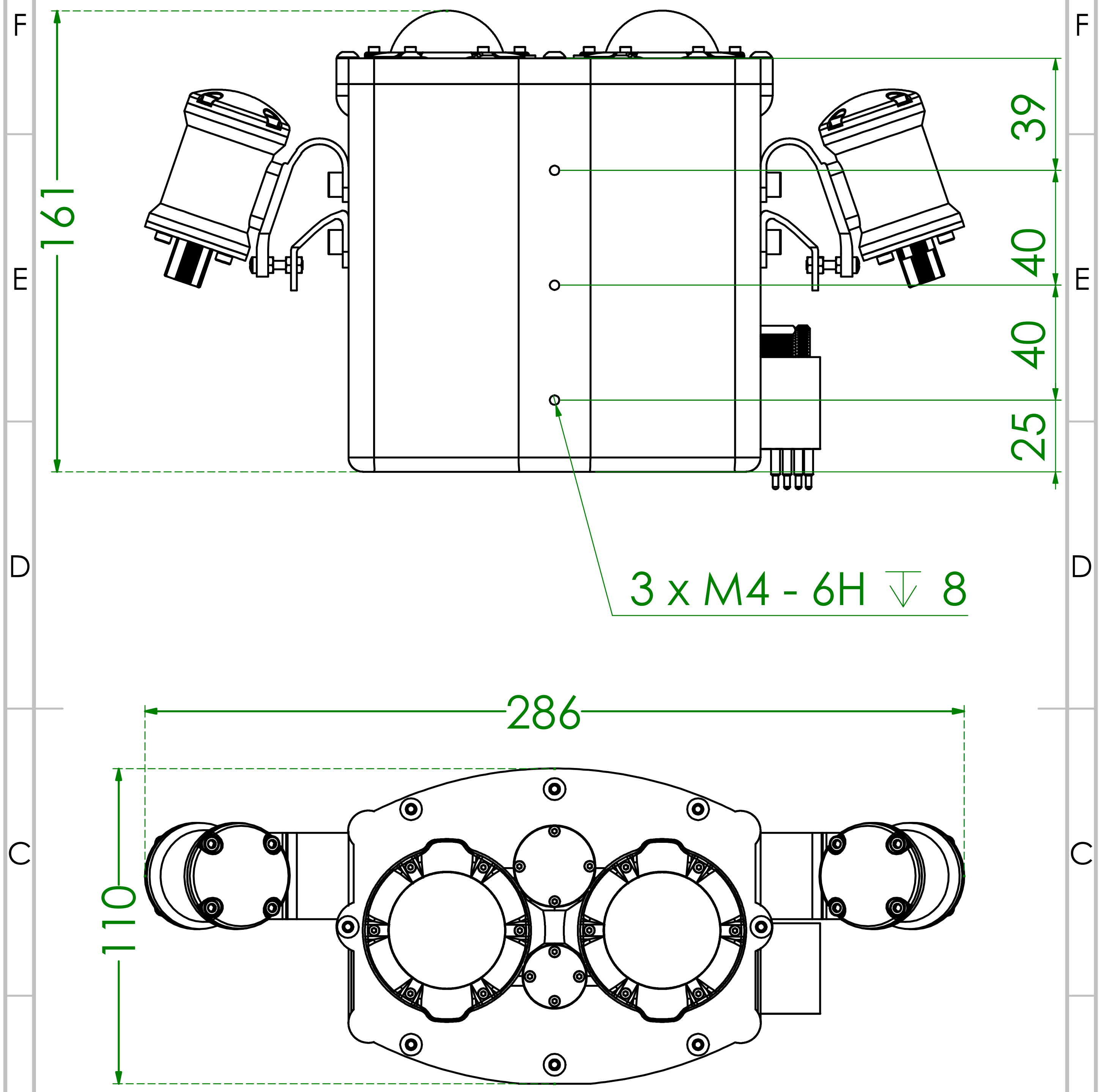

UNLESS OTHERWISE SPECIFIED:
DIMENSIONS ARE IN MILLIMETERS
SURFACE FINISH:
TOLERANCES:
LINEAR:
ANGULAR:

Drawn by: Pedro Pereira
Contact:

- pedro.n.almeida@inesctec.pt
- +351 916970655

INESCTEC
CRAS - Center of Robotics and Autonoous Systems

CONFIDENTIALITY NOTICE

THIS DRAWING AND INFORMATION CONTAINED HEREIN ARE THE EXCLUSIVE PROPERTY OF INESC TEC. AND SHALL BE RETURNED UPON DEMAND AND SHALL NOT BE REPRODUCED IN WHOLE OR IN PART TO ANYONE ELSE OR USED, WITHOUT THE WRITTEN CONSENT OF INESC TEC.

TITLE:
MARESye

DWG NAME
General dimensions

A4

WEIGHT: 2282 g
SCALE:1:2
SHEET 1 OF 1

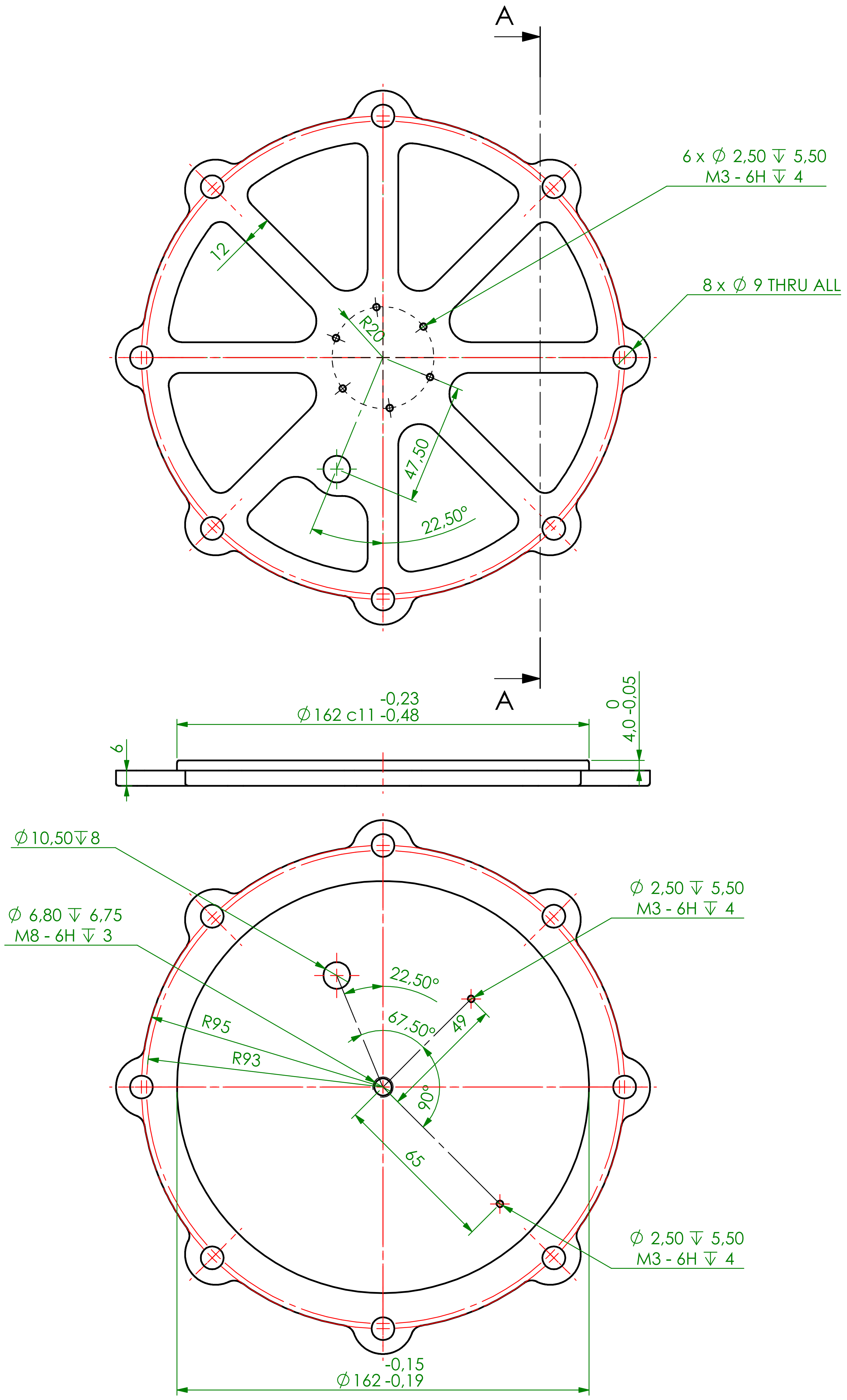

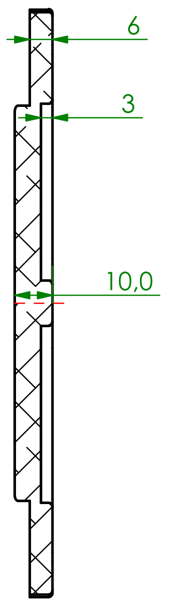

SECTION A-A

General Dimensions:

⌀ 210 mm
Height 10 mm

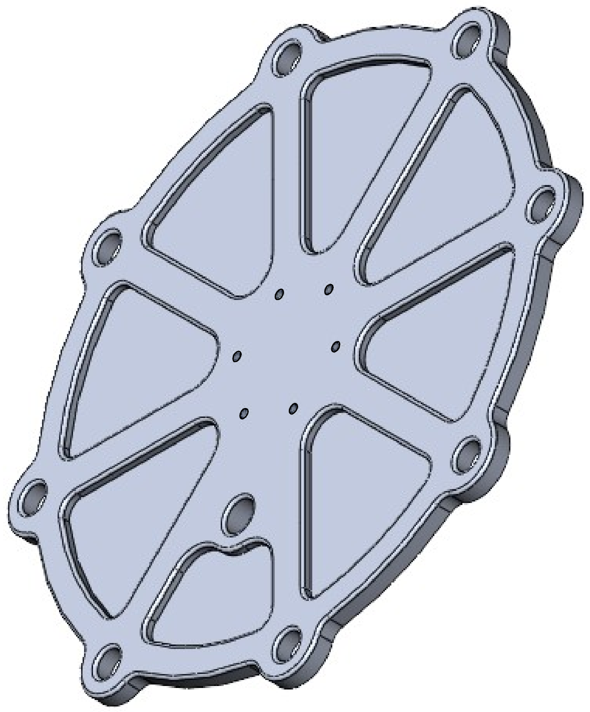

Refering to solid model for geometry not dimensioned is permissible.
All unspecified surfaces must match solid model within 0.5 mm.
Unless specified all corners are allowed a 1mm fillet

UNLESS OTHERWISE SPECIFIED:
DIMENSIONS ARE IN MILLIMETERS
SURFACE FINISH: 3.2 μm
TOLERANCES:
LINEAR: ± 0.5 mm
ANGULAR: ± 1°

Created by: Pedro Pereira

Drawing and tolerancing standard:
ISO 2768-mK | ISO 8015

INESCTEC
CRAS - Center of Robotics and Autonoous Systems

CONFIDENTIALITY NOTICE

THIS DRAWING AND INFORMATION CONTAINED HEREIN ARE THE EXCLUSIVE PROPERTY OF INESC TEC. AND SHALL BE RETURNED UPON DEMAND AND SHALL NOT BE REPRODUCED IN WHOLE OR IN PART TO ANYONE ELSE OR USED, WITHOUT THE WRITTEN CONSENT OF INESC TEC.

TITLE: WCH

MATERIAL: Aw 6061-T6

DWG NAME WCH Lid

A3

WEIGHT: 580 g

SCALE:1:2

SHEET 1 OF 1

Refering to solid model for geometry not dimensioned is permissible.
All unspecified surfaces must match solid model within 0.5 mm.
Unless specified all corners are allowed a 1mm fillet

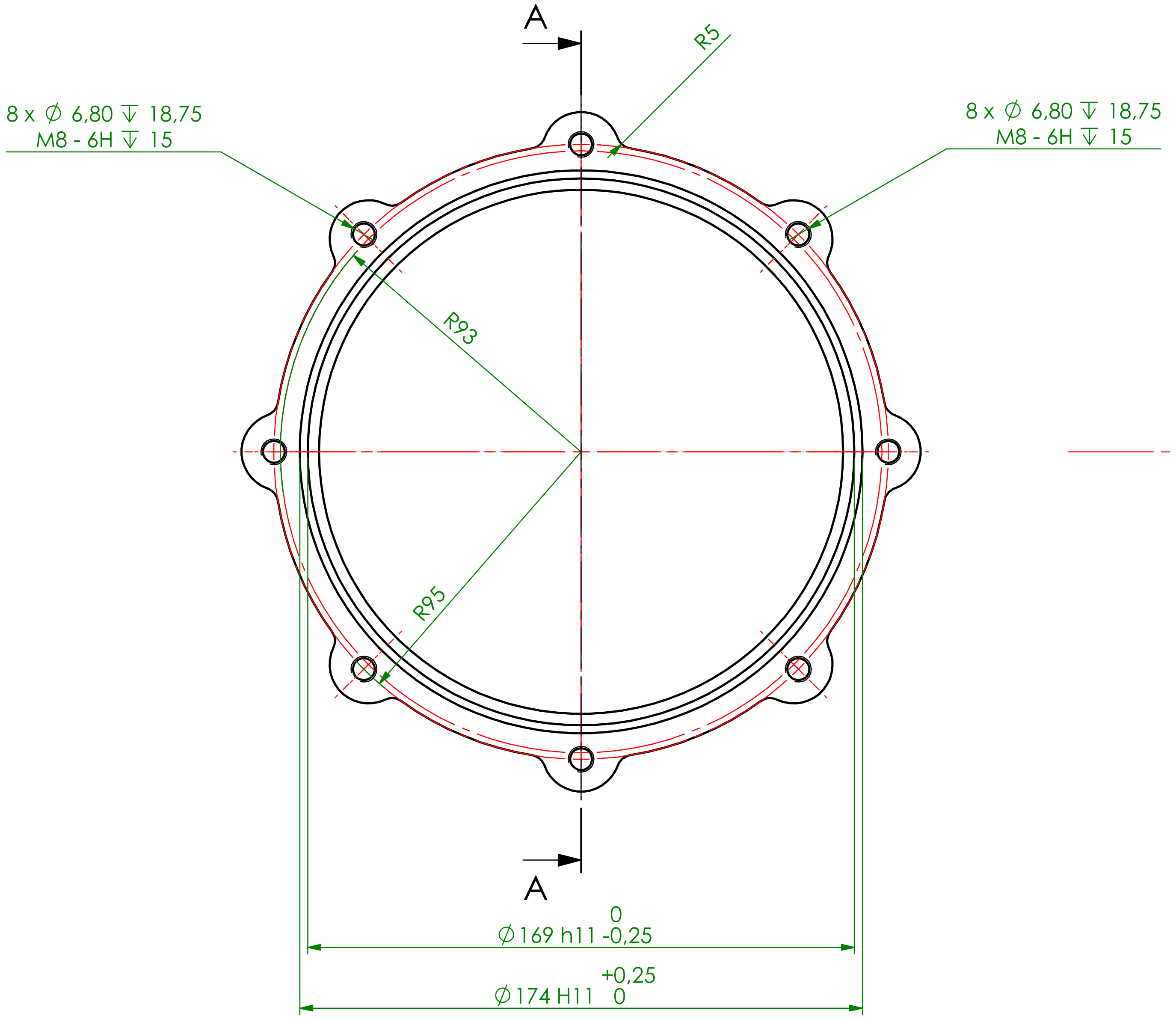

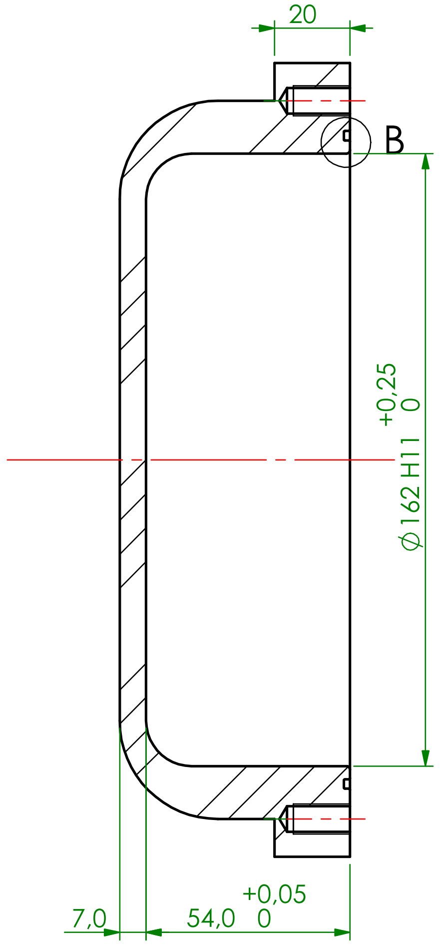

SECTION A-A

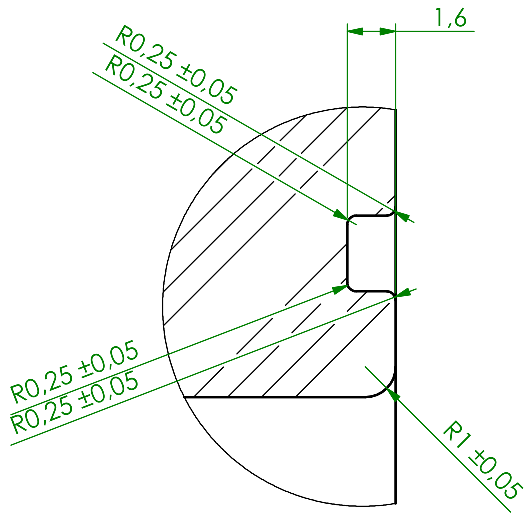

DETAIL B - Oring groove
SCALE 4 : 1

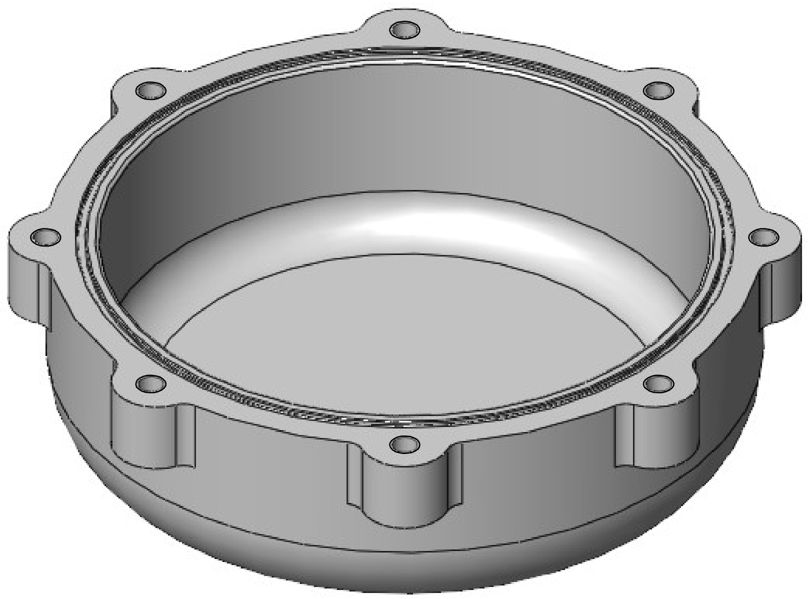

General Dimensions:

∅ 210 mm
Height 61 mm

UNLESS OTHERWISE SPECIFIED:
DIMENSIONS ARE IN MILLIMETERS
SURFACE FINISH: 3.2 µm
TOLERANCES:
LINEAR: ± 0.5 mm
ANGULAR: ± 1°

Created by: Pedro Pereira

Drawing and tolerancing standard:
ISO 2768-mK | ISO 8015

INESCTEC
CRAS - Center of Robotics and Autonoous Systems

CONFIDENTIALITY NOTICE

TITLE:
WCH

MATERIAL:
PET

DWG NAME
$PRPSHEET:{Name}

A3

WEIGHT: 797 g

SCALE:1:2

SHEET 1 OF 1

Refering to solid model for geometry not dimensioned is permissible.
All unspecified surfaces must match solid model within 0.5 mm.
Unless specified all corners are allowed a 1mm fillet

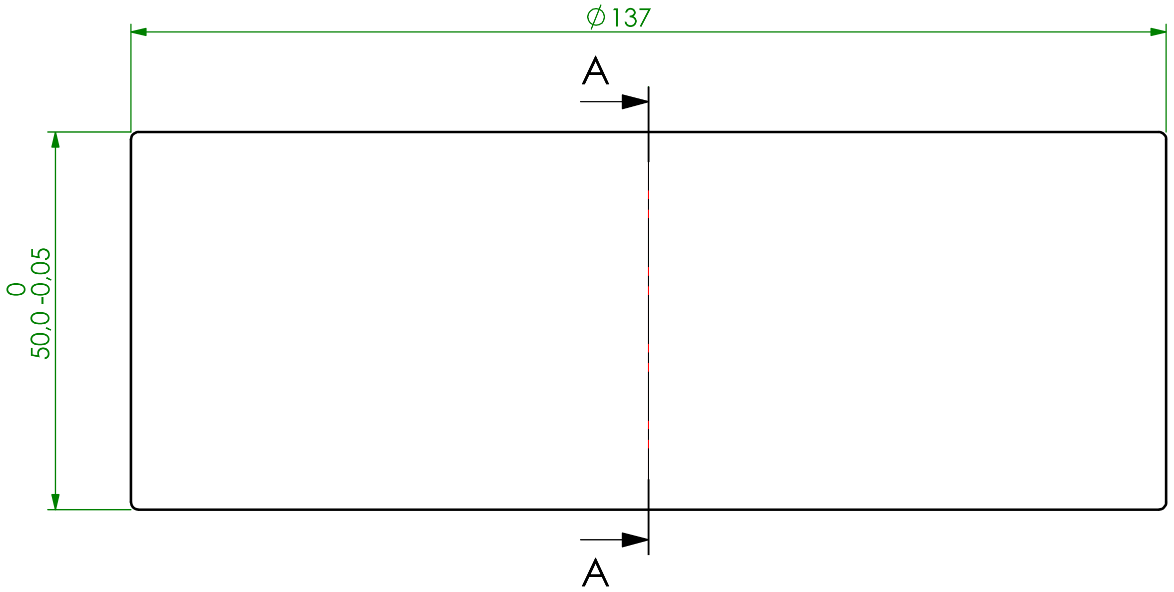

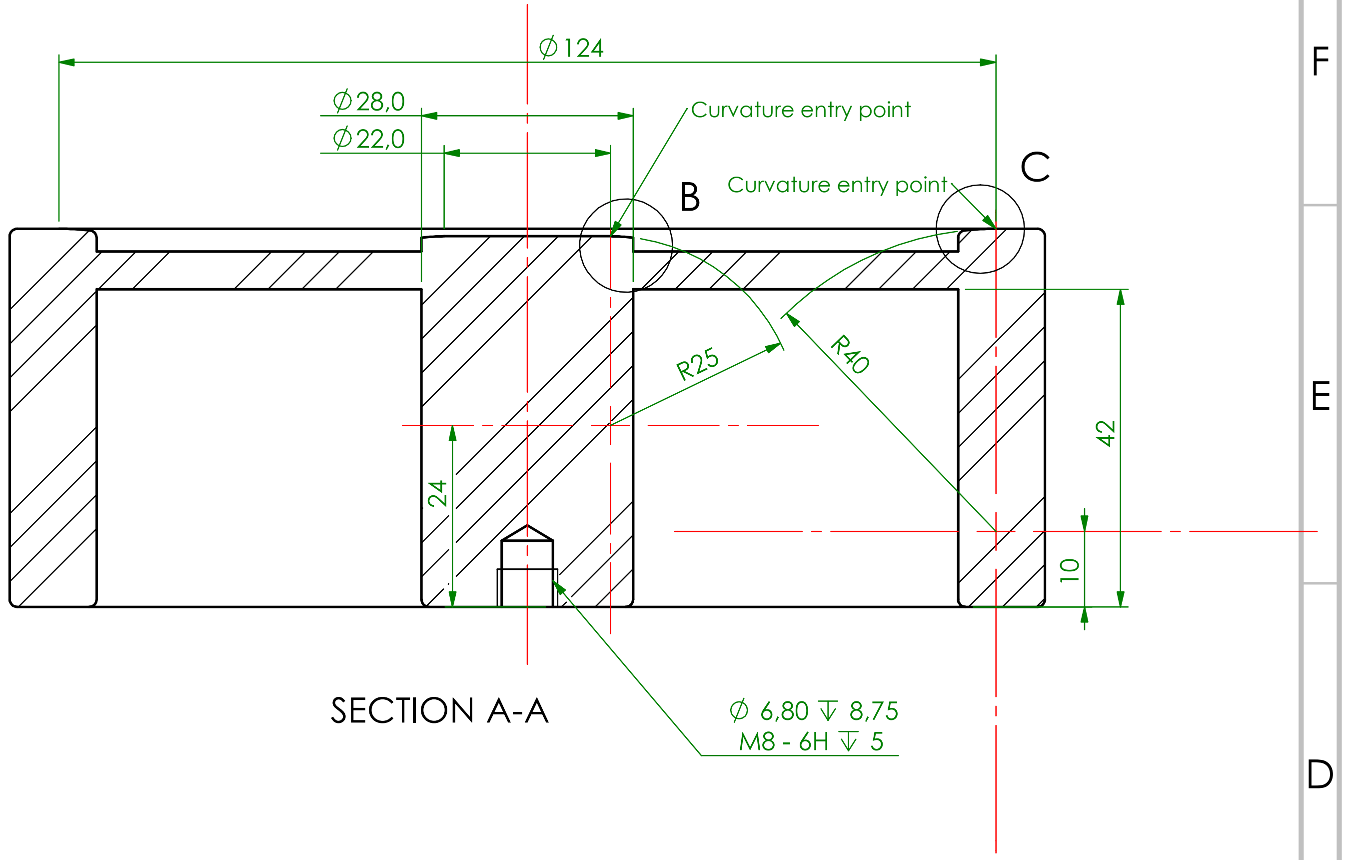

SECTION A-A

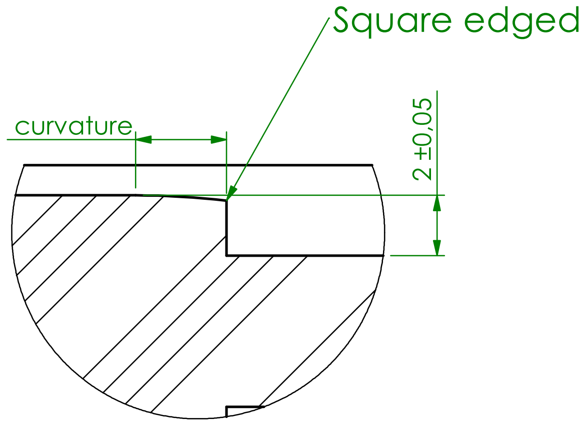

DETAIL B
SCALE 4 : 1

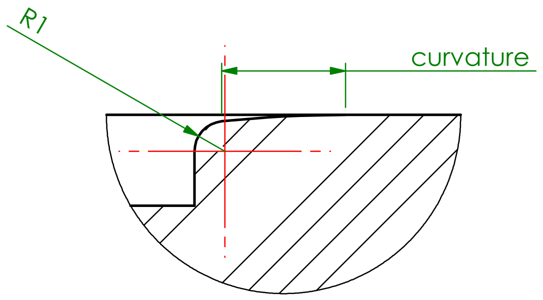

DETAIL C
SCALE 4 : 1

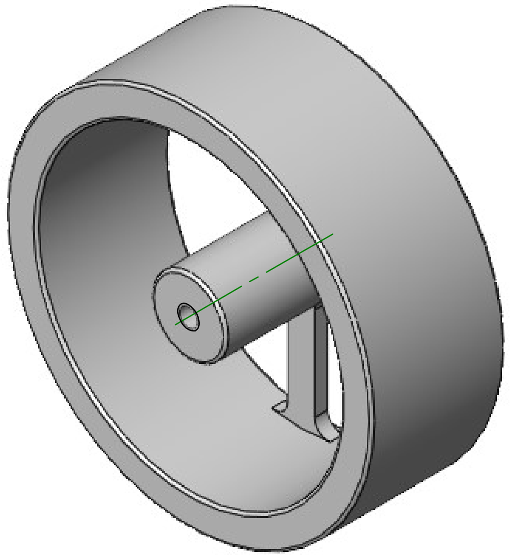

General Dimensions:

∅ = 137 mm
Height = 50 mm

UNLESS OTHERWISE SPECIFIED:
DIMENSIONS ARE IN MILLIMETERS
SURFACE FINISH: 3.2 μm
TOLERANCES:
LINEAR: ± 0.5 mm
ANGULAR: ± 1°

Created by: Pedro Pereira

Drawing and tolerancing standard:
ISO 2768-mK | ISO 8015

INESCTEC
CRAS - Center of Robotics and Autonoous Systems

CONFIDENTIALITY NOTICE

TITLE:
WCH

MATERIAL:
PET

DWG NAME
WCH Pillar 24

A3

WEIGHT: 362 g
SCALE:1:1
SHEET 1 OF 1

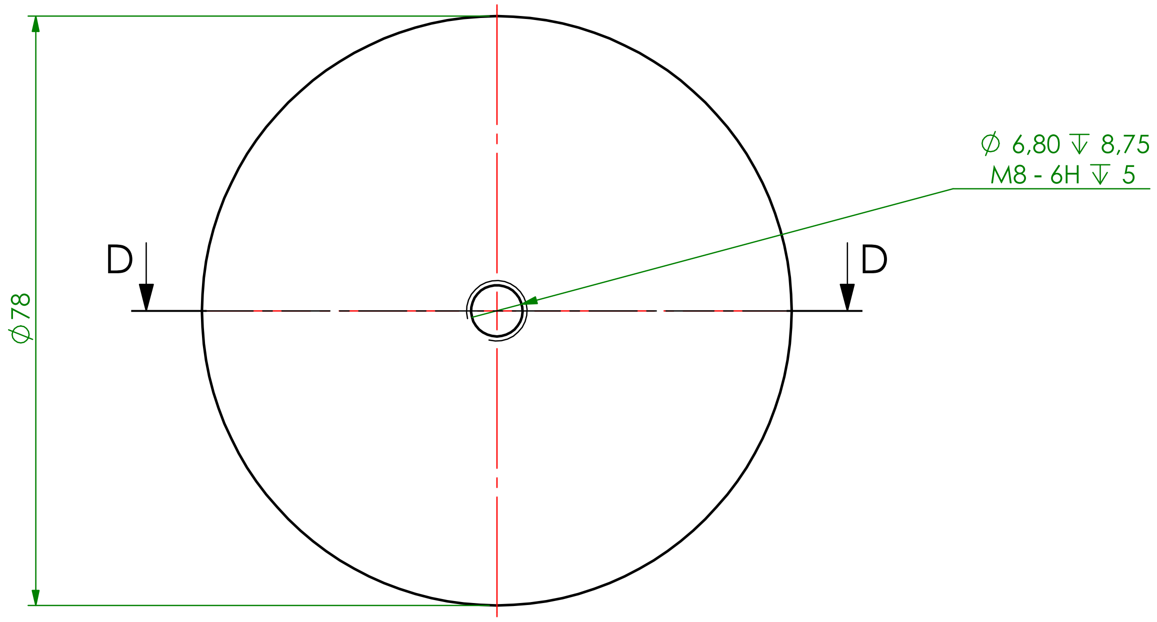

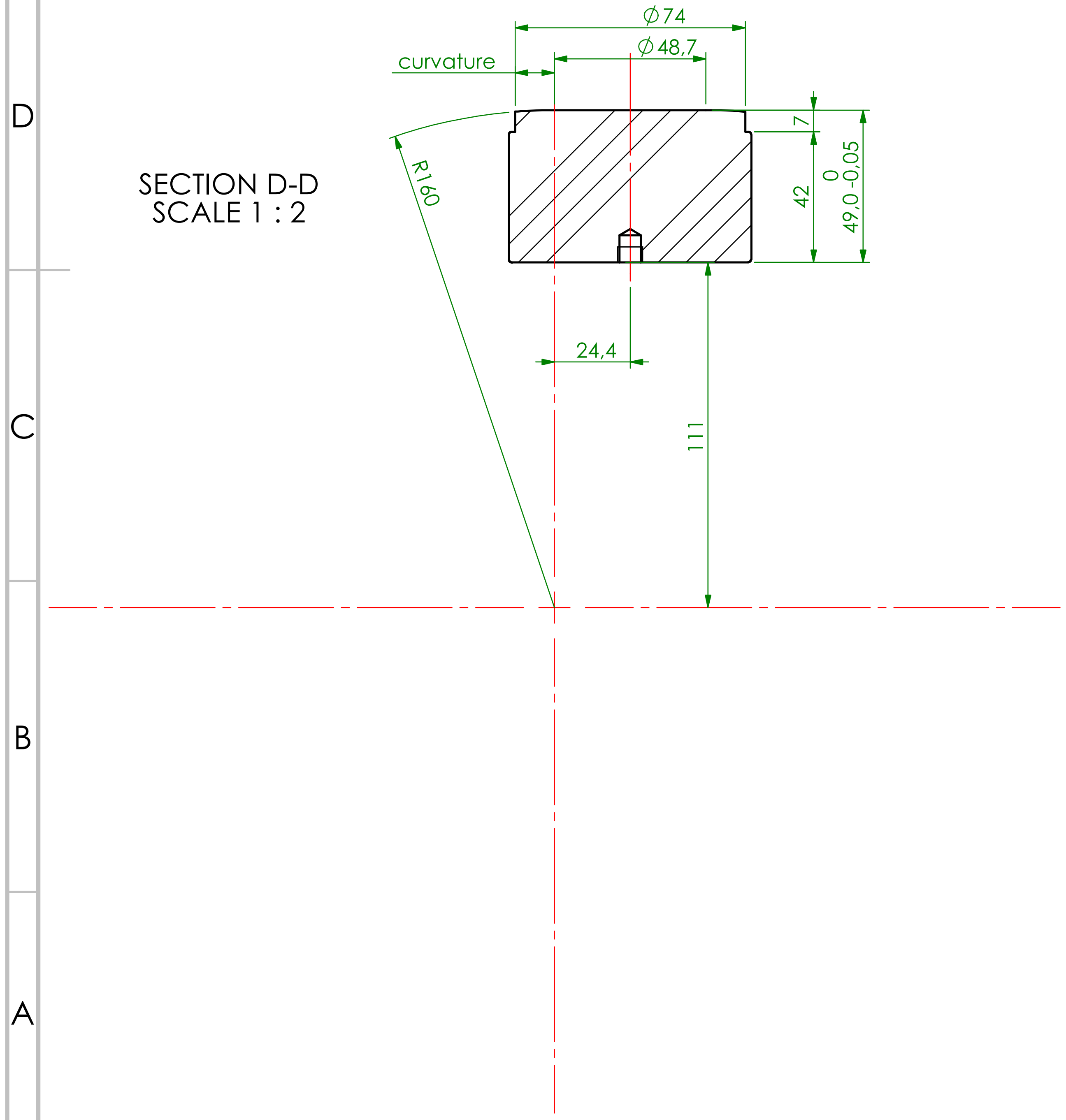

SECTION D-D
SCALE 1 : 2

General Dimensions:

∅ = 78 mm
Height = 49 mm

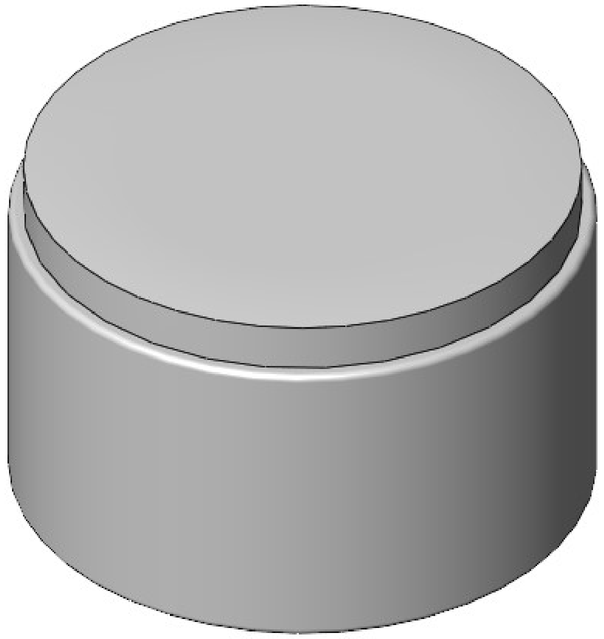

Refering to solid model for geometry not dimensioned is permissible.
All unspecified surfaces must match solid model within 0.5 mm.
Unless specified all corners are allowed a 1mm fillet

UNLESS OTHERWISE SPECIFIED: DIMENSIONS ARE IN MILLIMETERS SURFACE FINISH: 3.2 μm TOLERANCES: LINEAR: ± 0.5 mm ANGULAR: ± 1 °	Created by: Pedro Pereira Drawing and tolerancing standard: ISO 2768-1 | ISO 8015	INESCTEC CRAS - Center of Robotics and Autonomous Systems
CONFIDENTIALITY NOTICE THIS DRAWING AND INFORMATION CONTAINED HEREIN ARE THE EXCLUSIVE PROPERTY OF INESC TEC. AND SHALL BE RETURNED UPON DEMAND AND SHALL NOT BE REPRODUCED IN WHOLE OR IN PART TO ANYONE ELSE OR USED, WITHOUT THE WRITTEN CONSENT OF INESC TEC.		TITLE: WCH
MATERIAL: PET		DWG NAME: WCH Pillar 48 | A3
WEIGHT: 320 g		SCALE:1:1 | SHEET 1 OF 1